UNIVERSITY OF CALIFORNIA
RIVERSIDE

Synthesis of Inorganic Semiconductor Materials for Solar-Based Technologies

A Dissertation submitted in partial satisfaction
of the requirements for the degree of

Doctor of Philosophy

in

Chemical and Environmental Engineering

by

Wenting Hou

August 2014

Dissertation Committee:

Dr. David Kisailus, Chairperson
Dr. Robert Haddon
Dr. Pingyun Feng

This Dissertation of Wenting Hou is approved:

Committee Chairperson

University of California, Riverside

Acknowledgements

First, I would like to express my sincere gratitude to my advisor Professor David Kisailus for his continuous support and contribution to my study and research. His knowledge, patience, motivation, encouragement and enthusiasm have helped my all the time throughout my Ph.D. program, which probably the most challenging experience in my life. I also would like to acknowledge my committee members: Professor Robert Haddon and Professor Pingyun Feng for their valuable advice on my dissertation. I would also like to thank Professor Leigh Sheppard for his collaborative help with solar hydrogen performance. His generous help and expertise helped me to collect and analyze photoelectrochemical performance data.

I am very grateful to many past and current members in Professor Kisailus' group for providing a rich working experience, intellectual stimulation and friendship: Dr. Dongsheng Li, Dr. Qianqian Wang, Dr. Nichola Kinsinger, Dr. Jianxin Zhu, Chris Salinas, Parawee Pumwongpitak, Steven Herrera and Nick Yaraghi. Special thanks to the undergraduate students who have worked on this project, including Taysir Award, Ana Bowlus, Norman Lim, Nicholas Stewart, Is'haq Al Kindi, Louis Lancaster, Wei Tan, Chris Yang and Pablo Cortez.

I would like to thank Dr. Krassimir N. Bozhilov, Stephen McDaniel and Mathias Rommelfanger for their kind assistance in using the facilities in CFAMM at UCR. My thanks also go to my friends Dr. Yuanqi Tao, Dr. to be Haiyu Zhang, Dr. Xiadi Gao, Dr. Hongjia Li, and Dr. Qian Luo for their encouragement.

Most importantly, none of this would have been possible without the love and patience of my family. I would like to express my heart-felt gratitude to my parents Guoxiang Hou and Hong Wang, and my husband Yang Li for everything they have done for me.

Finally, I would like to take the opportunity to thank all persons who have ever helped me before.

Dedication

To my parents

Guoxiang Hou

Hong Wang

To my life partner and best friend

Yang Li

ABSTRACT OF THE DISSERTATION

Synthesis of Inorganic Semiconductor Materials for Solar-Based Technologies

by

Wenting Hou

Doctor of Philosophy, Graduate Program in Chemical and Environmental Engineering
University of California, Riverside, August 2014
Dr. David Kisailus, Chairperson

There is an alarming increase of energy issues due to significant fossil fuel consumption. Some progress has been made to replace fossil fuels with renewable sources, among which, solar energy has always been considered as the ultimate solution to solve these problems. As a relatively new evolved type of solar cell, Dye-sensitized solar cells (DSSC), have been investigated intensively in recent years and they are very promising for their cost-effectiveness properties. Zinc oxide (ZnO) is one of best candidates for DSSC due to its low cost and high electron mobility, amongst others. In this thesis, highly branched ZnO nanostructures are synthesized with biologically inspired methods to control the crystal growth and the mechanism by which these grow are investigated. Further explorations of the structure-function relationships reveal potential pathways towards the improvement of DSSC performance.

Besides DSSC, it is necessary to transform the solar energy to storable energy so it can be utilized during the night. Titanium dioxide (TiO_2) for hydrogen generation through photoelectrolysis is one of the most promising candidates. We synthesize TiO_2 nanowire arrays by homoepitaxial growth on templates, and precisely control the

nanostructured properties such as nanowire diameter, length, density, etc.. In addition, photoelectrochemical performance has been conducted on TiO_2 thin films with different nanostructures to investigate structure-function relationships.

Another significant concern involves environmental pollution due to the discharge or emission of a variety of new chemicals, which are threatening environmental and public health. ZnO, as a photocatalytic material, can effectively degrade organic pollutants without byproducts. In this work, we utilized biologically inspired methods to template the synthesis of Zn-organic compound materials using organic scaffolds. The complex material was heat-treated to produce a ZnO-carbon composite material. The processing conditions have been extensively studied and it has been demonstrated that the composite material can effectively improve the photocatalytic performance versus carbon-free ZnO nanostructured materials.

TABLE OF CONTENTS

LIST OF FIGURES

LIST OF TABLES

Chapter 1.

Introduction

1.1 Motivation and Background

Nowadays, over 80% of the energy consumption is provided by fossil fuels such as coal, petroleum and natural gas, and it is projected that world energy consumption will keep rising by approximately 35% from 2010 through 2040[1, 2], as seen in Figure 1. With the fast increase of fossil fuel consumption, two major issues have drawn more and more attention: concern of fossil fuel depletion and threats to the environment and public health.

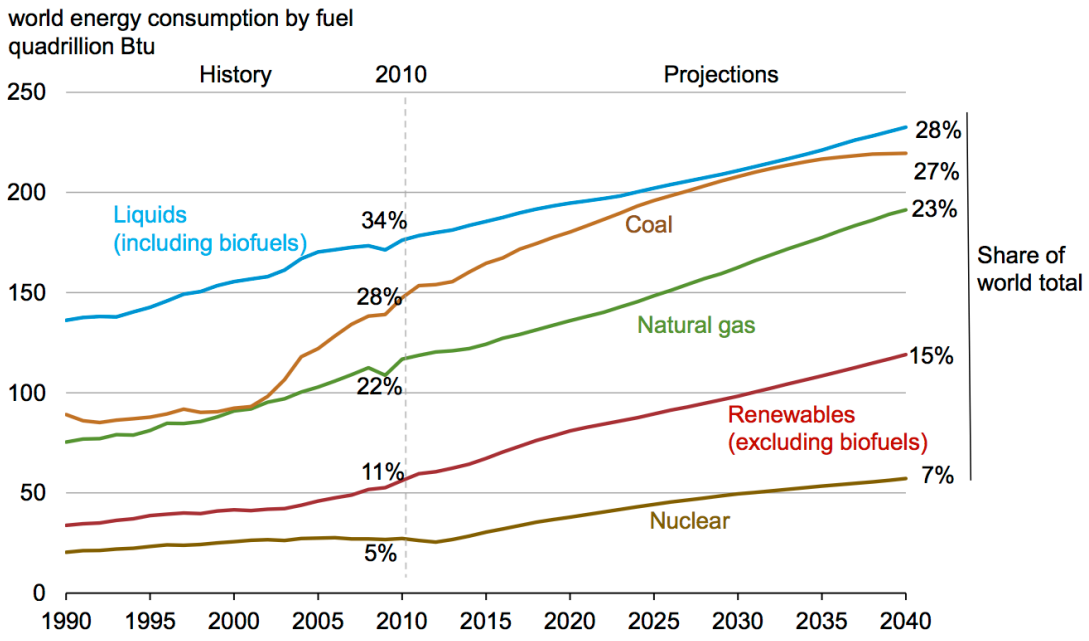

Figure 1. World energy consumption from 1990 to 2040. Source: EIA, International Energy Outlook 2013[2].

Significant progress has been made to replace fossil fuels with renewable energy sources such as wind, tides, sunlight, geothermal heat, and biomass[3-7]. It is expected that

the alternative technology would become more and more practical and price competitive with fossil fuels, eventually minimizing and even replacing the use of conventional fossil fuels[8]. From the International Energy Outlook of U.S. Energy Information Administration (EIA) in 2013, as seen in Figure 1, although the conventional energy (such as coal and natural gas) still remains as the dominant energy source, renewable energy is the fastest growing source of energy consumption [2].

Among all the renewable energy technologies, solar energy, as a carbon-neutral process, is considered the ultimate solution to replace fossil fuel and meet the environmental challenges [9]. Solar energy is one of the fastest growing renewable electricity technologies worldwide. Solar generation grew by a factor of 49 between 2000 and 2012. The United States, in 2012, installed solar photovoltaic capacity grew more than 83% from the previous year (Figure 2), which produced 3% of the total renewable electricity generation [10].

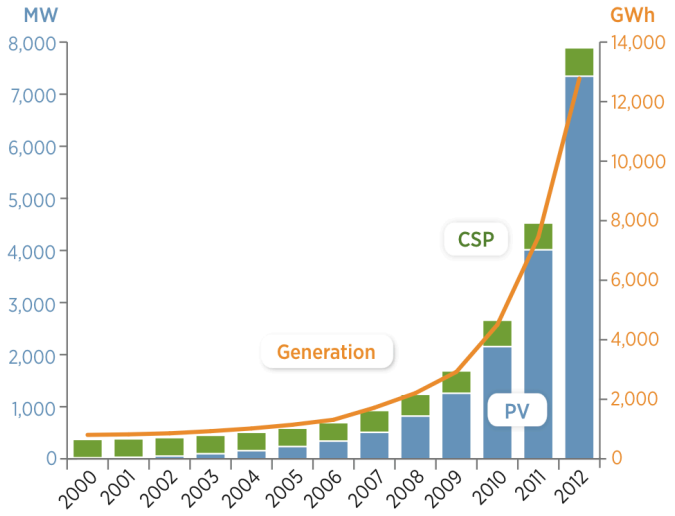

	U.S. Solar Energy Generation (GWh)	U.S. Solar Energy Capacity (MW) and % Increase from Previous Year			
		PV*	CSP	Total	Increase
2000	804	18	354	372	4.3%
2001	822	29	354	383	3.0%
2002	857	52	354	406	5.9%
2003	929	97	354	451	11.2%
2004	1,020	155	354	509	12.8%
2005	1,145	234	354	588	15.5%
2006	1,312	339	355	694	18.0%
2007	1,718	508	419	927	33.5%
2008	2,208	819	419	1,237	33.5%
2009	2,922	1,257	430	1,686	36.3%
2010	4,505	2,153	507	2,660	57.7%
2011	7,454	4,011	516	4,527	70.2%
2012	12,775	7,344	546	7,890	74.3%

Figure 2. Total installed solar electricity capacity and generation[10].

Although solar cells are considered being one of the most promising alternative candidates for replacing fossil fuel, there are some disadvantages such as low efficiency and high cost. In addition, as the sun is not shining 24 hours a day (i.e., a cloudy day or during the night), cost-effective and efficient solar cells need to be achieved. We need to store the energy when the sun is not shining. Recently, the conversion of solar energy to storable fuels have become an attractive topic. Hydrogen, due to its high energy content per unit mass (120 J/g vs. gasoline ~ 40 J/g), is one of the most attractive clean fuels [11, 12]. The conventional technology for producing Hydrogen is through steam and hydrocarbon reactions, which are not only expensive, energy consuming, but are also based on fossil fuels. In recent years, water splitting via sunlight has become one of the most attractive approaches for hydrogen generation. The process uses sunlight as the energy source and

water as hydrogen source, to produce hydrogen in a low cost, environmental friendly way via either photocatalysis or photoelectrochemistry[11, 13, 14].

Besides fossil fuel depletion, environmental crises is always a big concern, especially air and water pollution caused by industrial activities and our daily life. There are limited clean water sources in the world, and there has been a push to clean up wastewater to make drinkable water for daily life. However, due to the development of industrial technologies, there has been a dramatic increase in the variety of new chemicals being produced and now detected in our water systems. These include dyes (widely used in food, drug, paints and cosmetics) and different kinds of pharmaceuticals and personal care products. The emergence of these new compounds is believed to cause concerns to public health and safety, even to the whole ecological system [15]. Therefore, new water treatment technologies have to be implemented to remove the hazardous compounds for purified drinkable water. Recently, degradation of harmful compound in wastewater via sun light has become more popular and promising [16, 17].

1.2 Dye Sensitized Solar Cells

1.2.1 Evolution of Solar Cells

"I'd put my money on the sun and solar energy. What a source of power! I hope we don't have to wait until oil and coal run out before we tackle that."

--- Tomas Edison

Solar energy is primarily referring to the radiation energy of sunlight. Every organism needs the heat and light provided from sun since the formation of the earth. The

solar energy irradiating to the surface of the Earth is about 1.3×10^5 TW, about 4 orders of magnitude of the total global energy consumption (reported at 1.3×10^1 TW in 2010). Human beings started to utilize sunlight from ancient times to dry food for preservation or providing heat [18]. The usage of sunlight as an energy source has been developed since 1916, when a French engineer, Salomon De Caux, invented the world's first solar powered motor [19]. The use as "alternative energy for fossil fuels" for electricity generation is a recent developed technique.

There are normally two ways to utilize sunlight to produce electricity: solar thermal electricity and solar photovoltaics. Modern solar thermal technologies collect solar energy and convert to electricity through the use of some sort of heat to an electricity conversion device, such as a heat engine. It was first brought up by Mouchot and Pifre about 140 years ago, where it was believed to be a technology with great potential in the renewable energy area [20, 21]. With rapid developments in this technology, more commercial concentration solar thermal power plants have been installed in the world. The world's largest solar power plant, Ivanpah Solar Power Facility, has been built and put into use in 2014. The Ivanpah solar electric generating system is located in the Mojave Desert of California and consists of three solar thermal power plants, with a power production of 377 MW, which can be used to serve the electricity for more than 140,000 homes in California.

Photovoltaic technologies, which are different from solar thermal technologies, convert solar energy directly into electricity to power external loads. It was first reported by Edmund Bequerel in 1839, when he observed " The photovoltaic effects" that the light

on a silver coated platimum electrode immersed in electrolyte produced an electric current [22]. In 1885, Charles Fritts constructed the first solar cell by using a thin layer of selenium between gold and another metal [23]. The first silicon-based solar cell was reported by Chapin, Fuller and Pearson in 1954, and the efficiency of the solar cell was 6% [18]. Silicon-based solar cells have been widely developed since then, and the efficiency has risen significantly. However, the cost of the silicon solar cell during that time was approximately $200 per watt, comparing to $2 per watt from coal plant, it was too high to be used for power generation. Therefore, research efforts were focused on lower cost materials for solar cells. Different kinds of solar cell evolved, especially after the "Energy Crisis" in 1970s. During 1990s, the number of papers on Photovoltaics further expanded at a rate of 15-25% annually [23]. The research focused on the improvement of device efficiency and lowering cost. New materials such as polycrystalline silicon, amorphous silicon, "thin film" materials and organic materials have been developed for use in solar cells. In addition to prices decreasing, the efficiency of different kinds of solar cell were improved. Figure 3 shows the conversion efficiencies of a variety of solar cells. The graph indicates that monocrystalline solar cells are the most efficient, followed by single crystalline silicon panels and thin-film solar cells.

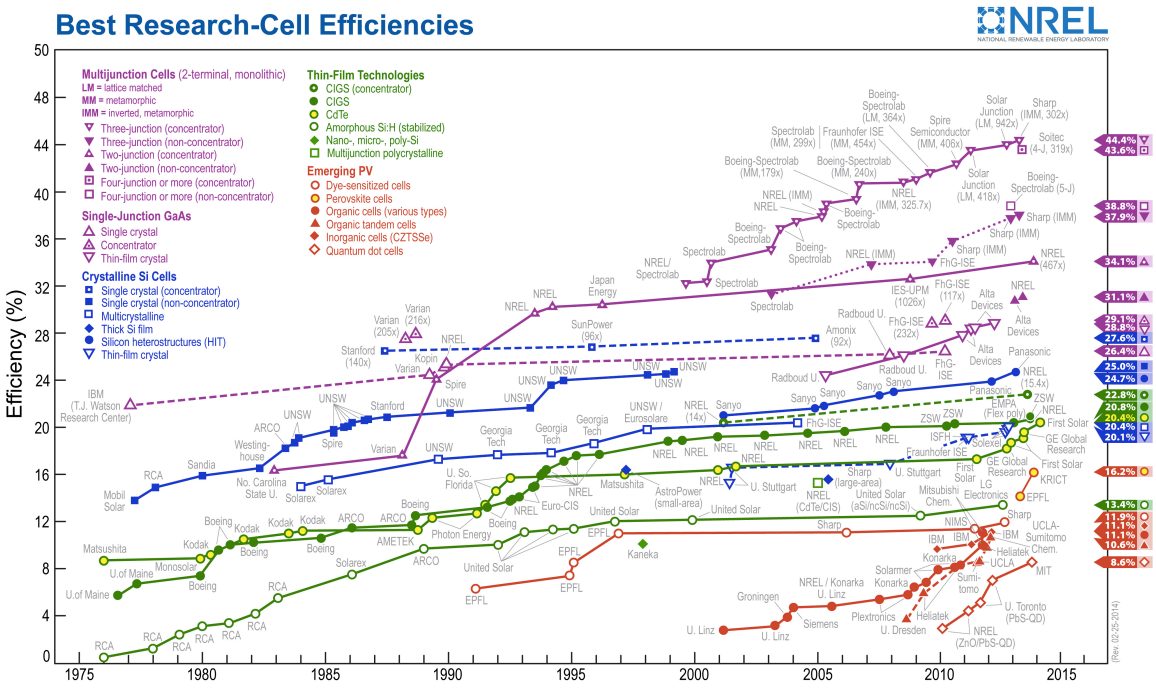

Figure 3. Conversion efficiencies of best research solar cells worldwide from 1976 through 2014 for various photovoltaic technologies (from National Renewable Energy Laboratory (USA)).

However, efficiency is not the only reason for choosing the solar cells; cost-effectiveness is critical. Currently, highly efficient solar cells have high costs. For example, the efficiency of conventional single crystalline silicon solar cells are about 20% [24]. However, because of the considerably high material processing costs, a cost-effective solar cell needs to be produced. Thin-film solar cells have been developed to address these production costs. Among all the thin-film solar cells, dye-sensitized solar cells (DSSCs or Gratzel cell), as a fairly recently developed solar cell, has attracted significant attention and has made significant progress in recent years. It has challenged the

conventional solid-state photovoltaic technologies, and developed solar cell at a molecular and Nano level [25].

1.2.2 Operational Principles and Development of Dye-sensitized Solar Cells

DSSCs was invented by Michael Gratzel and Brian O'Regan in 1988, and they published on the first high efficiency DSSC in 1991 [26]. It is currently one of the most promising solar technologies available for inexpensive, large-scale solar energy conversion [27]. This kind of solar cell is easy and inexpensive to manufacture, and it is proved to be stable for long time use without efficiency decrease [25]. Compared to other solar cells, DSSCs have better performance at higher working temperatures and under diffuse light conditions (i.e., it can be used indoors or under cloudy skies). The cells are also flexible, which makes it possible to be manufactured into any shape. It also has a tunable color, transparency and is lightweight, which provides a great potential to be used in commercial and daily life. The Sony Company has incorporated this technology into residential use by introducing DSSCs into power-generating windows, Hana-Akari room lights and solar mobile device chargers. These conceptual models demonstrate both output advances and intriguing design possibilities, and hint the potential of generating our own power to satisfy electricity needs.

The dye-sensitized solar cell contains broadly five components: (1) a mechanical support coated with transparent conductive oxide, (2) a ~10 μm thick film of wide band gap semiconductor nanoparticles such as titanium dioxide (TiO_2) or zinc oxide (ZnO) nanoparticles, (3) a monolayer of sensitizers/dyes absorbed onto the surface of the

semiconductor, (4) a liquid electrolyte containing the redox couple triiodide ions/ iodide ions (I^-/I^{3-}), which interpenetrates the dye-coated nanoparticles, and (5) a counter electrode containing catalysts like platinum or graphite, which are capable of regenerating the redox mediator. Figure 4 shows the composition and operational principles of DSSCs. When sunlight is shined through the transparent electrode into the dye layer, absorption of light by the dye molecules results in the formation of excitons (or electron-hole pairs). These excitons will dissociate at the dye molecule - TiO2 interface. Subsequently, an electron is injected into the semiconductor oxide conduction band and the hole is transferred to the electrolyte. The electrons would disperse in the semiconductor layer and be conducted outside toward the anode where they would be collected for powering a load. After flowing through the external circuit, they are re-introduced into the cell, and then flow into the electrolyte, where the electrons would be used to reduce the triiodide ions (I^{3-}) to iodide ions (I^-), and then the iodide ions supply electrons to the dye molecules [27, 28].

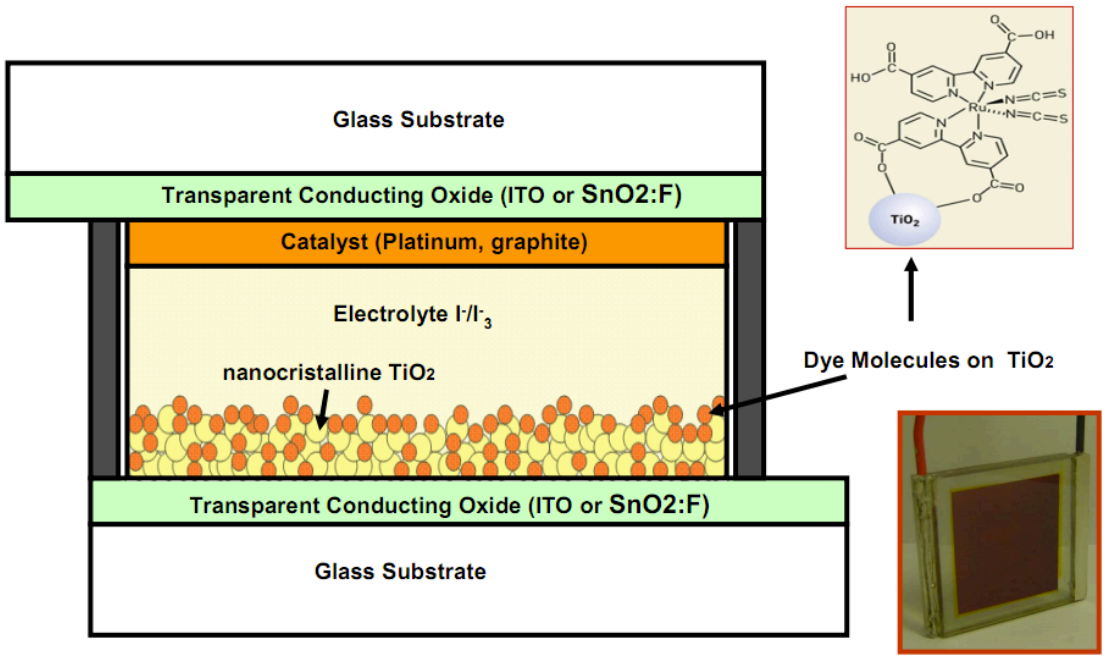

Figure 4. Structure and composition of dye-sensitized solar cell [29].

DSSCs utilize the photo-excitation of dye molecules, such as TiO_2–$RuL(NCS)_3$ (‘‘black dye’’), adsorbed on the semiconductor materials [30-32] to provide electrons. Central to this device is a thick semiconductor nanoparticulate film (typically made of TiO_2 that provides a large surface area for the adsorption of light-harvesting dye molecules. With the development of DSSCs, the highest conversion efficiency achieved is approximately 15% [33, 34]. Although the increase of the efficiency is dramatic, it is still lower compared to broadly used silicon-based solar cells, which have the highest conversion efficiency of 25%. The conversion efficiency of DSSCs has been limited mainly due to electron recombination in the bulk and at the interfaces of the electrodes as well as a limited coverage of electron producing dye molecules. In conventional DSSCs, high dye molecule coverage have been realized by high surface area TiO_2 nanoparticles.

A further increase in conversion efficiency has been limited by energy loss due to recombination between electrons and either the oxidized dye molecules or electron-accepting species in the electrolyte during the charge-transport process [35-37]. ZnO possesses an energy-band structure and physical properties similar to those of TiO_2, but has higher electronic mobility (200-1000 cm^2vs^{-1} compared to TiO^2=0.1~4 cm^2vs^{-1}) that would be favorable for electron transport with reduced recombination loss when used in DSSCs [27]. Studies have reported on the use of ZnO material for application in DSSCs. Although the conversion efficiencies of 0.4–5.8% obtained for ZnO-based DSSCs [27] are much lower than that of 13% for TiO_2 [28], ZnO is still thought of as a distinguished alternative to TiO_2 due to its ease of crystallization and anisotropic growth. These properties allow ZnO to be produced in a wide variety of nanostructures, thus presenting unique properties [38, 39]. Leschkies et al. have reported 0.4% power conversion efficiency (PCE) value of QDSSC based on single layer ZnO nanowire [40]. Guo et al. have reported 2.1% of PCE based on ZnO nanorod for DSSC [41]. Jiang et al. have reported 90% improvement of PCE value based on ZnO nanoflowers compared with nanorod photoelectrodes in DSSC based on increased absorption of sensitizers [42].

1.3 Solar Hydrogen Generation

1.3.1 Hydrogen Generation methods

When alternative energies, such as solar energy, are being used, the toughest problem is the variability in conditions. We cannot control when the sun is shining and

therefore, a solution to save solar energy becomes very important. Energy can be stored by a variety of methods, such as electromagnetic waves, and chemical bonds. Among these, the chemical bonds of molecules turn out to be the most energy dense way to store energy. Hydrogen provides a clean, efficient, safe, storable, and transportable of energy storage, and has generally been considered the best candidate as a pollution-free green energy. Thus, it has attracted the attention from multiple researchers [43]. Hydrogen is the most abundant element on earth, but it does not exist in the atmosphere in its molecular form. It must be produced from other primary energy sources such as fossil fuels, biomass, or water. Figure 5 shows examples of hydrogen production pathways.

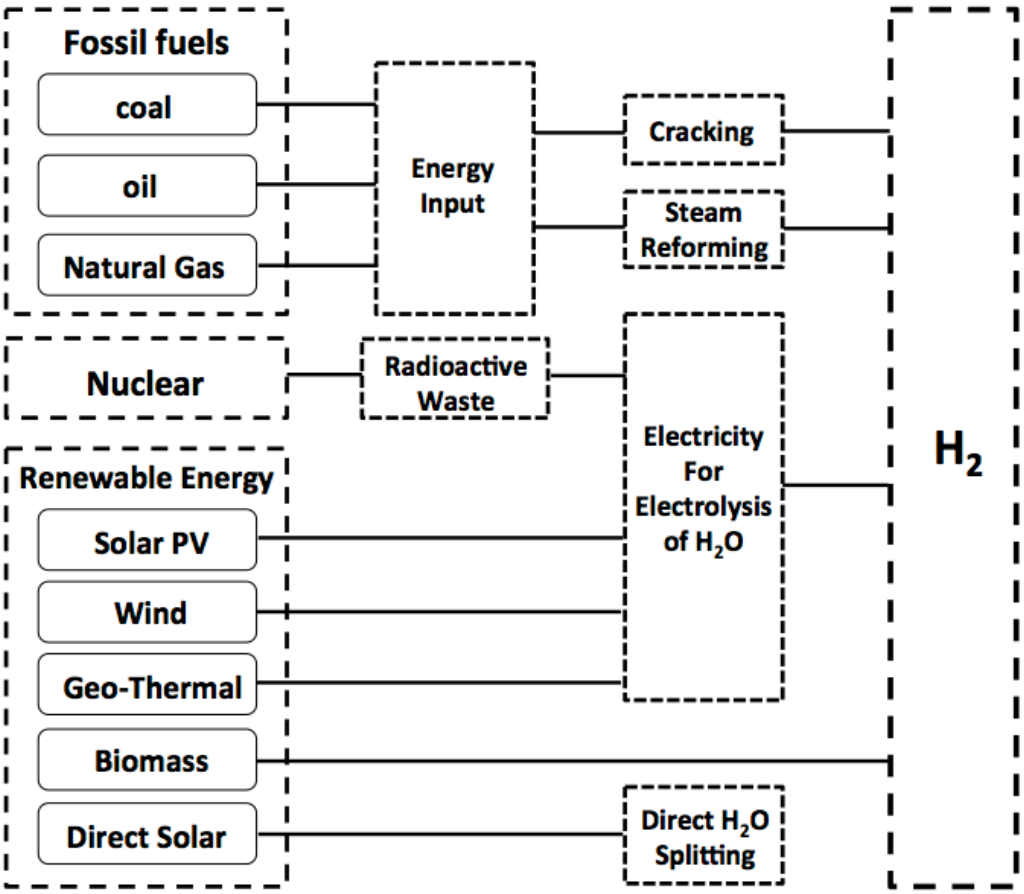

Figure 5. Examples of Hydrogen Production Pathways.

Currently, hydrogen is mainly produced (~95%) through steam reforming, which uses fossil fuels as the dominant source, and carbon dioxide is generated along with hydrogen.

$$CH_4 + H_2O \rightarrow CO + 3H_2 \quad (1.1)$$

$$CO + H_2O \rightarrow CO_2 + H_2 \quad (1.2)$$

This steam reforming process not only relies on the utilization of fossil fuels, but also accelerates the green house effect by producing carbon dioxide. Furthermore, these

reactions are conducted with intensive energy at high temperatures from 700°C to 1000°C [44]. Other conventional techniques including electrolysis and thermolysis can also be used for hydrogen generation, but the hydrogen generation process is conducted under very high temperatures (800°C to 2500°C), and thus lot of energy is needed [45]. Therefore, the cost of hydrogen production becomes an important issue, and a convenient and inexpensive method for producing hydrogen energy becomes the dream of scientists.

In nature, plants can convert sunlight energy with some precursors to sugar for energy storage via photosynthesis. Similar to photosynthesis, scientists find out that we can also collect and store solar energy in chemical bonds (e.g., H_2). In 1972, Honda and Fujishima first proposed the photocatalytic splitting of water through a single crystal TiO_2 electrode, which was a milestone, indicating the possibility to obtain H_2 fuel from solar energy via cheap semiconductors [46]. Water is a very stable compound under standard conditions. As seen in equation (1.3), it is an energetically unfavorable reaction, and the free energy change for the conversion of H_2O to H_2 and $1/2O_2$ is ΔG=237.2 kJ/mol, and ΔE^0=1.23 V per electron transferred according to Nernst equation.

$$H_2O \rightarrow H_2 + 1/2O_2 \qquad (1.3)$$

A water splitting cell, is composed of stable semiconductors, which under sunlight, are designed to split water at the semiconductor surface by photoelectrolysis, driving both the hydrogen evolution and water oxidation reactions.

1.3.2 Photocatalytic Water Splitting

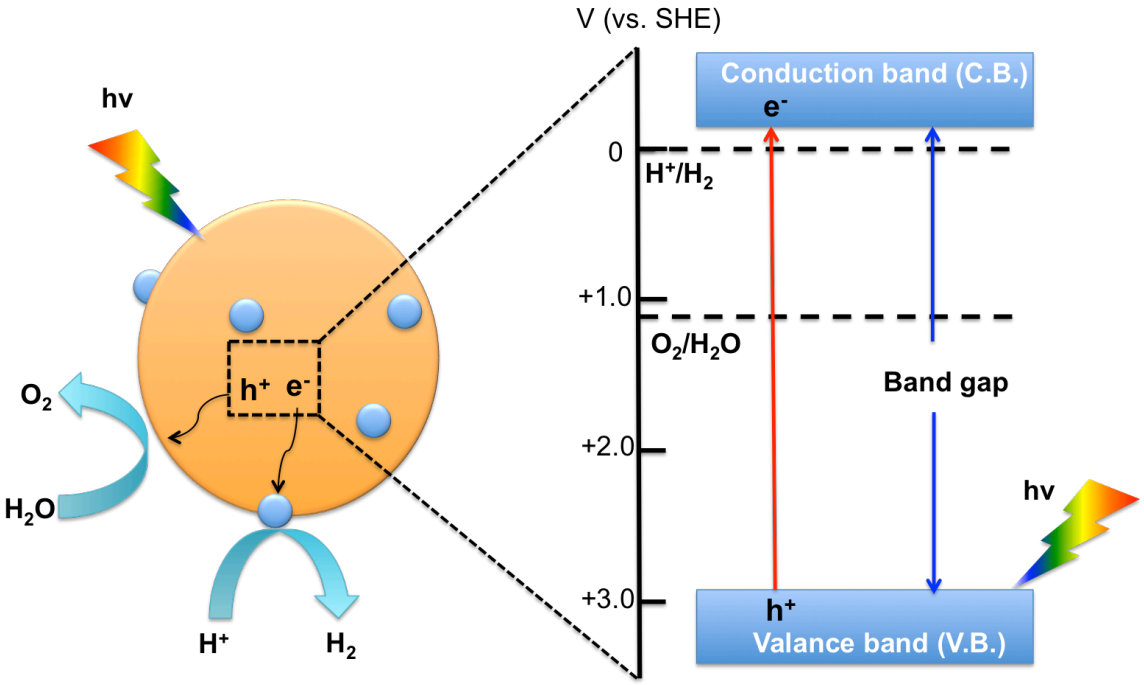

Figure 6. Mechanism of photocatalytic decomposition of water into H_2 and O_2.

The primary process can be divided into the following three steps:

(1) When the sunlight is shining on the semiconductor photocatalyst, a photon is absorbed and generates electron-hole pairs, and the photocatalytic reactions will be conducted on the surface of the semiconductor materials, as seen in Figure 6. When the energy of the incident photon is equal to or exceeds the band gap energy level (E_g), the electron can be excited from the valence band (VB) to the conduction band (CB), a positively charged hole left behind in the valence band [47]. As seen in Figure 6, the photo-excited carriers (electrons and holes) will be transferred to surface active sites. Electrons are conducted from the conduction band to the interface of the semiconducting material

with water, and H^+ in water will gain these electrons to be reduced to H_2. The holes will transition to water and be oxidized. Water is split at the semiconductor surface by photoelectrolysis, driving both the hydrogen evolution and water oxidation reactions.

(2) The electron-hole separation and migration are the most important steps in the photocatalytic process, since unsuccessful and ineffective separation and migration would hinder the performance efficiency. The electron-hole separation and migration can be affected by a wide variety of factors, such as the crystal size, crystallinity, morphology and the orientation of the semiconductor materials. For example, crystal size is a key factor in the carrier transport process. Smaller particle size would benefit the carrier transport due to shorter diffusion distance, however, electron-hole recombination are mostly happened through surface trap sites rather than in the bulk, which is related to high surface area. Therefore an optimized size particle sized need to be obtained for achieving minimum electron-hole recombination [48]. Another factor is the crystallinity of the semiconductor materials. The diffusion rate of carrier depends on the crystallinity of the nanoparticles. High crystalline structure would benefit the electron hole migrations. The defects and grain boundaries in less crystalline structures would serve as the centers for electron-hole recombination, which may induce heat or radiation instead of water splitting [49]. Furthermore, the orientation and the morphology of the crystal also affect the carrier transport rate. It is reported the electrical conductivity is highest along the [001] direction [50], which indicate a preferred orientation or specific crystal structures to eliminate the electron-hole recombination and provide high performance.

(3) The surface chemistry would highly affect the photocatalytic water splitting performance. The photo-generated carriers would conduct reduction and oxidation reactions on the surface of the semiconductor materials. The surface chemical reactions are related to the surface area, on one side, high surface area would let the carriers have more chance to contact with water, which is the source of hydrogen revolution; on the other side, high surface area may lead to high concentration of surface defects or trap sites for electron-hole recombination. Only electrons and holes that migrate to the surface without recombination can be consumed for Hydrogen and Oxygen evolutions.

The key of the photocatalytic water splitting cell is the semiconductor materials. There are a few requirements for the semiconductor material to be used in the water splitting cell: (1) long-term stability and resistivity to corrosion; (2) Low cost and availability; (3) rapid charge transfer at the semiconductor/aqueous interface; (4) having a conduction band-edge energy (E_{cb}) and valence band-edge energy (E_{vb}) that straddles the electrochemical potentials $E^0(H^+/H_2)$ and $E^0(H_2O/O_2)$; (5) Effective absorption of photons of the solar spectrum related to the band gap in the photon energy range of 1.6–1.9eV. (See Figure 7). Among all the candidates, TiO_2 is shows great stability and relatively high reactivity in the photocatalytic reactions. It is widely studied and has been reported to be one of the most promising candidates for solar hydrogen production. TiO_2 nanoparticles can absorb photons with energies equal or higher than the band gap energy of TiO_2 (3~3.2 eV). After the photons are absorbed, electrons are excited from the valence band into the conduction band, creating electron-hole pairs, which facilitate redox reactions on TiO_2 surfaces through the formation of adsorbed radicals [51, 52].

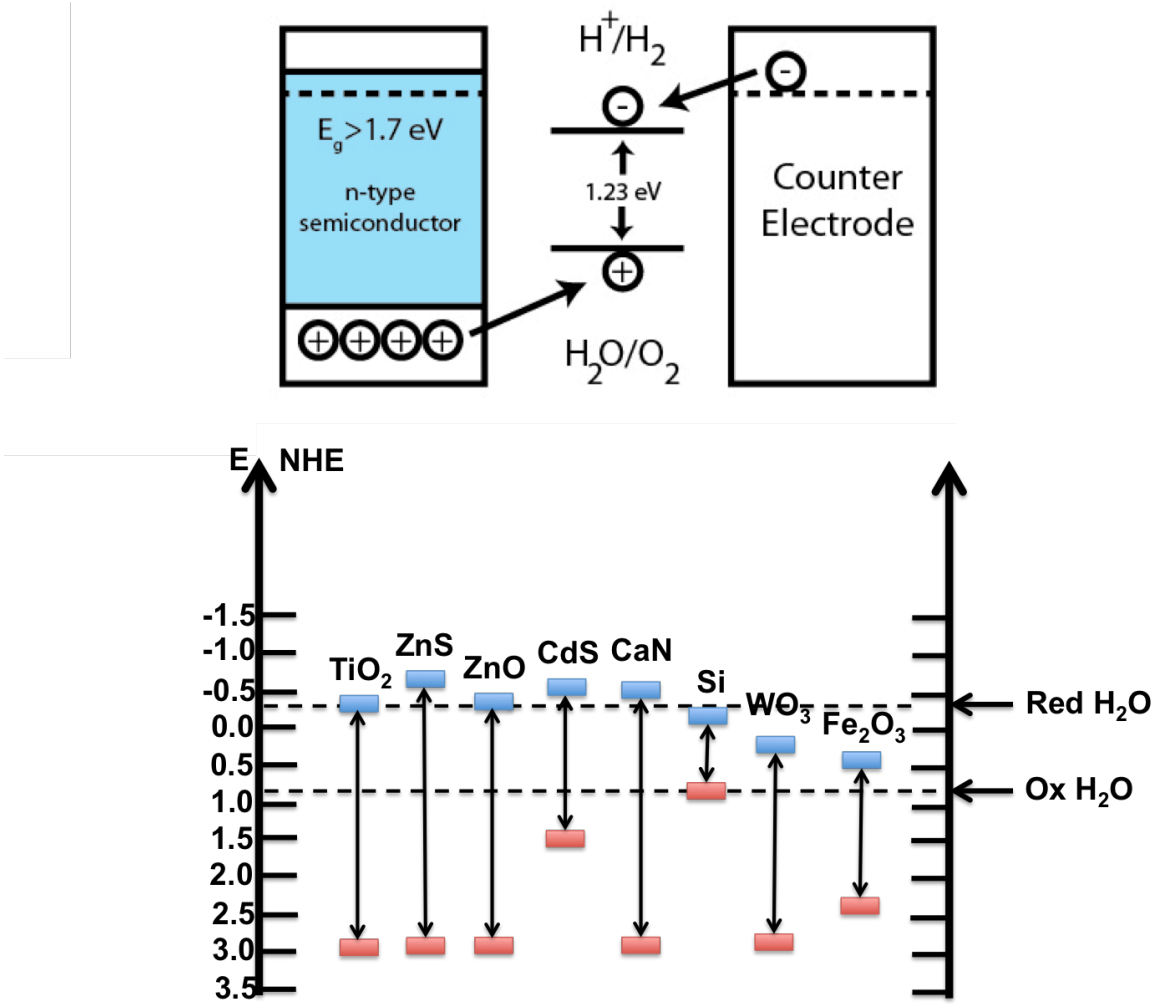

Figure 7. Valence and conductance band positions for various seminconductors.

So far, with the development of photocatalytic water splitting cells, there are still some problems for the photocatalysis system, and the conversion efficiency of solar energy to hydrogen is still not satisfactory. The reason of the low efficiency is mainly due to inability to utilize the whole spectrum of sunlight and fast electron-hole recombination. Most photocatalysts are only stable and effective under the ultraviolet light. However, the

ultraviolet light only takes about 5% of the whole solar energy, and the visible light region takes almost all the sunlight spectrum. The photocatalysts that could work under visible light always have very low photocatalytic activity, or show light corrosion phenomenon. Even when the electrons and holes were generated successfully, they may conduct a recombination reaction immediately, or during the migration process, the electrons or holes might be consumed by the trap sites in the bulk or on the surface of the semiconductor particles. These disadvantages would lead to low energy conversion efficiency, and hinder the practical application of the photolysis of water.

To improve the conversion efficiency, a lot of researches have been done to solve the electron-hole recombination and broaden the working spectrum for the materials. The electron-hole recombination can be minimized through several approaches. Besides increasing the crystallinity of the materials and optimized the particle size and surface area, a lot of additives can be used to enhance the hydrogen production. Noble metals, such as Pt [53], Au [54], Cu [55], and Ag [56], are usually used and reported to be very effective to enhance the surface chemical reactions to produce hydrogen. Addition of electron donors to the surface can also enhance the hydrogen production. For example, methanol [57] and inorganic ions such as S^{2-}/SO_3^{2-} [58], IO_3^-/I^- [59] can be used as electron donors to react with the photo-generated VB holes, therefore reduce the electron-hole recombination in the bulk. Carbonate salts such as HCO_3^-, $CO3^-$ can also be added to suppress backward reactions by consuming the photo-generated holes, and enhance the hydrogen production [60].

To broaden the absorption spectrum of the materials, take TiO_2 as an example, a wide variety of methods have been reported. The band gap of TiO_2 can be modified to affect the absorption spectra by shifting the absorption edges to longer wavelength light. And the change of band gap can be achieved by cation doping, such as transitional metal ions and rare earth metal ion doping. It has been proved TiO_2 with metal ions (for example, Ta [61], Cu [62] and Fe [63]) doping would expand its absorption into visible spectrum, since the metal ions dopant would introduce impurity energy levels [64]. However, the cation doping is likely to form recombination center for a reverse reaction. Unlike cation doping, anion doping is more effective in the photocatalytic activity. Anion doping would shift the band gap into visible spectrum, while does not add more combination sites in the bulk. It is found doping TiO_2 with anions such as C [65], N [66], F [67] could shift the valence band upwards, therefore realize the narrowing of the band gap. Self-doped TiO_2 with Ti^{3+} is also studied and it is showed that the photoresponse of TiO_2 from the UV to the visible light region [68]. In addition, composite semiconductor materials (for example CdS/TiO_2 composite [69]) and dye sensitization [70] can also utilize visible light for energy conversion and achieve high photocatalytic activity.

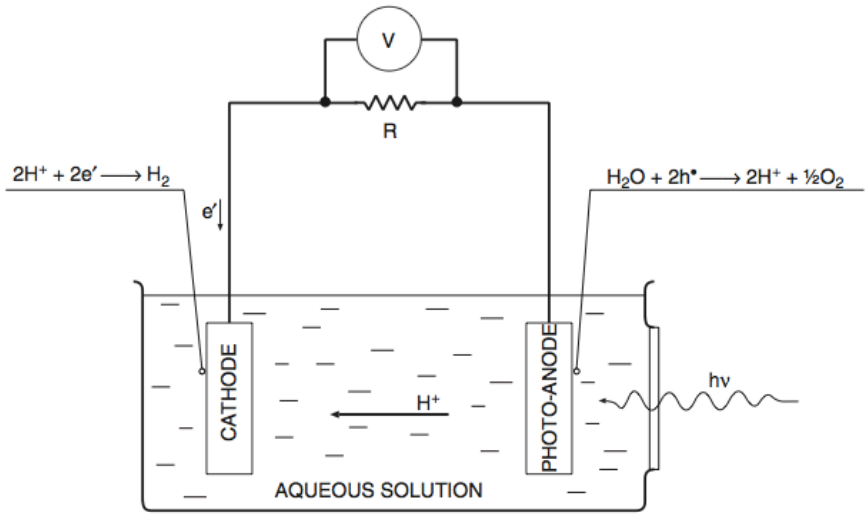

Figure 8. Photoelectrochemical cell (PEC) equipped with a single photoelectrode for water photoelectrolysis [71].

Photoelectrochemical cell (PEC) is commonly used for studying the Photocatalytic performance of semiconducting materials under illuminations. Figure 8 shows a simple PEC model for water photolysis. A PEC is consisted of a photoelectrode (photoanode), a cathode and a reference electrode, and all of the electrodes are immersed in aqueous electrolyte. When the photoanode is exposed to light illumination, there will be charge transport within the PEC and evolution of gases at the surfaces of photoanode and cathode.

Research on the photocatalytic water splitting is a difficult task, although there has been some progress in recent years, a lot of work still needs to be done, such as the development of new photocatalysts with special structure, to improve the photocatalytic performance.

1.4 Photocatalytic Water Purification

1.4.1 Current Water Treatment Technologies

Water is the source of life, and the total amount of water on earth is constant. More than 97% of all the water on the earth is in oceans and seas, which cannot be utilized by human being. The rest is fresh water, out of which approximately 68.7% water is in the form of glaciers and ice caps, and about 30.1% is locked up in the groundwater. Therefore, only about 1.2% of all the fresh water can be used for people's life needs. It has been reported that 4 billion people all over the world are facing the clean water shortage, and there are millions of people died due to waterborne disease every year [72]. With the fast industrialization, more and more clean water source has been polluted by industrial and human activities, therefore, it is necessary to develop technologies to treat wastewater and provide clean water.

Water treatment is a process to remove unwanted harmful substances from different water sources and make the water meet the quality or standards for its intended use. Human beings have conducted water treatment for many years, and one of the earliest water treatment methods is boiling water, which is still widely used nowadays. A wide variety of methods have been developed, such as physical, chemical or biological approaches. Physical methods include filtration and precipitation. Filtration use filters with different pore sizes, which can be used to absorb or blocking the impurities in water. Activated carbon powder, for example, is widely used for absorption of impurities in water. Blocking is to exclude impurities when its size is larger than the pore size of the filter. In addition, physical methods also include precipitation or settling, which utilize

gravity to get rid of heavy pollutant particles on the bottom or light particles on the top of water. Chemical methods are to use a variety of chemicals to change the pollutants in dissolved or suspended states to materials less harmful to human beings or precipitations. The most widely used chemical agents for water treatment are chlorine, chlorine oxide and ozone. However, during the disinfection process using these chemicals, secondary contamination might be introduced into the water system. By-products such as trihalomethanes, halo-phenols, ketones, aldehydes are produced with the elimination of the original pollutants, and a lot of the by-products are proved to be carcinogenic and mutagenic [73-75]. Biological treatment is a process of biological degradation of pollutants into carbon dioxide, water and nitrogen. In the biological treatment process (for example, activated sludge and lagoon systems), bacteria and algae are usually used to metabolize organic matters in the wastewater, and additional treatment methods may be added for further treatment. Besides, there are a wide variety of water treatment methods used in the recent years, which would be discussed in Table 1 for the comparison between their advantages and disadvantages.

Table 1. Comparison between commonly used water treatment methods.

Treatment process	advantages	disadvantages
Activated Carbon	Applicable to a wide variety of pollutant compounds; Flexible system.	Unable to remove soluble organics; high operation cost.
Chlorination	Effective to remove bacteria, organisms; low cost.	No Nitrate removal; causes smell and bad taste; 2nd contamination.
Ozone	Effective to kill bacteria; no nasty odors; leaves no trace of ozone.	High energy cost; 2nd contamination.
Ultraviolet	Effective to remove bacteria, organisms; no 2nd contamination.	High energy cost; high maintenance cost.
Coagulation by alum or ferric sulphate	Effective to remove inorganic pollutants.	Poor performance to remove organic pollutants.
Reverse-Osmosis	Effective to remove most contaminations.	Not effective to remove small molecules; waste a lot of water.

Although the currently used water treatment methods have been proved effective in reducing most of the contaminations in wastewater, unfortunately, with the development of industrial technology, an increasing amount of new pollutants have been detected from the municipal wastewater, such as the endocrine disrupting compounds from pharmaceuticals and personal care products, surfactants and various of additives to industrial products. The harmful organic compounds have been introduced to rivers, lakes, even our drinking water [76, 77]. These organic compounds cannot be removed by conventional water treatment methods properly or the costs are too high. Therefore, the development of new, high efficient and low cost treatment methods to remove pollutants in water becomes extremely important.

1.4.2 Photocatalytic Water Treatment Technology

In recent years, advanced oxidation processes (AOPs) have demonstrated great potential as a novel water treatment technology. The working principle for AOPs is to generate highly reactive species, such as hydroxyl radical (OH□), to oxidize and degrade organic pollutants. OH□ has been proved effective to mineralize more than 800 compounds to carbon dioxide and water [78]. Besides, the presence of AOPs has eliminated the risk of secondary contaminations produced by conventional water treatment methods such as chlorination. Among the AOPs, photocatalytic semiconducting materials (TiO_2, ZnO, CdS, ZnS) have attracted the greatest attentions for being a low cost, effective approach to decompose organic pollutants.

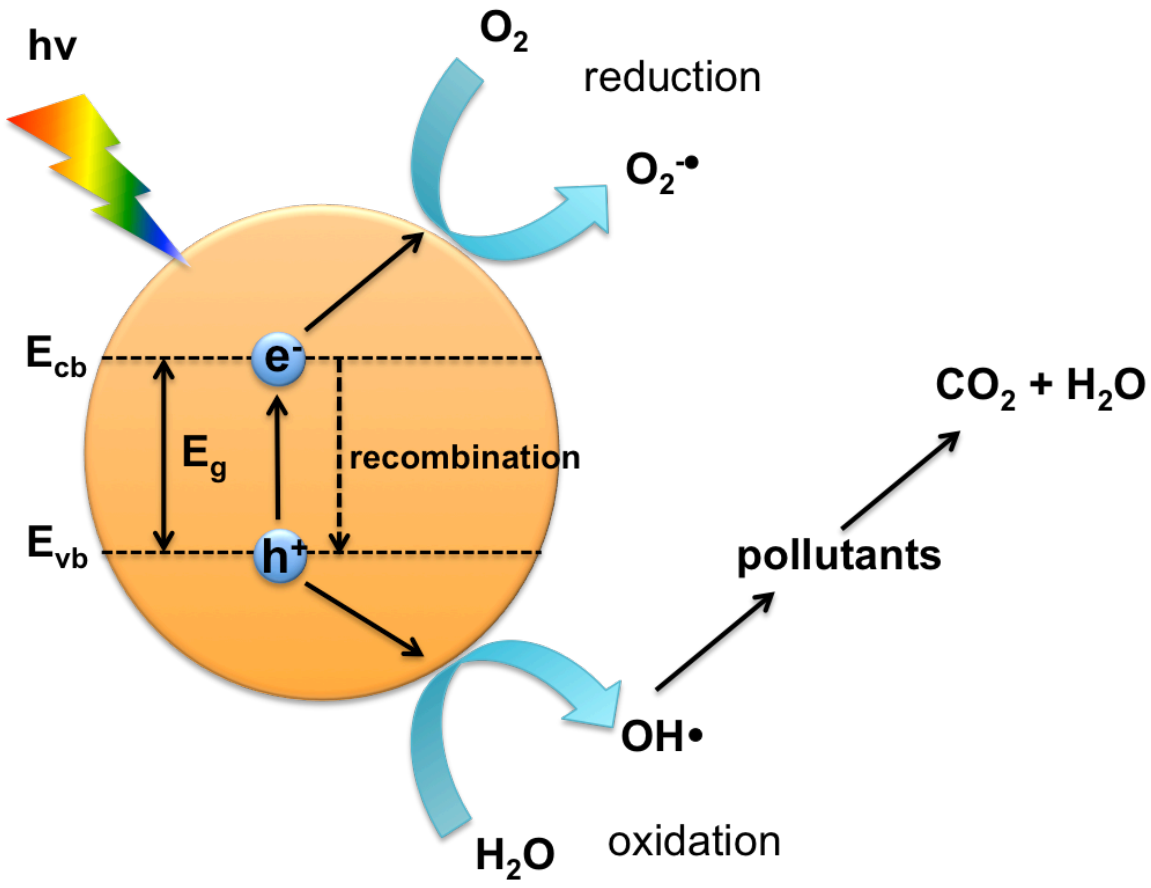

Figure 9. Working mechanism of photocatalytic water oxidation to produce hydroxyl radicals and degradation of organic pollutants to carbon dioxide and water.

Semiconductor materials can be used as photocatalysts is due to their photo-electrochemical properties. Semiconductors are generally composed of low-energy valence band and high-energy conduction band, and the presence between the valence band and conduction band is band gap. As seen in Figure 9, when the light irradiated to the semiconductor has higher energy than the band gap ($h\nu \geq E_g$), the semiconductor will absorb light and produce electron-hole pairs. The water absorbed on the catalyst surface would be oxidized by positively charged hole (h+) in valence band, and subsequently

produce OH□ to mineralize organics into carbon dioxide and water [79], and the holes (h+) can also oxidize the contaminations directly by oxidation reactions [17]. The electrons in conduction band can also be involved in the decomposition of organics by reducing the oxygen absorbed on the surface [79].

In the last 40 years, TiO_2 has been widely studied as a photocatalyst for water treatment due to its photocatalytic activity, stability and inexpensive properties [80, 81]. ZnO has similar properties as TiO_2, and recently, ZnO has attracted more and more attentions and is regarded as a suitable alternative to TiO_2. ZnO has been found to be very efficient in photocatalytic degration of pollutants in the presence of sunlight/UV light as the energy source, and it has been proved that ZnO absorbs over a larger fraction of solar spectrum than TiO_2, which makes it more superior in the photocatalytic application [82-84].

The reactions that conducted during the photocatalytic process would be displayed in Eqs (1.4) to (1.12), ZnO would be used as an example of the photocatalyst in the reactions.

$$ZnO + h\nu \rightarrow e^- + h^+ \quad (1.4)$$

$$h^+ + OH^- \rightarrow OH\square \quad (1.5)$$

$$OH\square + Organics \rightarrow CO_2 + H_2O \quad (1.6)$$

$$h^+ + Organics \rightarrow CO_2 + H_2O \quad (1.7)$$

$$e^- + O_2 \rightarrow O_2^-\square \quad (1.8)$$

$$O_2^-\square + H^+ \rightarrow HOO\square \quad (1.9)$$

$$HOO\square + e^- \rightarrow HOO^- \quad (1.10)$$

$$HOO^- + H^+ \rightarrow H_2O_2 \quad (1.11)$$

$$e^-_{CB} + h^+_{VB} \rightarrow e^-_{VB}\, h^+_{VB} + \text{heat} \quad (1.12)$$

After the photo-excited electrons are produced, the electrons and holes can transfer to ZnO surface to undergo reduction or oxidation reactions, shows in Eqs (1.4)-(1.10). However, not all of the electrons and holes can be used for pollutant degradation, a large portion of the photo-excited electrons would recombine with the holes in valence band and release heat during the recombination process (Eq (1.11)) due to surface or bulk defects or insufficient electron donors and acceptors.

The overall photacatalysis reactions are limited by several independent steps. (1) Mass transfer of the pollutant materials from the solution to ZnO surfaces, (2) the absorption of the pollutants to ZnO surface, (3) photocatalysis reaction, (4) the desorption process of the degraded intermediates (CO_2) from ZnO surface, (5) mass transfer of the intermediate materials from the surface to the solution [16]. The photocatlytic performance is limited by the slowest step, and among these five procedures, the rate limiting step is always considered to be the photocatalysis process, which is hindered by the scanvage of electron and holes during the transfer towards ZnO surfaces. Therefore, the production of materials with excellent charge transfer is one of the most effective methods to increase the photocatalytic performance.

1.5 Semiconductor Materials for Solar based Technologies

1.5.1 Zinc Oxide (ZnO)

Zinc Oxide (ZnO) is a very common material in our daily life. It has been used in paints, ointments, rubber, plastic, ceramic, cosmetics and food as additives. In recent years, ZnO has attracted growing attention for its unique semiconducting properties such as high exciton binding energy (60meV), high optical transmittivity and high conductivity, good charge carrier transport properties and high crystalline quality [85]. ZnO is a II-IV compound semiconductor whose ionicity resides at the borderline of ionic and covalent semiconductors. The crystal structures shared by ZnO are hexagonal wurtzite (B4), cubic zinc blend (B3), and rock salt (B1), as seen in Figure 10. In both wurtzite and zinc blend structures, zinc and oxide atoms are tetrahedral coordinated, and for rocksalt structure, zinc and oxide centers are octahedral. The wurtzite structure is the most thermodynamically stable phase at ambient conditions and thus most common, the cubic zinc blend structure can be obtained by growing on cubic substrates, and cubic Rocksalt structures can be achieved by producing ZnO under relatively high pressures [86, 87].

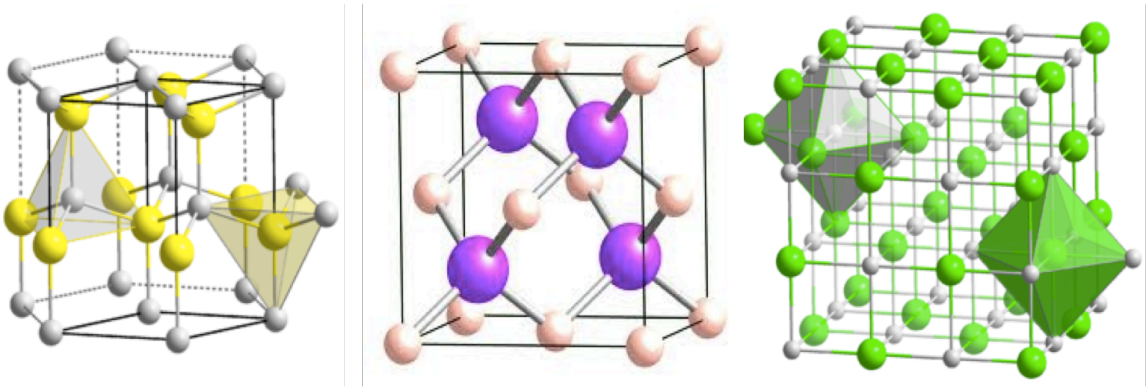

Figure 10. ZnO crystal structures presented in stick and ball models: (a) hexagonal wurtzite, (b) cubic zinc blende, and (c) cubic rocksalt. The big spheres and small spheres indicate Zn and O atoms, respectively.

Wurtzite ZnO structure has a hexagonal unit cell without inversion symmetry, and there are two lattice parameters for its unit cell, a=3.25A and c=5.2A, with a ratio of c/a≈1.633. Wurtzite ZnO belongs to the point group of 6mm or C_{6v}, and the space group of C_{6v}^4 or $P6_3mc$. The schematic representation of the wurtzite ZnO structure is shown in Figure 11. Zinc (0001) and oxygen (000-1) planes bear positive and negative electric charge respectively, due to the polar Zn-O bonds, and these crystalline facets have high surface energy, while the six prismatic (10-10) planes are low surface energy nonpolar surfaces.

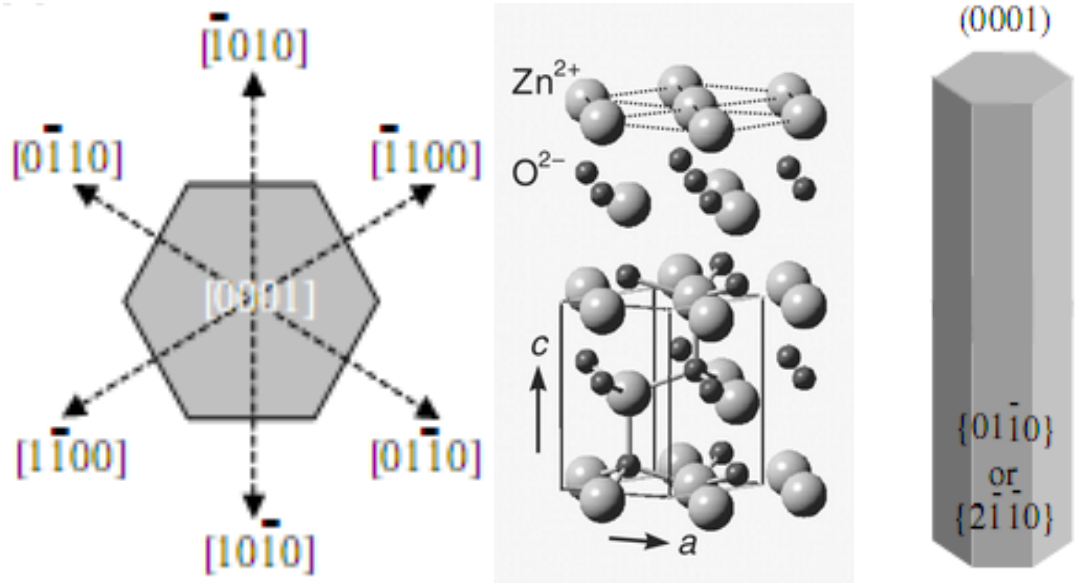

Figure 11. Hexagonal wurtzite sturcutre of ZnO crystal.

ZnO exists as mineral zincite in nature. However, most ZnO is produced through synthesis. It has been grown via a wide variety of methods, such as hydrothermal synthesis [88], sol-gel processing [89], chemical vapor deposition [90], solution-based methods [91]. With these techniques, nanostructured ZnO can be synthesized into a wide variety of structures, such as nanoparticles, nanorods [92], nanotubes [93], nanobelts [94], and hierarchical structures. The properties of nanostructured ZnO closely depend on its phase, size and morphology, and therefore, ZnO serves a wide variety of applications for electronics, photonics, acoustics and sensing areas [85].

1.5.2 Titanium Dioxide (TiO_2)

Titanium dioxide, as a stable, non-toxic, low cost semiconducting material, has been widely used for years in a variety range of applications such as paints, cosmetics

and food coloring. Similar to zinc oxide, TiO_2 has become one of the most promising materials in recent decades due to superior semiconducting properties, and it has presented great potentials for photovoltaic and photocatalytic applications.

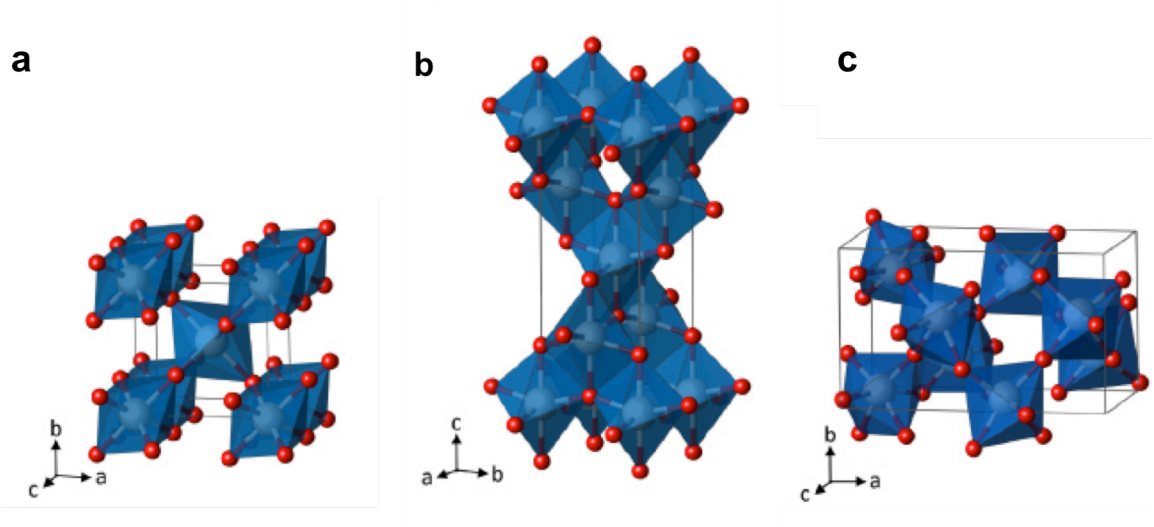

Figure 12. Building-block representation for the TiO2 phases rutile (a), anatase (b) and brookite (c) (Ti (white); O (red)).

TiO_2 naturally occurs in the form of three phases: rutile, anatase and brookite. All the phases above contain octahedral coordinated titanium, as shown in Figure 12. The lattice parameters is a = b = 4.5937 Å, c = 2.9581 Å for rutile, a = b = 3.7842 Å, c = 9.5146 Å for anatase and a = 9.16 Å, b = 5.43 Å, c = 5.13 Å for brookite [95]. Rutile, anatase and brookite belong to the space groups of P 4/mnm, $I4_1/amd$ and P cab respectively. And the band gap for these three phases are rutile: ~3.0 eV [96], anatase: ~3.2 eV [97] and brookite: ~3.14 eV [98]. The most common form is rutile, which is also the most thermodynamically stable phase at all temperatures. The metastable anatase and

brookite phases both could transform to rutile upon heating. For nanoparticles with sizes less than 50 nm, anatase is the stable form due to low surface energy, but transforms to rutile at temperatures higher than 973K. It is generally reported that anatase exhibits superior photocatalytic activity to rutile as a result of a significantly higher surface area and thus higher levels of adsorbed radicals, although anatase has larger band gap than rutile [51]. There are several publications claiming a combination of anatase and rutile shows the optimum photocatalytic activity [99, 100].

TiO_2 can be synthesized by a number of different methods. Chemical and physical vapor deposition are effective methods for producing high purity and crystallinity, however, high temperatures (1200°C to 1600°C) are normally required for these techniques [101, 102]. TiO_2 can also be achieved by low temperature solution-based methods such as hydrothermal method (<300°C), which is advantageous for its environmental friendly and low cost properties. And the products obtained via this route can be easily tuned by adjusting the reaction conditions like pH, precursor concentration, temperature, time, etc [103, 104]. In addition, sol-gel method [105], sintering [106], electrodeposition [107] and microwave methods [108] are widely used for controlling the size, phase and morphology of TiO_2 for various of applications.

1.6 Objectives

The increase of energy demands drives the need for efficient and inexpensive energy conversion devices, such as dye-sensitized solar cells and solar hydrogen generation. In addition, water pollution caused by industrial activities and our daily

abuses is also a big concern. New water treatment technologies such as photocatalytic devices are promising to be implemented to remove hazardous compounds for purified drinkable water. These devices require precision over their constituent materials. ZnO and TiO_2 are good candidates for these applications. However, traditional processing methods of these semiconducting materials yield structures with poorly controlled structures.

Our research focus for this thesis are: (1) Understand the effects of synthesis reaction conditions on the resulting semiconducting materials; (2) understand the nucleation and growth mechanism of nanostructured materials; (3) understand the structure-function relationship between the metal oxide materials and their photovoltaic or photocatalytic applications.

1.6.1 Specific Objectives for Bio-inspired ZnO Nanostructures for DSSCs

Based on inspiration from Nature, which can produce elegant structures at room temperature through controlled organic-mineral interactions, we utilize organic agents to mimic the organic-mineral interactions process, to synthesize ZnO nanostructured materials under mild solution conditions with controlled size, shape and orientation. Specifically, we utilize functional organic materials to direct the growth of ZnO nanostructures under hydrothermal/hydro-solvothermal conditions. The significance of our research is that we utilize what we have learned from Biology and use it for Solar-based technology, which is a cost-effective and environment friendly process.

Objective 1: Investigate the crystal growth behavior of ZnO nanostructures synthesized by hydrothermal methods, and understand the effects of reaction conditions on the resulting materials.

We have successfully synthesized ZnO highly branched nanostructures by using hydrothermal/solvothermal method. Reaction conditions such as precursor concentration, reaction time and ratio between precursor to organic additive have been systematically studied to determine synthesis-structure relationships, which would help us to guide further synthesis of ZnO nanostructures with precisely controlled size, shape and orientations.

Objective 2: Understand the growth mechanism of ZnO highly branched structure.

We have investigated the formation process of the highly branched structure by conducting a time study. Detailed characterization techniques were used to interrogate the nucleation and development of the branched structures.

1.6.2 Specific Objectives for ZnO-carbon Composite Materials for Photocatalytic Water Treatment

Water pollution caused by industrial activities and our daily abuses has become a big concern. New water treatment technologies such as photocatalytic devices are promising to be implemented to remove hazardous organic compounds for purified drinkable water.

Objective 1: Developed a novel synthesis method to produce ZnO-carbon composite materials.

Based on inspiration from Nature, organic agents are used to mimic organic-mineral interactions to yield ZnO-organic composite materials under mild solution conditions. The organics offer the potential to modify ZnO crystal nucleation and growth behavior, and provide the source for carbon. In fact, as-synthesized composites are subsequently annealed to form a ZnO-carbon composite structure.

Various preparative parameters, such as initial reactant concentration, precursor salts and pH have been systematically examined. At different pH, the zinc precursor has different interaction with the functional groups in the solution, thus different ZnO-carbon nanostructures were produced. Different graphitic carbon amounts in the resulting composite materials can be achieved by adjusting the annealing temperature and time. By understanding the mechanism of ZnO-carbon formation process, through a tuning of initial parameters, we can exert control over nanostructural size and morphology to affect the optoelectronic and chemical properties.

Objective 2: Study the structure-function relationship by its performance in photocatalytic organic compound degradation.

The presence of this graphitic carbon will expedite the electron transport, and therefore reduce electron-hole recombination within ZnO. The photocatalytic performance of these ZnO-C nanostructures have shown promising results in exhibiting higher degradation rates than without carbon.

1.6.3 Specific Objectives for TiO_2 Solar Hydrogen Generation

With the increasing demands of energy in our life, solar hydrogen has become an attractive approach to provide renewable energy by utilizing solar energy. TiO_2 has been

considered the most promising candidate for photocatalytic water splitting due to its superior semiconducting properties, and also it is inexpensive, stable and easy to manufacture. In this work, TiO_2 nanowires growing on novel templates have been applied for the photocatalytic water splitting. And it has been proved that the photo-electochemical activity of TiO_2 can be affected by its crystallinity, surface structure, morphology, size and orientation. Therefore, a comprehensive study of the structure-performance relationship is necessary and important.

Objective 1: Uncover the formation mechanism of TiO_2 nanowires on novel templates, and investigate the processing effects (such as template surface chemistry, template orientation and precursor diffusivity) on the development of TiO_2 nanowires.

The diameter and density of the nanowires can be controlled by tuning the surface chemistry of the templates, such as changing the grain size of the templates or creating oxygen vacancies on the surface. The wire orientation was tuned by homo-epitaxial growth on templates, and the electron conductivity have shown different rate in different orientations. The tip sharpness of the nanowires was adjusted by limiting the precursor diffusivity in the solution. Also, Kinetic experiments were performed to identify the mechanism of the nucleation and growth of the nanowires on the templates.

Objective 2: Determine the structure-performance relationships between TiO_2 and the photacatalytica water splitting performance.

Here, we investigate how the surface chemistry of the template, the length of the nanowires and the density of the nanowire can affect the performance to reveal the structure-performance relationships.

Chapter 2.

Biologically Inspired Synthesis of Highly Branched Zinc Oxide Nanowires

Wenting Hou, Louis Lancaster, Dongsheng Li, Ana Bowlus, Krassimir Bozhilov, and David Kisailus. Biologically Inspired Synthesis of Highly Branched Zinc Oxide Nanowires, *Bioinspired, Biomimetic and Nanobiomaterials,* **3** (1) (2013) 10-18. DOI: 10.1680/bbn.13.00019.

ABSTRACT:

Biological mineralization demonstrates how Nature can produce elegant structures through controlled organic-mineral interactions. These organics are often used to control shape, size and orientation of mineral. Based on inspiration from Nature, we utilize an organic agent, Ethylenediamine (EDA), as a mineralizer to inhibit rapid hydrolysis and condensation of ZnO, and thus control crystal growth behavior. Through adjustment of various parameters, such as precursor concentration as well as the molar ratio of the inorganic precursor and organic ligands, we investigate the mechanism of formation of highly branched ZnO nanostructures, which can be used for improving efficiency energy conversion and water purification applications.

2.1. Introduction

Due to the increasing demand for energy as well as environmental pressures caused by the use of fossil fuels, significant research has been focused on the development of alternative renewable energies, such as wind power, solar energy and biofuels [109]. Among all the renewable energy technologies, solar energy, a carbon-neutral process, is considered the ultimate solution to replace fossil fuel and solve many environmental challenges. Dye Sensitized Solar Cells (DSSCs) are a low cost option for efficient solar-to-electrical power conversion. DSSCs, which utilize the photo-excitation of dye molecules adsorbed on the semiconductor materials [30-32], achieve an overall conversion efficiency of 11.4% [31, 110, 111]. This enables them to compete with commercialized high cost solar cells (i.e., silicon and compound semiconductor-based devices) [32]. However, the conversion efficiency of DSSCs has been limited due to

electron recombination in the bulk and at the interfaces of the electrodes as well as a limited coverage of electron producing dye molecules. A material with a high surface area and electron mobility would enable more photoabsorption and reduced recombination, respectively. ZnO, a II-VI compound semiconductor with a direct bandgap of 3.37 eV, a high exciton binding energy (60meV) [86, 112], and an electron mobility as high as 2000 [112, 113], is a promising candidate compared to TiO_2 [113, 114]. Besides being useful in DSSCs, ZnO has significant potential in sensors, ultra-violet laser diodes and photocatalysts [85, 86, 115]. To improve performance in theses applications, numerous efforts have been made to synthesize ZnO with different structures such as nanoparticles [116], nanowires [40, 117], nanotubes [118] and thin films [119, 120]. Morphology, crystallinity and orientation of ZnO crystals have a strong effect on its resulting optoelectronic properties [121]. For example, nanoparticulate networks with disordered pore structures have been observed to exhibit slow electron transport kinetics due to formation of electron traps at the contacts between nanoparticles. Conversely, aligned single crystalline nanowires are promising for fast electron transportation due to lack of grain boundaries acting as traps [117, 122] and thus, the replacement of nanoparticles with nanowires have shown an enhanced electrical conductivity [40, 117, 122]. Although the nanowires show better electron transport kinetics, they have a reduced surface area, which also limits their utility in devices (e.g., the amount of dye sensitizer molecules in DSSXs that can be absorbed is limited). Thus, in order to enhance performance, it is necessary to produce ZnO nanostructures with both good electron transport and high surface area [123].

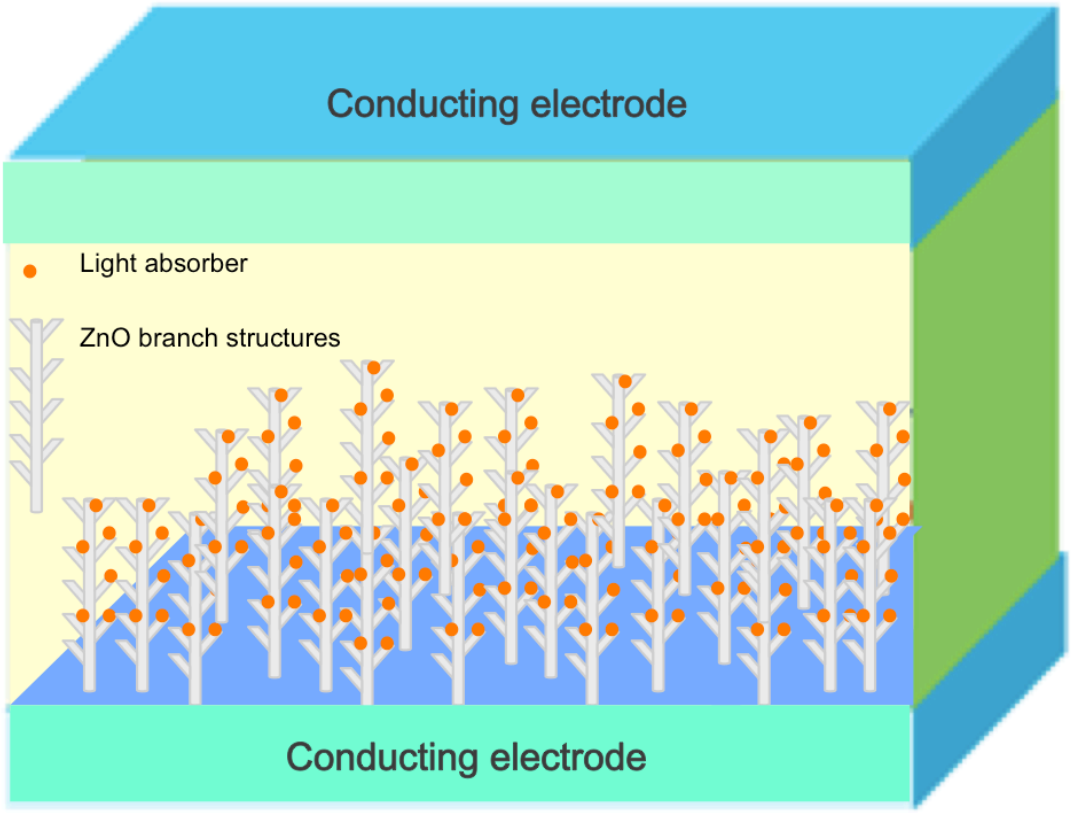

Figure 13. DSSC model showing the semiconducting materials with good electron transport and high surface area.

ZnO can be synthesized by a variety of methods including physical [124] or chemical vapor deposition [125, 126], which require extreme conditions like high temperature or high vacuum to achieve the desired crystallite size and phase. Solution routes such as chemical bath deposition [127, 128], sol-gel synthesis [89] and hydro/solvothermal methods [129] utilize relatively mild temperatures and pressures, which translate to low cost. However, these methods often lack precise control over size and morphology of the resulting crystals. Over billions of years, Nature has evolved to produce elegant structures that

serve highly specified functions. This is exemplified in biomineralized organisms, which are able to spatially control nucleation, mineral size, shape, growth orientation and phase [130, 131]. These organisms can do this by utilizing organics as templates, which guide mineral formation (e.g., calcite [132-134], iron oxide [135] and silica [136], with an incredible precision and fidelity, under mild conditions (room temperature and near-neutral pH). During the growth, ions or clusters that constitute these minerals interact with the organics, and subsequently grow in a directed fashion, yielding different morphologies. Based on inspiration from these biological minerals, we utilize functional organic moieties to direct the growth of ZnO under hydro-solvothermal conditions. We investigate how modified solution parameters affect the growth and branching of nanocrystalline structures.

2.2. Experimental Section

ZnO nanostructures were synthesized under hydro-solvothermal conditions in 23 mL Teflon liners. Concentrated precursor solutions of zinc were prepared by dissolving zinc nitrate hexahydrate ($Zn(NO_3)_2 \cdot 6H_2O$, 98%, ACROS) and sodium hydroxide (NaOH) in Milli-Q water to form an aqueous precursor solution (molar ratio $[Zn^{2+}]$:[OH]=1:20). Mixtures of water/ethanol (16.7/83.3 vol%) were used as co-solvents and ethylenediamine (EDA) was added as a mineralizer. Specific quantities of the precursor solution were added to the water/ethanol co-solvents to make different concentration zinc nitrate solutions. Subsequently, different amounts of EDA solutions were added into the solutions. The final solution precursor mixtures (i.e., $Zn(NO_3)_2$, EDA, water and ethanol)

were placed into 23 mL Teflon-lined autoclaves (Parr Instruments, Moline, IL), sealed and placed in convection ovens at 180°C for different durations (10 minutes - 20 hours). After the reactions were complete, reactors were removed and subsequently cooled under ambient conditions. The resulting products were then washed three times with DI water and twice with ethanol, with product suspensions being sonicated (Branson 2510, Danbury, CT) between washes to remove any unreacted precursor and reaction by-products. Samples were then dried in air at room temperature.

The resulting ZnO products were characterized using X-Ray Diffraction (XRD, Philips X'Pert), using Cu Kα radiation (λ = 1.5405 Å) for phase analysis. Structural analyses were conducted using Scanning Electron Microscopy (SEM, Philips FEI XL30) at 10kV accelerating voltage, Transmission Electron Microscopy (TEM, CM300) operated at 300kV. Chemical analysis was conducted by Fourier Transform Infrared Spectroscopy (FTIR, Bruker Equinox 55, 4000 cm^{-1} to 370 cm^{-1}, step size 1 cm^{-1}). Samples for FTIR were prepared by grinding dried potassium bromide (KBr) with 1 wt% ZnO sample in a mortar and pestle, and drying at 60°C for 4 hrs. 100 mg of the KBr and ZnO powders were subsequently pressed into pellets for FTIR analyses.

2.3. Results and Discussion

2.3.1 Effect of Zn concentration

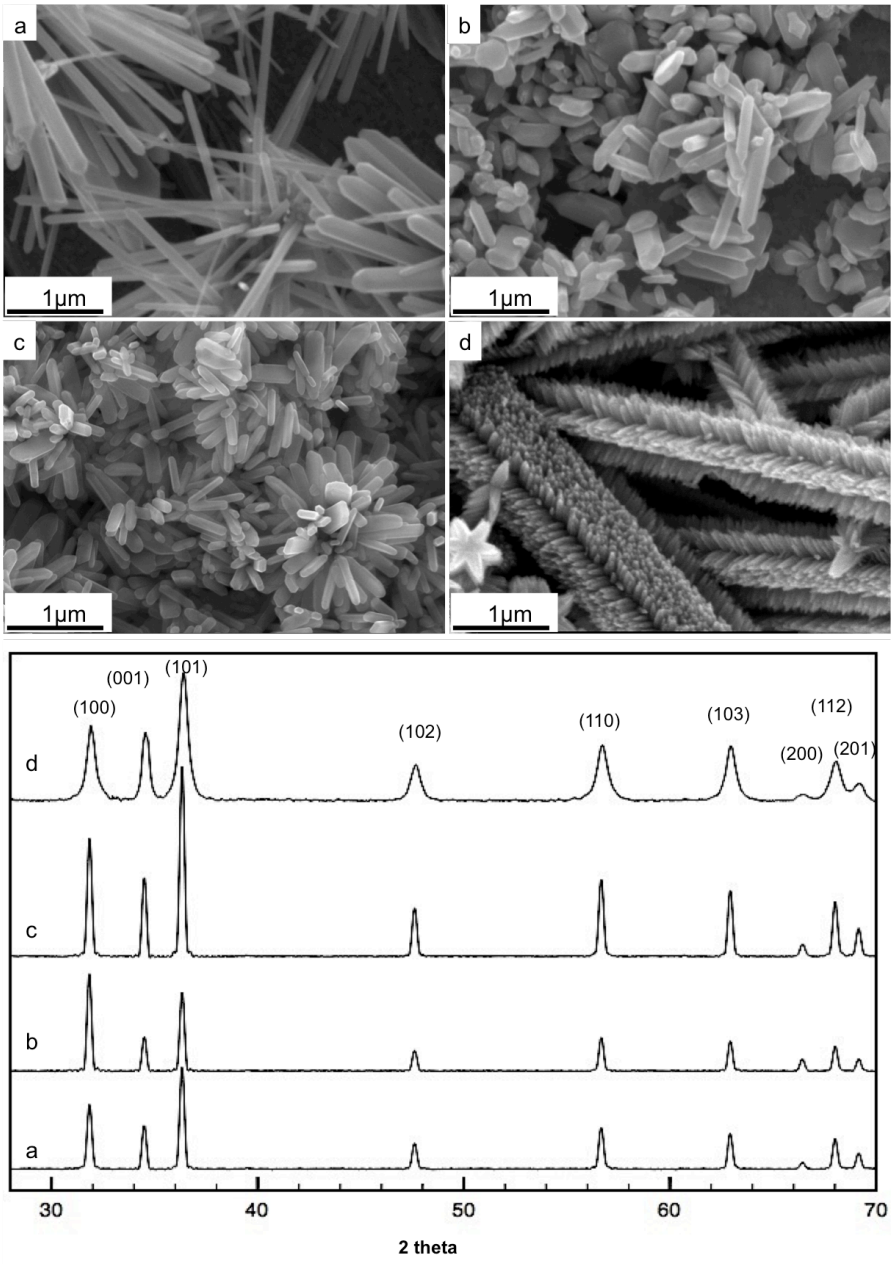

Figure 14. SEM micrographs and XRD patterns of ZnO nanostructures synthesized at 180°C, pH=14 and [Zn]: [EDA]=1:1, at different [Zn] (a) [Zn] = 5 mM, (b) [Zn] = 10 mM, (c) [Zn] = 25 mM, and (d) [Zn] = 50 mM. XRD (bottom) depicts wurtzite ZnO with a decrease in crystallite size with increasing [Zn] (as indicated by the increase in the full width at half maximum of peaks).

The size and morphology of ZnO nanoparticles have a great influence on its optoelectronic properties, which is likely to affect performance in DSSCs [113]. Here, different ZnO nanostructures have been prepared using precursor solutions with different zinc concentrations with EDA as a mineralizer. XRD (Figure 14) confirms that all the samples are in the form of crystalline wurtzite ZnO (JCPDS 36-1415). No additional phases (such as zinc hydroxide) were observed. The crystallinity of the samples decreased from 50 nm (at 5 mM) to 20 nm (at 50 mM), as observed by the increase in the full width at half maximum (FWHM) of the (100) ZnO peak.

SEM micrographs of these structures (Figure 14), revealed obvious differences between the ZnO structures produced using different precursor concentrations. At low concentrations of zinc precursor (5 mM), long (> 3 μm) and smooth ZnO rods formed with diameters between 50 - 200 nm. With increasing precursor concentration (i.e., 10 mM and 25 mM), the length and aspect ratio of ZnO rods decrease from 3 μm and 25 to 500 nm and 4, respectively. When the concentration of zinc precursor is increased to 50 mM, highly branched ZnO rods form (compared to nanoparticles or smooth rods at low concentrations). These ZnO branched structures consist of long (5-10 μm) hexagonal rods with highly condensed, oriented nanobranches growing from its six prismatic (10-10) faces.

At low nutrient concentrations (i.e., low concentration of hydrolyzable species) crystal growth is favorable, whereas at higher concentrations, nucleation dominates. The rate of nucleation increases rapidly with increased precursor concentrations [137]. Therefore, at high concentrations (50 mM), nucleation occurs in a very short period of time,

producing a large number of nuclei, which would not only decrease the crystallite size, but also affect the manner in which the structures grow (i.e., ion by ion versus particulate-based growth). Li et al. have demonstrated that high concentrations of titania precursor lead to spherulitic nanostructures, consisting of a core nanowire with multiple branches that increase in density with increasing titania precursor concentration and time [138]. In our system, it is likely that at higher concentrations of Zn precursor, more nuclei are produced, increasing the probability of a branching event via twinning [139].

2.3.2 Branched Structure Analysis

SEM and TEM analyses were used to further investigate the characteristics of the highly branched structures (Figure 15). SEM observations (Figure 15a, d) show that the core of the ZnO branched nanostructures have diameters between 1 μm - 2 μm, and the secondary rods (i.e., branches) are approximately 40 nm in diameter.

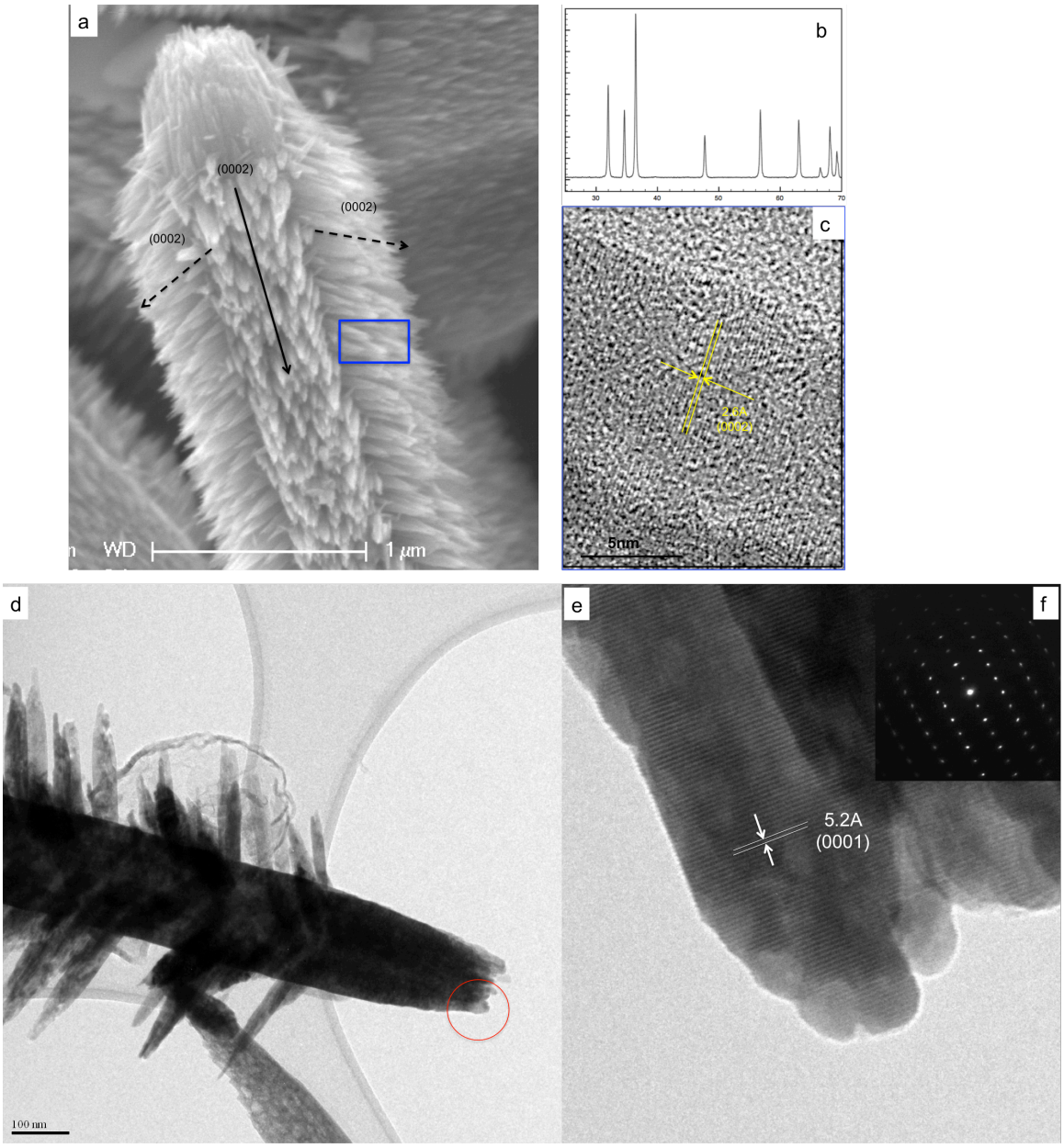

Figure 15. Analysis of branched structures: SEM micrograph (a) highlighting the secondary branches growing from the prismatic faces of the core rod. XRD pattern (b) confirmed wurtzite ZnO. HRTEM of a branch (c) uncovering the growth direction of the branch (i.e., along <0002>. TEM micrographs and electron diffraction pattern (d-f) demonstrate the branches, their growth direction and crystallinity.

A SEM micrograph taken perpendicular to the long axis of the ZnO branched structure (Figure 15a) indicates the secondary rods grow from the prismatic (10-10) planes. HRTEM analyses of the secondary rods (Figure 15c) revealed that the d-spacings along the length of the branches correspond to ZnO <0002> direction, confirming their growth direction. TEM analysis (Figure 15d) of the branched ZnO nanowires confirmed the branch diameters (i.e., 20-40 nm). HRTEM (Figure 15e) highlights the tip of main rod in Figure 15d, on which there are thinner ZnO nanorods observed attached to each other to form a larger rod. The tips of these rods also appear to consist of nanoparticles. Selected area electron diffraction (SAED) (Figure 15f) of the tip of the rod reveals its single crystalline nature, implying that the smaller crystalline rods of ZnO are formed from nanocrystallites, which are oriented along the same crystallographic direction [127, 138, 140].

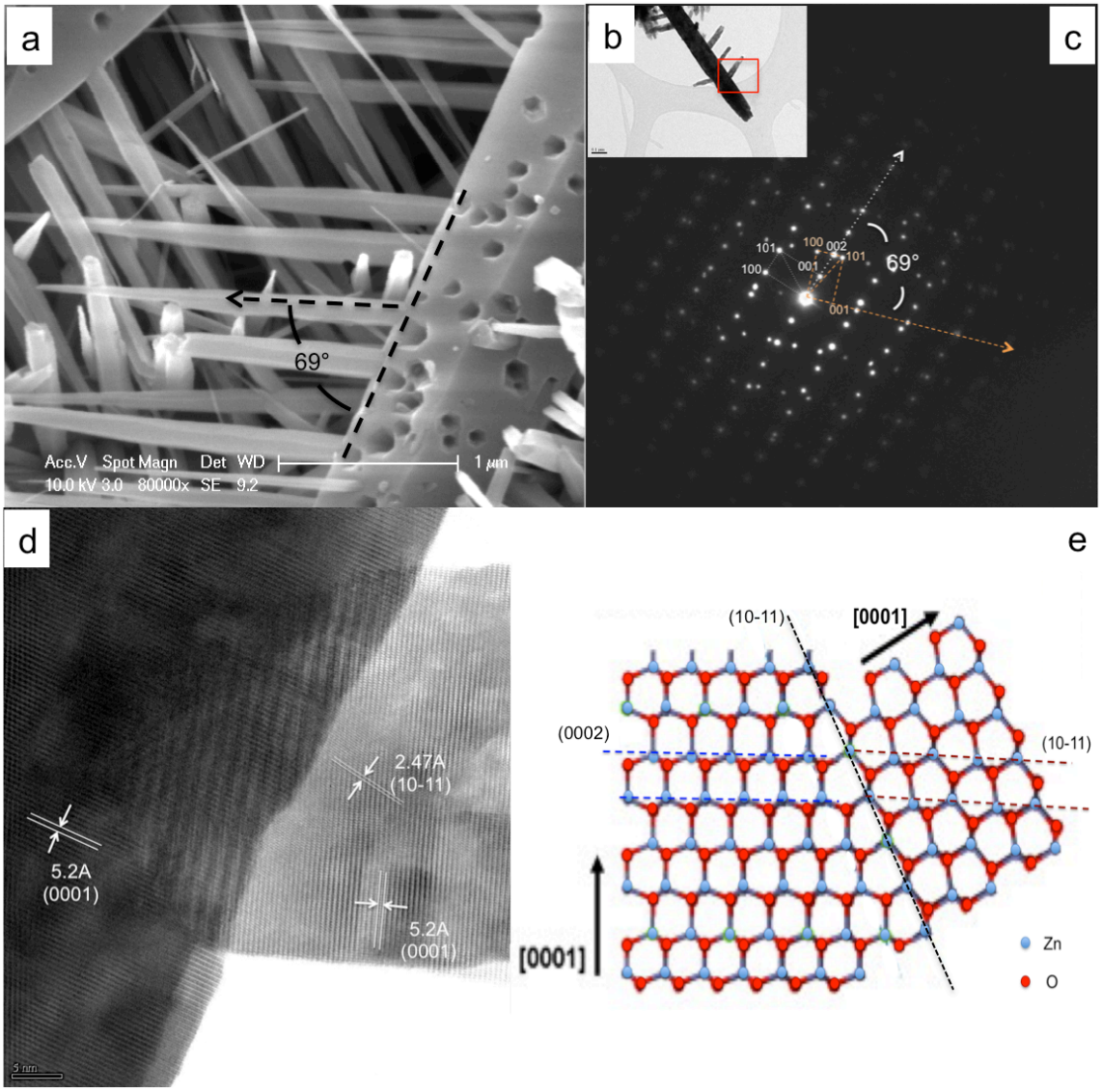

Figure 16. Analysis of branched structures: SEM micrograph (a) highlighting the secondary branches growing from the prismatic faces of the core rod. Bright field TEM (b) highlighting the region of the branched rod interrogated by SAED (c), which reveals the angle between the primary rod and branches. High resolution TEM micrographs (d) showing the formation of the branch along the semipolar surface. An atomic model (e) indicating the interface between the core rod and a secondary branches.

SEM analyses (Figure 16a) demonstrate pores on the prismatic surfaces of the primary rod and shows the angle between the branches and the core rod is about 69°. The

presence of these pores provides hints about the growth mechanism of the branches, as the pores reveal locations of interfaces between the branches and the main rods. It is likely that during the rod growth, particles that are formed in solution may impinge on the growth front, forming twin boundaries with the main rod and acting as branch points. Similar observations have been made in highly branched TiO_2 nanostructures [138]. The presence of pores could have formed due to a number of reasons. One possibility is the etching of highly defective regions where branches had formed, yielding pores with hexagonal shapes [141]. Another possibility is the incomplete branch formation or branches which may have initially formed and subsequently fractured due to growth stresses from the primary rod growth outward from the prismatic (i.e., (10-10)) planes. Closer observation of Figure 16a reveals that the pore diameter increases away from the core rod. This could indicate that branches are formed early and continue to grow in diameter, but have limited growth near the core rod, as they are encased due to lateral growth of the primary rod. Further analyses of the pore formation are needed to explain this phenomenon. SAED (Figure 16c), conducted on a region consisting of the main rod and a branch (Figure 16b, highlighted area), demonstrated both were single crystalline, with the angle between their growth direction measured at approximately 69°, in agreement with our SEM observations. HRTEM (Figure 16d) analysis at the interface of a branch and the core region revealed the lattice spacing of the core rod is 0.52nm, while the d-spacings of the branched region are 0.52nm (along the long axis of the branch) and 0.247nm. This confirms that the core rods grow along [0001] direction, and the branches that grow from the (10-10) plane also grow in the [0001] direction. The boundary between the main rod

and the branched structure is the (10-11) plane in the main rod, which is demonstrated by the dotted black line in Figure 16e. The (0 0 0 1) growth plane, which consists of an alternative stacking of Zn^{2+} and O^{2-} ions, is a polar surface and is known to have the highest surface energy and therefore exhibits a high growth rate. The (10-11) plane consists of a semipolar surface with a short distance between Zn^{2+} and O^{2-} ions. Therefore, it is possible to change the stacking direction of the Zn^{2+} and O^{2-} ions along the (10-11) plane [142]. The branch growth was attributed to the mismatch (<5%) between the (10-11) and (0002) lattice spacing [143, 144], highlighted by the atomic model (Figure 16d, e). Here, the blue dotted lines represent (0002) plane and the red dotted lines correspond with the (10-11) plane in the branch. Based on a crystallographic analysis of the ZnO system, the angle between the [0001] and [10-11] directions is approximately 62°. Our observations (Figures 16a, c, and d) show this angle to be ~ 69°. This difference in angle rotation might be caused by a small twist of the c-axis in the branch between (10-11) and (0001) planes [143-145].

2.3.3 Growth Mechanism

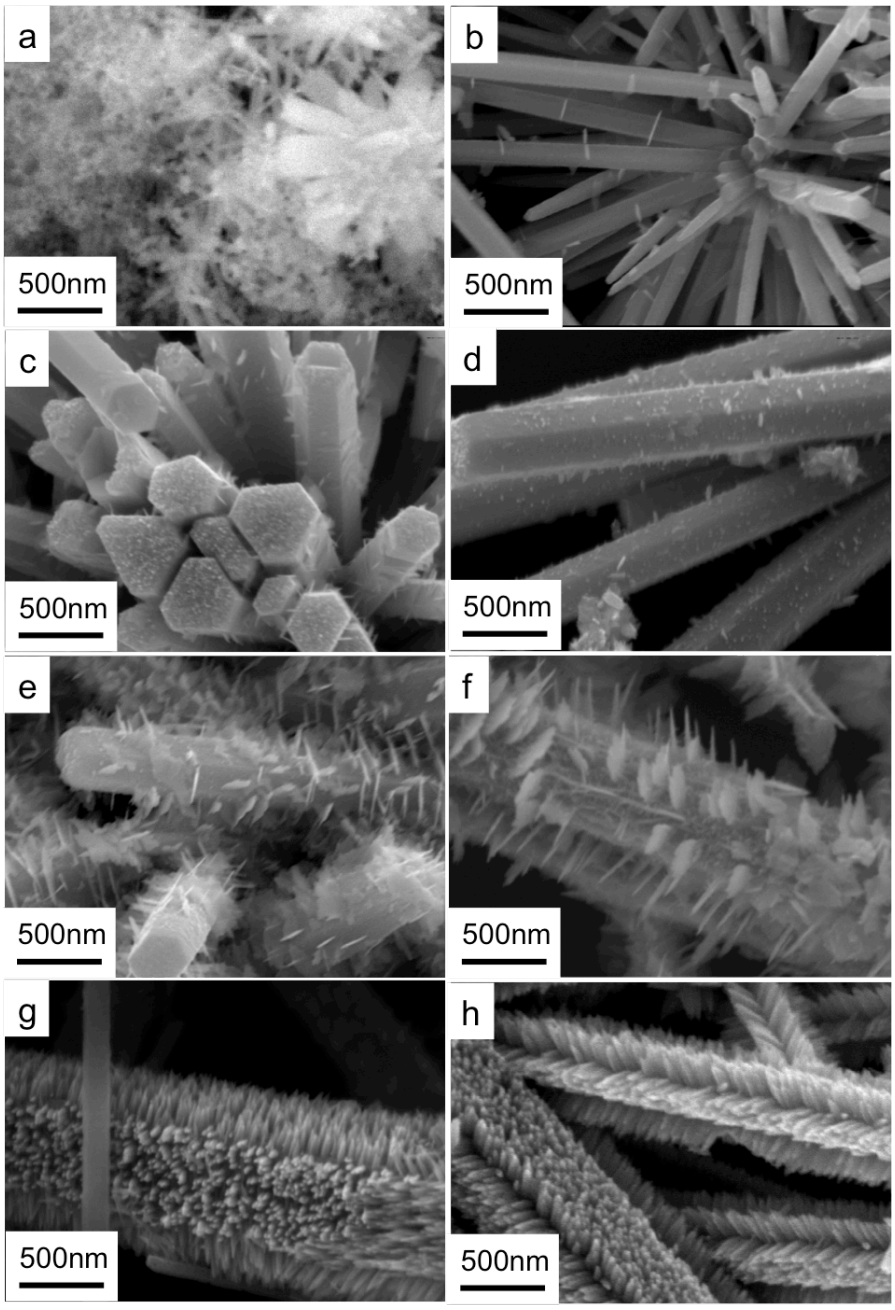

Figure 17. SEM micrographs of branched ZnO nanostructures at different reaction times: (a) 10 minutes, (b) 30 minutes, (c) 1 hour, (d) 2 hours, (e) 5 hours, (f) 10 hours, (g) 15 hours, and (h) 20 hours.

A time study (from 10 minutes to 20 hours) was performed to observe the formation of the branched structures. Based on our observations (SEM), it is clear that at very short times (i.e., 5 min, Figure 17a), nanowires form concurrently with large numbers of nanoparticles. The sizes of the nanowires ranges from 50 nm to 200 nm, while the sizes of the nanoparticles are approximately 20 nm. At longer durations (i.e., 10 min and 30 min, Figures 17b and c, respectively), a primary hexagonal rod (d = 200 nm at 30 min, d = 400 nm at 1 hr) initially forms with minimal branching (< 3% of the surface). By 5 and 10 hours (Figure 17e and f, respectively), a significantly higher density of branches has formed (20% of the surface) on the six prismatic (10-10) faces. Some of these branches are plate-like, since the needle-like branches (30 nm diameter) can fuse together [129]. After 15 hours (Figure 17g and h), all six sides are covered with branches (95% surface coverage).

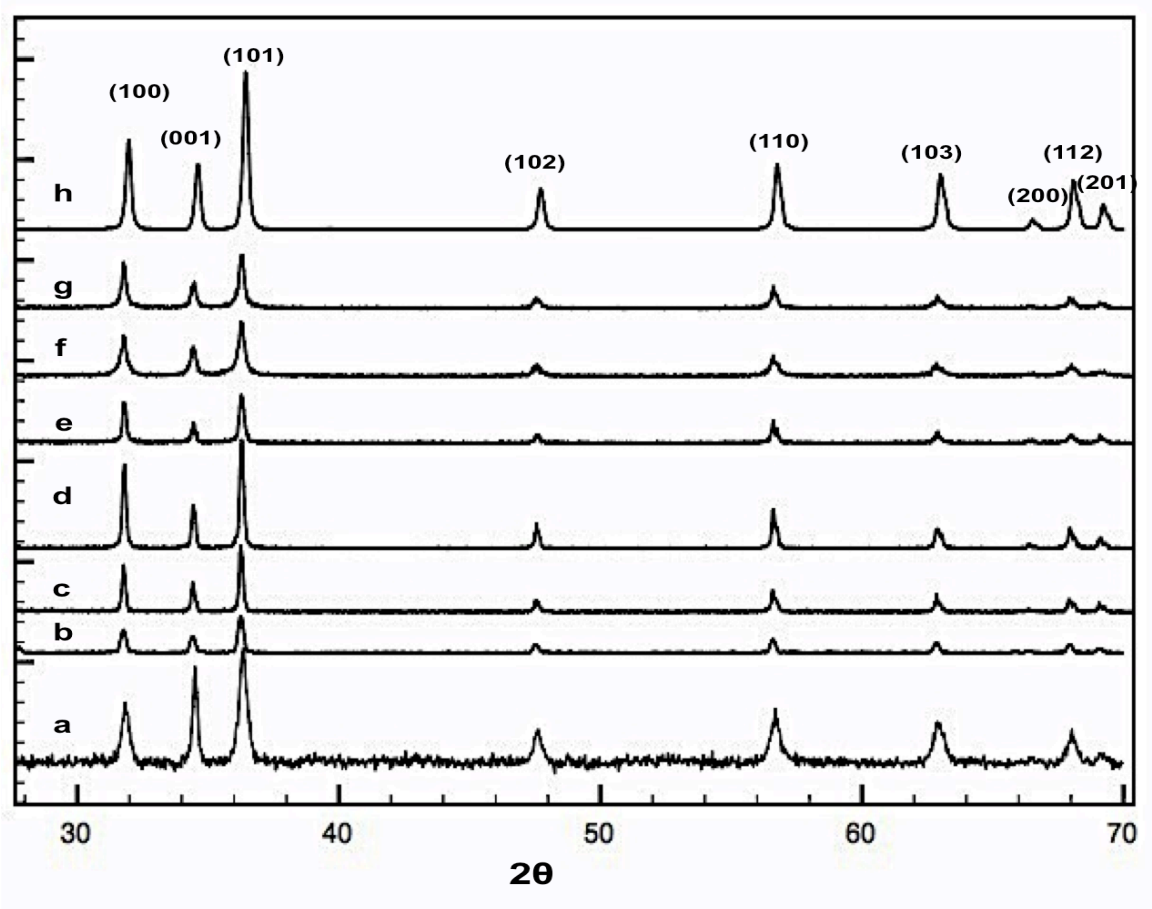

Figure 18. XRD of branched ZnO nanostructures at different reaction times: (a) 10 minutes, (b) 30 minutes, (c) 1 hour, (d) 2 hours, (e) 5 hours, (f) 10 hours, (g) 15 hours, and (h) 20 hours.

During the formation of the branched ZnO structures, it is clear that smooth hexagonal structures form first, with subsequent branching occurring with increasing time. The branches grow from the six prismatic (10-10) surfaces, as seen in the illustration figure 19.

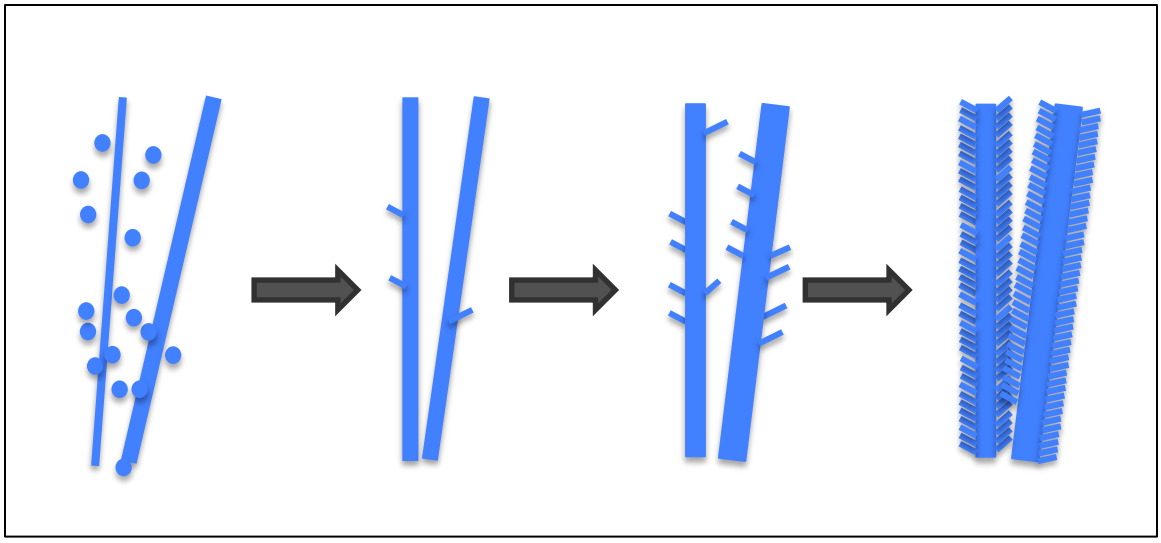

Figure 19. Illustration of the structure evolvement from short time to long time.

To examine the role of EDA, which may play an essential role in the formation of ZnO branched structures [141, 146], the morphology of ZnO formed using different molar ratios of Zn to EDA was compared (Figure 20). Without EDA in the solution media, we observe the characteristic hexagonal rod-like structures of wurtzite ZnO. Addition a small quantity of EDA ([Zn] : [EDA] = 1:0.5), induces a slight branching event on the prismatic sides. The density of these branches is maximized at a 1:1 molar ratio of Zn to EDA. Increasing this ratio to 1:2 reduces the branching, while the highest ratio tested (1: 20) yields no branching and a low aspect ratio (i.e., ZnO nanoparticles are produced instead of ZnO rods). Thus, it appears that EDA interacts with either Zn-species or the ZnO nuclei, affecting crystal morphologies. In fact, Liu and Zeng have shown that EDA can bind to the divalent zinc species on ZnO particles, or can form complex with Zn-species in the solution [129, 147].

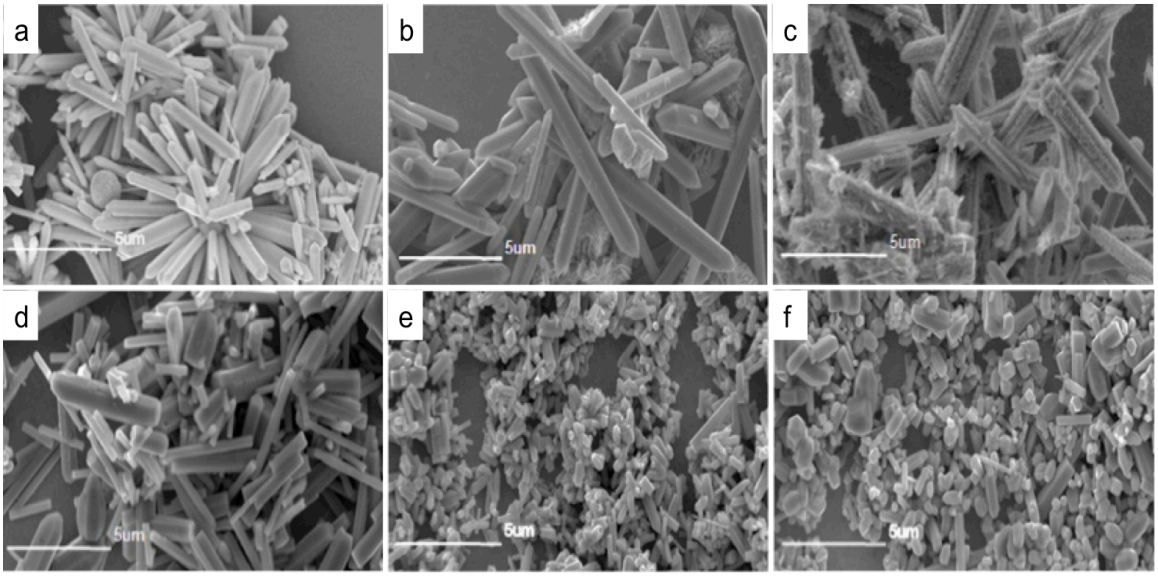

Figure 20. Effect of different molar ratios of Zn^{2+} to EDA on morphology. (a) $[Zn^{2+}]$:[EDA] = 1:0, (b) $[Zn^{2+}]$:[EDA] = 1:0.5, (c) $[Zn^{2+}]$:[EDA] = 1:1, (d) $[Zn^{2+}]$:[EDA] = 1:2, (e) $[Zn^{2+}]$: [EDA] = 1:10, (f) $[Zn^{2+}]$:[EDA] = 1:20. Samples were synthesized at 180°C and pH=14.

The following reactions depict interactions of EDA with the zinc species in aqueous solutions [141, 148]:

$$Zn^{2+} + 4OH^- \rightleftharpoons ZnO + 2OH^- + H_2O \quad (1)$$

$$Zn^{2+} + 3NH_2(CH_2)_2NH_2 \rightleftharpoons [Zn(NH_2(CH_2)_2NH_2)_3]^{2+} \quad (2)$$

$$ZnO + NH_2(CH_2)_2NH_2 + H_2O \rightleftharpoons [Zn(NH_2(CH_2)_2NH_2)_3]^{2+} + 2OH^- \quad (3)$$

In the solution, a variety of zinc complexes are generated. Since there is a high concentration of OH^- ions in the solution, the concentration of ZnO_2^{2-} is very high (supersaturated), leading to fast homogeneous nucleation and growth [121]. In the absence of EDA, most of the Zn^{2+} would be hydrolyzed (i.e., $[Zn(OH)_4]^{2-}$ and subsequently

condensed to form ZnO nuclei [147, 149]. These nuclei subsequently grow into one-dimensional nanorods along the fastest growth direction [0001]. With the addition of EDA, there is a competition between the OH^- ions and EDA for Zn^{2+} cations. Cations that react with OH^- can participate in condensation reactions and form ZnO nuclei. The remaining Zn^{2+} can be chelated by EDA, (a Zn-EDA complex forms when the molar ratio of EDA to Zn^{2+} is higher than three [146]). This soluble Zn-EDA complex would not immediately participate in hydrolysis and condensation reactions and thus, remain in solution.

At temperatures greater than 95°C, the Zn-EDA complex will start to decompose [150] and the equilibrium condition of Equation (2) would shift to the left, resulting in an increase in the concentrations of Zn^{2+} and EDA. The unbound EDA can etch the top and side surfaces of ZnO nanorods and create sites for secondary nucleation (equation 3) [141], yielding the released Zn^{2+} ions susceptible to nucleophilic attack by OH- ions. The soluble Zn^{2+} ions would thus serve as precursor for secondary nucleation of particles, which would impinge on growing rods and lead to branch formation. Thus at low concentrations of EDA (i.e., Zn^{2+}:EDA = 1:0.5), there are few branches on the rod surfaces, while an increase in the density of branches occurs for Zn^{2+}:EDA = 1:1.

Further increases in EDA concentration, (e.g., Zn^{2+}:EDA = 1:10 or 1:20), enables EDA to serve as reservoir for zinc cations [127]. Under certain conditions, EDA is able to compete with the hydroxide ion for free zinc cations to form $Zn[(EDA)_2]^{2+}$ or $Zn[(EDA)_3]^{2+}$ complexes [143, 147]. Therefore, most of the zinc cations are inhibited from hydrolysis at low temperatures and high concentrations of EDA and will thus only be susceptible to

hydrolysis at high temperatures. At high temperatures, the supersaturation level of the zinc cation is significantly higher, resulting in a large number of smaller nuclei, which aggregate to form ZnO nanoparticles rather than long rods or branched structures.

Since the branched structures are affected by the presence of EDA in solution, it is unclear if EDA is either incorporated into or bound to the crystal surface. FTIR (Figure 21) was used to probe the presence of EDA on both smooth ZnO rods synthesized without EDA and branched ZnO structures synthesized with EDA. The strong peak at 470 cm^{-1} corresponds to E_2 mode of hexagonal ZnO, while the peak at 505 cm^{-1} corresponds to oxygen vacancies (V_O) in ZnO [151]. The broad absorptions at about 3400, 1640 and 1410 cm^{-1} are assigned to the hydroxyl groups of chemisorbed and/or physisorbed H_2O molecules on the ZnO surface. The presence of a carboxylate group likely comes from carbon dioxide in the environment [152]. The branched ZnO structures show absorption bands at 1380 cm^{-1} and 3300 cm^{-1}, indicative of C-N and N-H stretches, respectively, confirming the presence of EDA on or within ZnO. EDA is known to be able to bind to the surface of ZnO [146, 147], and the FTIR results verify the incorporation of EDA either within or on the branched structures. Although the presence of EDA is identified with the ZnO product, it is unclear whether its binding plays a role in the branching event or if residual EDA present in solution binds to the surface.

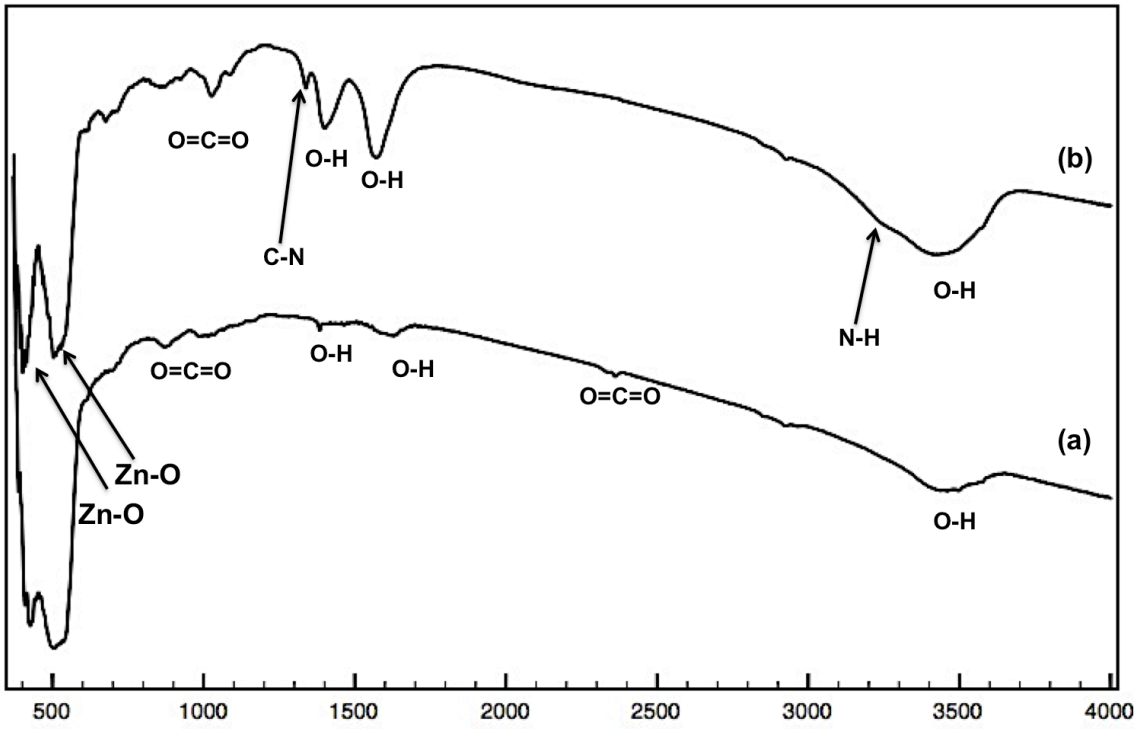

Figure 21. FTIR transmission spectra of smooth ZnO rods synthesized without EDA (a) and branched ZnO structures synthesized with EDA (b).

2.4. Conclusions

We have developed a one-pot solution-based method for branched ZnO rods under relatively mild conditions. The branched structures were modified by using EDA as a mineralizer under different zinc precursor and EDA concentrations. We observed that EDA plays an inhibitory role in nucleation, delaying complete hydrolysis and inducing secondary nucleation after initial formation of primary rods. This secondary nucleation lead to the formation of nanoparticles, which yielded branched structures growing from the prismatic faces of the primary rod. The branches formed via [10-11]

/[0001] twins at the interface with the primary rod. By understanding of the growth mechanism, we can design nanostructures with high surface area for potential enhanced performance in dye-sensitized solar cells, photocatalysts and gas sensors.

Chapter 3.

Synthesis and Performance Test of Titanium Dioxide Nanowires with Controlled Diameter, Morphological Structure and Density via Templating Systems

Wenting Hou, Pablo Cortez, Leigh Sheppard, Rong Liu and David Kisailus. Synthesis and Performance of Titanium Dioxide Nanowires with Controlled Diameter, Morphological Structure and Density via Templating System. Journal of #####

ABSTRACT:

Titanium dioxide nanowires arrays were produced on the surface of polycrystalline TiO_2 templates via hydrothermal reactions. The prepared samples were characterized by X-ray diffraction, scanning electron microscopy, transmission electron microscopy, X-ray photoelectron spectroscopy, and UV−Vis diffuse reflectance spectroscopy. The effects of the reaction conditions and the properties of the templates on the TiO_2 nanowires were extensively investigated and discussed. The length of the nanowires are affected by reaction time, while the diameter and the number density of the nanowires are controlled by the surface properties of the templates, and the tip sharpness of single nanowires is influenced by precursor solubility and diffusion within the solution. Also, TiO_2 nanowires growing on single crystalline templates have been studied with respect to different surface roughness achieved via SIMS. The performance of TiO_2 nanowires for photoelectrochemical (PEC) water splitting was investigated, and it is demonstrated that the photocatalytic activity of the templates are closely related to the nanostructures on the templated surfaces.

3.1. Introduction

There is a continued growth of energy requirement but a dwindling supply of conventional energy sources, and the growing environmental concerns such as greenhouse-gases caused by fossil fuels have posed a prominent risk to our ecosystem. Therefore, the development of highly efficient, clean and renewable energies is important and necessary. Hydrogen, which has long been considered as an efficient and environment-friendly energy carrier, is one of the most promising candidates to replace the conventional fuels. It can be produced from primary sources such as natural gas, oil, coal, nuclear reaction and other renewable energy sources [153]. Among all these production methods, photocatalytic generation of hydrogen from the decomposition of water has been the most attractive one and is a goal of scientists and engineers since Fujishima and Honda first discovered using TiO_2 for hydrogen generation via photoelectrolysis in early 1970s [46, 154]. However, the conversion efficiency of photocatalytic water splitting has been limited due to the electron recombination at the grain boundaries within bulk crystals or between particles [12, 14], and a limited photon absorption in the photoanode materials [12]. In a photocatalytic water splitting reaction, the semiconductor materials that can be used as the photocatalysts are required to have the appropriate band-gap energy, stability toward photocorrosion, be corrosion resistant, cost-effective and environment friendly [12, 155]. Metal oxides such as WO_3 [156], ∂-Fe_2O_3 [157], Cu_2O [158], ZnO [159] and TiO_2 [13, 14] are the best candidates and extensive research has been done to study structure-function relationships.

Single crystalline one-dimensional (1D) semiconductor architectures have widespread utility in applications such as photovoltaic [88, 160], photocatalysis [161], LED [162] and gas sensors [163] due to their superior properties including high surface area, morphological control and charge transportation. TiO_2 nanowires can serve as nanostructured photocatalysts with high surface area for optimized light absorption and direct pathways for charge-carrier transportation [13]. TiO_2 nanowires can be synthesized by a wide variety of methods including physical or chemical vapor deposition [164, 165], which require extreme conditions, such as high temperature or high vacuum, which translate to high cost, to achieve the desired control over size and phase. Solution routes such as chemical bath deposition [166], sol-gel [167] synthesis and hydro/solvothermal methods [168, 169] utilized relatively mild pressure and temperatures. Considerably efforts have been made to produce densely packed nanowires growing vertically from substrates [156, 164]. However, little work has been done on the synthesis of nanowires with controlled orientation and diameter, areal density, and tip sharpness.

Here we produce highly controlled TiO_2 nanowires (TNWs) using a hydrothermal method and a novel TiO_2 templating system. In this work, the diameter, density, aspect ratio, growth direction, and tip sharpness of TNWs can be precisely controlled by tuning the reaction conditions and the template properties. Also, the water splitting performance of the TNWs films are tested and compared.

3.2. Experimental Section

3.2.1 Material Synthesis

1. Preparation of TiO_2 templates

TiO_2 powder sample (commercial TiO_2 powder) is pelletized in an uniaxial press, and re-pressed under high pressure using a cold isostatic press (American Isostatic Presses, Inc). The pellet is polished (LaboForce grinding and polishing machine) to remove scratches on the surface, and then it is transferred to a tube furnace, and treated under high temperature in different gas environments with controlled flow rates for a period of time. After the sintering process, the pellet is cooled to room temperature and cut to the desired shape using a diamond saw (Accutom 5 precision cut-off machine).

TiO_2 single crystal wafers in (100) (001) (111) orientations are purchased and Secondary Ion Mass Spectrometry (SIMS, CAMECA IMS-5F7E) is applied to create craters with a 200μm*200μm dimension. SIMS is normally used for analyzing surface elements and composition. In this work, SIMS is used to create different roughness' on the surface by etching at different time durations. In the process, an oxygen source is applied, with an impact energy of 7.5 KeV, current of 40 nA, and an incident beam angle of 40.2°.

2. Growth of TiO_2 nanowires on ceramic templates

TiO_2 nanowires were synthesized by a hydrothermal method in 23mL Teflon-lined autoclaves (Parr Instruments, Moline, IL, USA). TiO_2 templates (5 mm*5 mm) were prepared and fixed on a Teflon holder with the polished side facing down, and the holder placed in the hydrothermal reactor. Titanium (IV) tetrabutoxide (97%, Sigma

Aldrich) was used as the Ti source. 1ml of Milli-Q water was used as solvent and 10ml of Hydrogen Chloride (HCl, 37%, Fisher Sci) was mixed into the solvent. The Ti precursor was added to the acidic solvent, drop by drop, in order to slow the condensation of hydrolyzed Ti precursor (final concentration is [Ti]=0.25M). The final solution precursor mixture was placed into 23-mL Teflon-lined autoclaves containing the template, sealed and placed in convection ovens at 180°C for different time durations (40 minutes to 12 hours). After the reactions were complete, they were subsequently cooled under ambient conditions. The resulting templates were then washed with water to remove any unreacted precursor and reaction by-products. Samples were then dried in air at room temperature.

3.2.2 Material Characterization

The resulting templates were characterized using X-ray diffraction for phase analysis. The crystallographic orientations of the templates were examined by electron backscattered diffraction (EBSD). The elemental composition at surface of the templates was measured by X-ray photoelectron Spectroscopy (XPS). Light absorption of the templates was detected using Ultraviolet-visible spectroscopy (UV-Vis). Structural and morphology analyses of the nanowires growing on the templates were conducted using scanning electron microscopy (SEM) and transmission electron microscopy (TEM).

TiO_2 templates (with or without nanowires growing on the surface) were characterized using X-Ray Diffraction (XRD; PANalytical Empyrean, The Netherlands) using Ni-filtered Cu Kα radiation (λ = 1.5406 Å) at 45kV and 40mA within the 10-70° 2θ range for phase analysis.

High-resolution EBSD mapping of the templates were collected on a Zeiss Ultra Plus field emission gun (FEG) SEM, equipped with an Oxford Instruments Aztec EBSD system. 20kV accelerating voltage and beam current of approximately 1-5 nA was used for the characterization. The electron backscatter diffraction patterns (EBSPs) were indexed using a Rutile structure, with a step size of 2μm on a grid of 600 x 600 points. The analysis speed was approximately 100 indexed patterns per second.

UV-Vis diffuse reflectance spectra of the templates were performed with a CARY 300 UV-Visible Spectrophotometer. The spectral resolution was 1 nm over the spectral region from 200 nm to 800 nm.

X-ray photoelectron spectroscopy (XPS) characterization was carried out by using a Kratos AXIS ULTRADLD XPS system equipped with an Al Kα monochromated X-ray source and a 165-mm mean radius electron energy hemispherical analyzer. The vacuum pressure was kept below 3×10^{-9} torr during the acquisition.

Atomic Force Microscopy (AFM, Dimension 5000 Nanoman AFM, Veeco) was used to study the surface roughness of templates created after the sintering process. The template samples were adhered to an AFM puck using carbon tape and imaged using silicon cantilevers at a frequency of 300 kHz and spring constant of 60 N/m, with scan size varying from 500 nm to 10 μm.

The morphology and size of TiO_2 nanowires were observed with Scanning Electron Microscopy (SEM; Philips FEI XL30, Eindhoven, The Netherlands) at 10kV accelerating voltage. The growing orientation and the diameter of the nanowires were determined using Transmission Electron Microscopy (TEM; CM300, Eindhoven, The

Netherlands) at 300kV accelerating voltage for bright field imaging and electron diffraction analysis.

3.2.3 Photoelectrochemical Performance

The pellet TiO_2 templates with or without nanowires were coated with a layer of gold on the backside, and the specimens were mounted onto copper, which was enclosed in a glass sheath. The contact between the specimen and copper rod was established using silver paste, which was subsequently sealed with epoxy to ensure isolation from the electrolyte during electrochemical testing. The cyclic voltammetry measurements were conducted with Nitrogen gas purged 0.5M H_2SO_4 electrolyte. During each measurement, the potential of the working electrode was set between -0.1 and 1.9 V vs. a Ag/AgCl Electrode at a rate of 100 mV/s using AUTOLAB potentiostat/galvanostat instrument. Photocurrents were measured in the dark and under illumination using a Xenon lamp (Xenonlampenversorgung TYP SVX 1450, Muller).

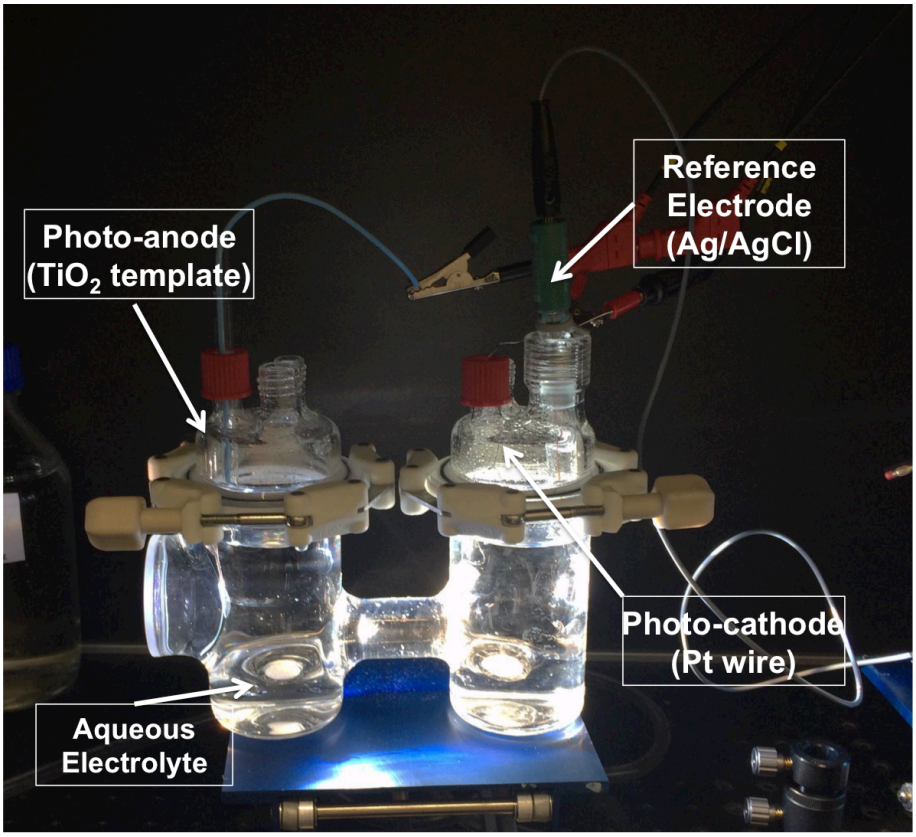

Figure 22. Experimental setup for photoelectrochemical test.

3.3. Results and Discussion

3.3.1 Synthesis of TiO_2 Nanowires on Novel Templates

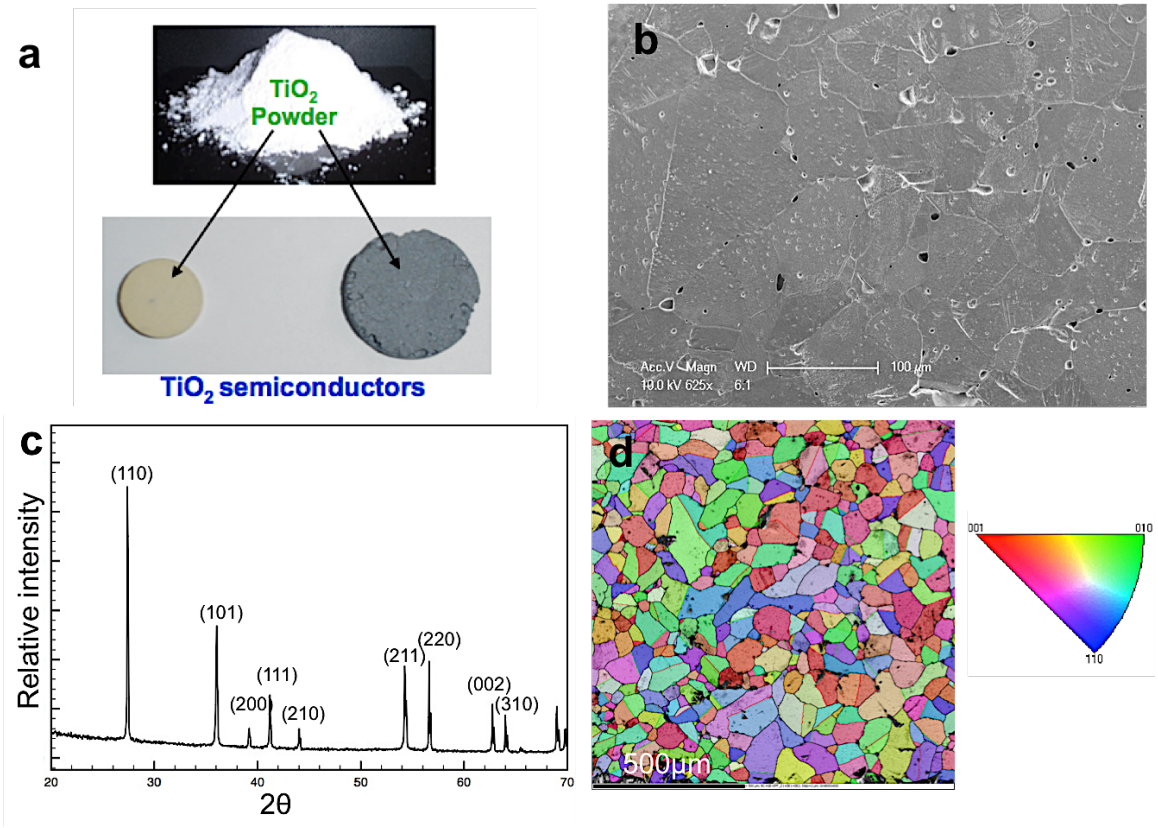

Figure 23. Fabrication and characterization of TiO_2 templates (a) Schematic of fabrication, (b) SEM of surface highlighting grains and distribution, (c) XRD confirming TiO_2 rutile phase and "lack" of impurities, (d) EBSD showing grain orientations on blue template.

The templates were prepared by compressing TiO_2 powder into pellets, followed by sintering the pellets in different gas environments. The chemical property of the template was affected by the gas environment that was chosen for the annealing process. As seen in Figure 23, two kinds of templates were produced by annealing in different gas

environments with controlled oxygen activity. The white color template was produced under an oxidative gas, while the blue template was prepared in a reduced gas. Under normal annealing conditions, TiO_2 has a white color. However, it has been found that TiO_2 can exhibit different colors via different preparation methods or approaches. Blue TiO_2 (as shown in Figure 23a) is due to oxygen deficiencies created by annealing under highly reduced conditions [170, 171]. Figure 23b reveals the surface structure of the templates. Since the white and blue templates have the same structures on the surface, only one representative SEM image is shown here. The sample is composed of large grains that are ~ 20μm to 200μm. The size of the grains on the template can be controlled by different sintering times in the furnace with controlled grain boundary diffusion [172]. X-ray diffraction in Figure 23c indicates polycrystalline rutile TiO_2 without any impurities. This is clearly seen in the EBSD map in Figure 23d, where different colors represent the orientations of individual grains. Non-indexed points, which are black, are seen to occur at some points on the grain boundaries.

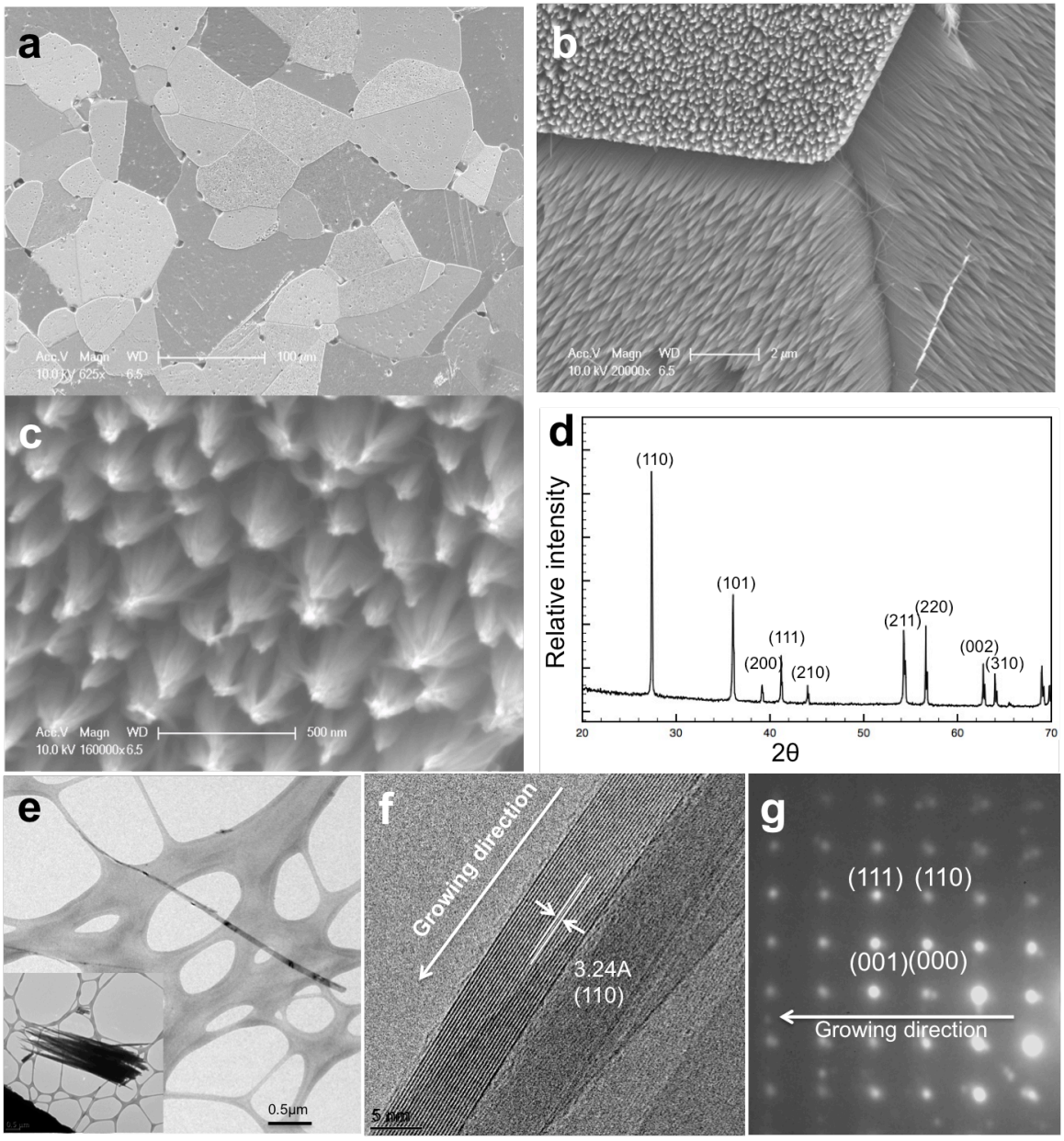

Figure 24. SEM micrographs, XRD and TEM micrographs of TiO_2 nanowires synthesized on the blue template at 180 °C under reaction conditions for 6 hours. (a, b) Low magnification SEM micrographs indicate the distribution of wire orientations and density of wires, (c) high magnification SEM micrograph highlight the tips of the wires, (d) XRD pattern of the TiO_2 nanowires growth on the template, (e, f, g) TEM micrograph, HRTEM and SAED of TiO_2 nanowire, showing aspect ratio, morphology, phase and orientation.

Highly controlled TiO_2 nanowires (TNWs) on the TiO_2 templating system were produced by using hydrothermal method. The phase, morphology and structure of the TiO_2 nanowires thin film are characterized by X-ray diffraction (XRD), scanning electron microscopy (SEM) and transmission electron microscopy (TEM). High density and uniformly distributed TiO_2 nanowires have been successfully produced on the templates, and the growth orientation of the nanowires were finely controlled by growing on different grains of the template, which is shown in Figure 24a (the different brightness indicate different exposed planes of the TiO_2 nanowires). Figure 24b highlights an area that is composed of three different grains, and the TiO_2 wires are growing in different directions on each grain. High resolution SEM, Figure 24c, shows the tips of the nanowires, each bundle is composed of many thin nanowires, which are approximately 15-30 nm in diameter. The thin nanowires are aggregated together due to the surface tension during the drying process [173]. XRD (Figure 24d) confirms that the nanowires are pure rutile TiO_2 without any impurity phases. A TEM micrograph (Figure 24e) of one single nanowire with the inset TEM image showing a bundle of nanowires. It demonstrates that the bundle consists of several thin nanowires, each of which is 3-5 μm in length 20 nm in diameter. The nanowires are observed to be very thin at the tip (10-15 nm) and get thicker (50 nm in the middle) from tip to bottom. The nanowires appear fused together (forming one single crystal wire) at the base. This is likely due to lateral growth of wires at lower supersaturation values (after the initial burst of nuclei). The average aspect ratio of the wire is calculated to be around 100. HRTEM (Figure 24f) highlights one nanowire in the bundle, revealing its single-crystalline nature and the

diameter of a single nanowire is about 8 nm SAED of the wire (Figure 24f) indicates that each nanowire is a single crystal and the wire is growing along (001) direction, which is the fastest growth direction of rutile TiO_2 [168].

The reaction is conducted in a solution with a high HCl concentration (10 mol/L), which significantly affects the solution conditions. The high concentration of HCl provides a low pH (-1.9) environment, which increases the solubility of TiO_2 by enabling the complexation with Cl^- ions, which compete with OH^- ions in the octahedral coordination sphere with Ti^{4+}. This leads to potential dissolution-recrystallization reactions that can fuse nanowires together. At this low pH, the concentration of OH^- ions complexed with Ti ions is reduced which leads to a decrease in the rate of condensation reactions. In addition, at the reaction condition of pH=-1.9, the solubility of Ti precursor is high, which favors Ostwald ripening, crystal growth will form ion by ion and follow the favorable growth directions [104, 174, 175]. Because of the higher surface energies of the (001) planes (vs. the lateral (110) plane) [176], the growth velocity along the [001] direction is faster than the sides of the (110) surface, leading the rutile nanowire formation [168, 169]. TiO_2 nanowires growing on the templates perform an epitaxial effect on different grains[177]. Each grain has a specific crystalline direction, and the TiO_2 nanowires will follow the directions of each grain.

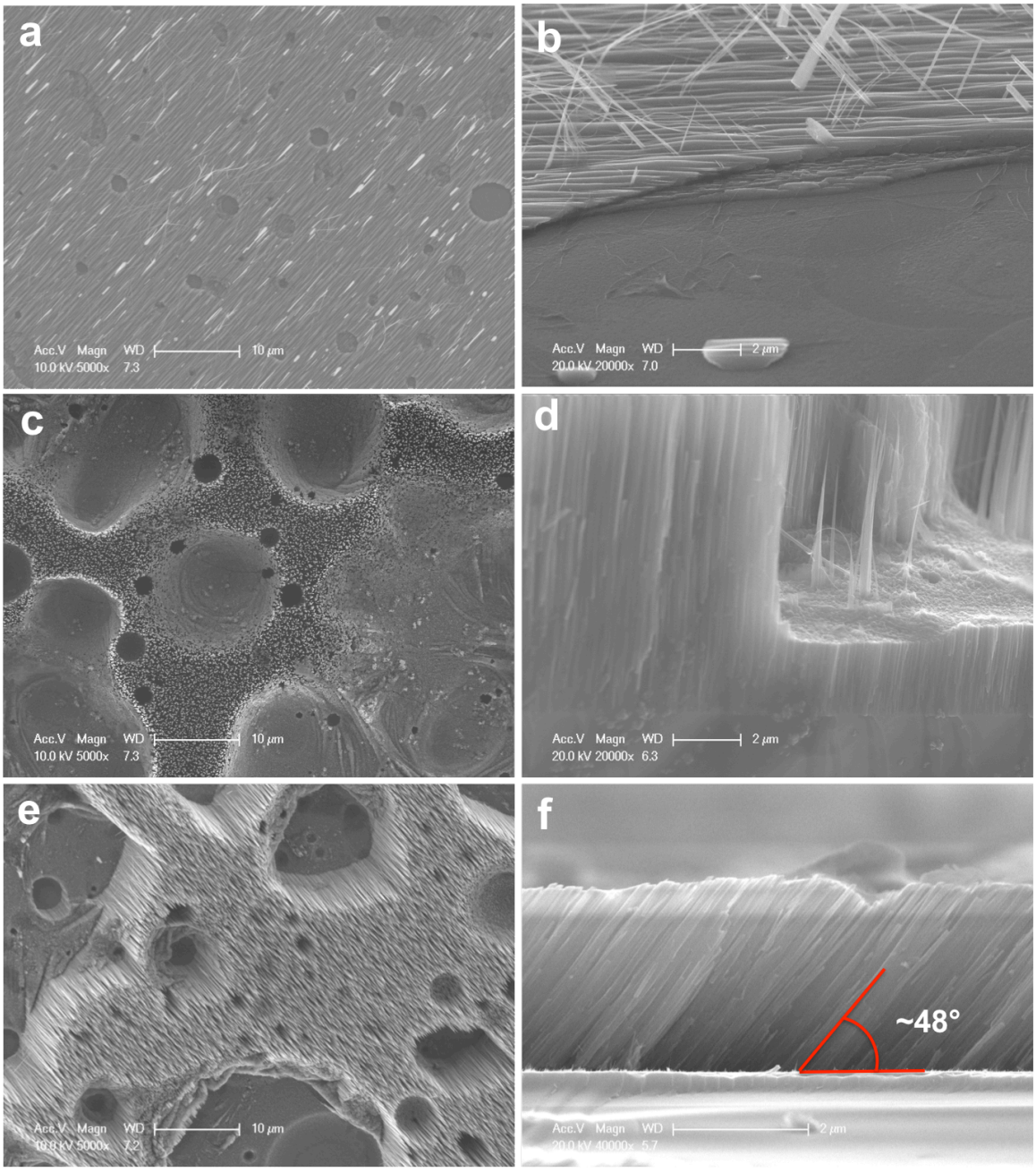

Figure 25. Scanning electron micrographs of TiO_2 nanowires epitaxial growth on TiO2 single crystal wafers for the top and cross-section views (a, b) (100), (c, d) (001), (e, f) (111).

To further investigate the growth behavior of the nanowires on different grains, TiO_2 nanowires have been grown on single crystalline TiO_2 wafers (001) (100) (111). It is observed in Figure 25 that TiO_2 nanowires grow horizontally on (100) wafer, vertically on (001) wafer, and align at some angle with the (111) wafer. The nanowires are all growing in (001) orientation, which is the fastest growing direction of rutile nanowires, as shown before. However, the nanowires grow on different single crystalline wafers with the same orientation as the underlying single crystal templates. The nanowires on (100) wafers maintain the same orientation as the underlying template. The angle between the wires and the (111) single crystalline wafer were measured to be approximately 48°, which corresponds to the angle between the (111) and (001) planes. This confirms the nanowires are oriented with the underlying template and are growing fastest along the (001) direction. These observations confirm the homo-epitaxial growth phenomenon, which has been proved to be a promising approach to obtain aligned nanostructures due to good lattice match and no impurity [178]. The driving force for homo-epitaxial growth is surface energy and surface structures [179], which leads to continuous growth of crystalline structures in the same orientations as the templates.

3.3.2 TiO_2 nanowires synthesis with controlled length, diameter, and tip sharpness.

3.3.2.1 Control of the nanowire length via reaction time

The length of the TiO_2 nanowires can be controlled by reaction time, and the kinetic growth study of the nanowires on templates has been conducted (as seen in Figure 26). Figure 26a and b depict the bare template surface before nanowire growth. It is

observed that the surface is not smooth but rather has some edges, steps and terraces on the surface, which might be introduced by crystal reconstruction in the annealing process [180]. XRD analysis of samples produced for different time durations in Figure 26c shows that the nanowires on the templates as well as the bare templates are in the form of rutile TiO_2. SEM micrographs in Figures #d – o reveal the TiO_2 nanostructures produced for different reaction times from 1 hour to 12 hours, respectively. From the SEM analysis, we observe significant crystal growth along the length of the wires with increasing reaction time. The nanowires length increase in length from ~ 100 nm at 1 hour to ~18 μm at 12 hour. The nanowire diameters also increase with time from ~10 nm to 200 nm, but at a slower rate than the length. The aspect ratios of the nanowires are relatively constant until 6 hours, after which it increases dramatically at 12 hours. Details of the length, diameter and aspect ratios of the nanowires growing from 1 hour to 12 hours on both white and blue templates are shown in Table 2. The diameters of the nanowires are relatively constant from 6 hours to 12 hours, which is likely due to limited diffusion of precursor. This is because the nanowires are closely packed on the surface, there is limited space between adjacent nanowires for the precursor molecules to penetrate. Since the precursor is in contact with the tip of the wires continuous growth along the (001) direction. Nanowires growing on blue templates have much smaller diameters and larger aspect ratios than ones of the white templates, and is discussed in detail in the following sections.

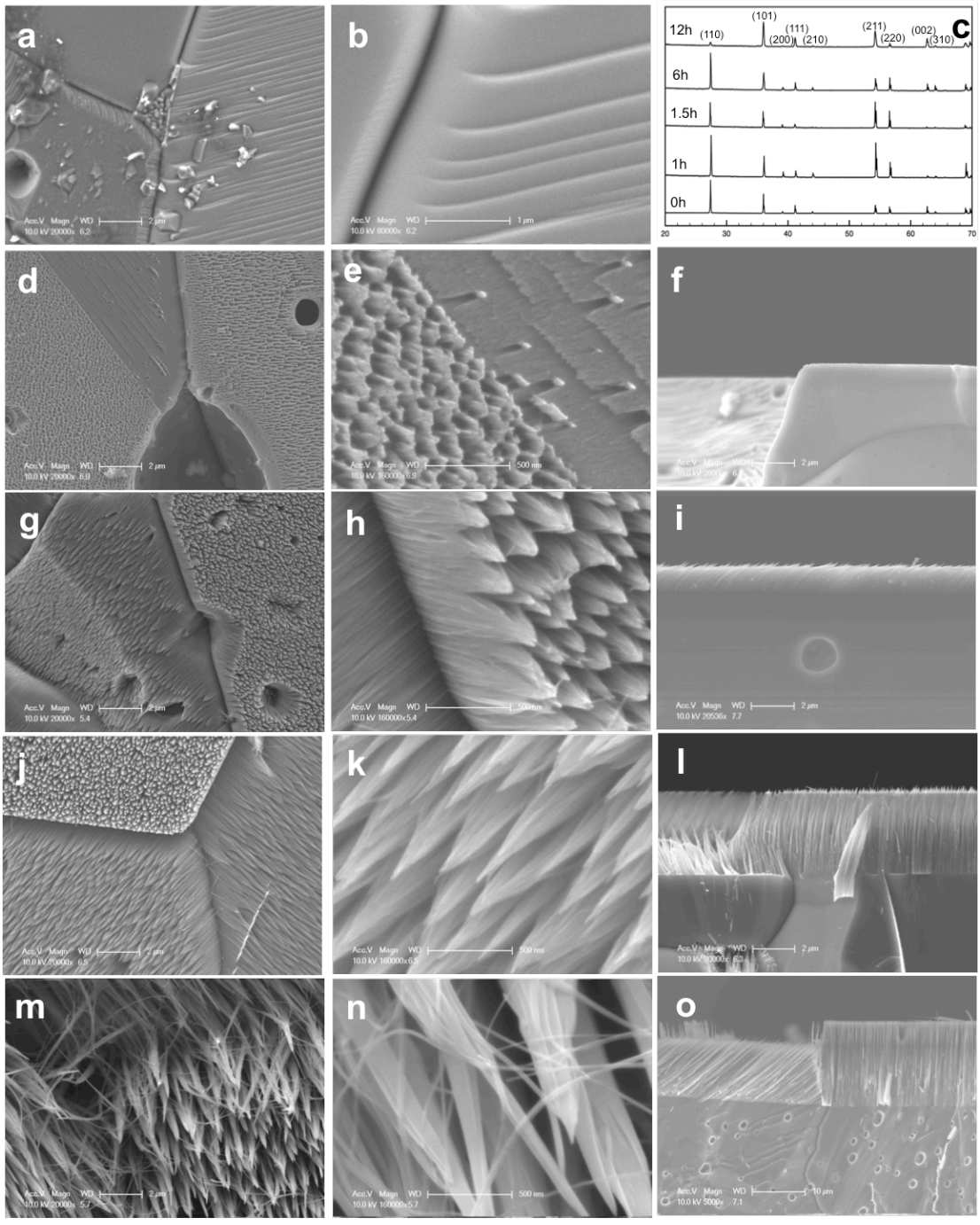

Figure 26. Kinetic study of the growth of TiO_2 nanowires on white templates. SEM micrographs (a-b, d-o) and XRD patterns (c) of TiO_2 nanowires growth on template at different reaction times on the surface (left column), high magnification SEM (middle column) and cross section SEM micrographs (right column) : (a, b) 0 hr template without TiO_2 nanowires, (d, e, f) 1 hr, (g, h, i) 1.5 hr, (j, k, l) 6 hr, (m, n, o) 12 hr.

Table 2. Summary of the diameter, length and aspect ratio of TiO_2 nanowires growing on different templated surfaces.

Reaction time	White			Blue		
	width	height	Aspect ratio	width	height	Aspect ratio
1h	N.A.	100nm	N.A.	N.A.	100nm	N.A.
1.5h	12-30nm	1.5µm	75	6-15	1.5µm.	150
6h	15-200nm	5µm	50	15-40nm	5µm	150
12h	15-200nm	18µm	180	15-60nm	18µm	450

In order to get a more detailed view of the nanowire growth process, we focused on the early stages of the growth. SEM micrographs (Figure 27a, b) reveals the nucleation process for the TiO_2 nanowires on the templates. It is observed that the nuclei initially formed at the defect sites (i.e., kinks). These high-energy sites enable precursor molecules to attach more readily compared to terraces or to flat step edges [130, 180, 181]. The rate at which molecules can nucleate on a crystal, for a given solute concentration, scales with the kink density. This provides a hint that the growth rates of crystals can be altered by roughness of the sample.

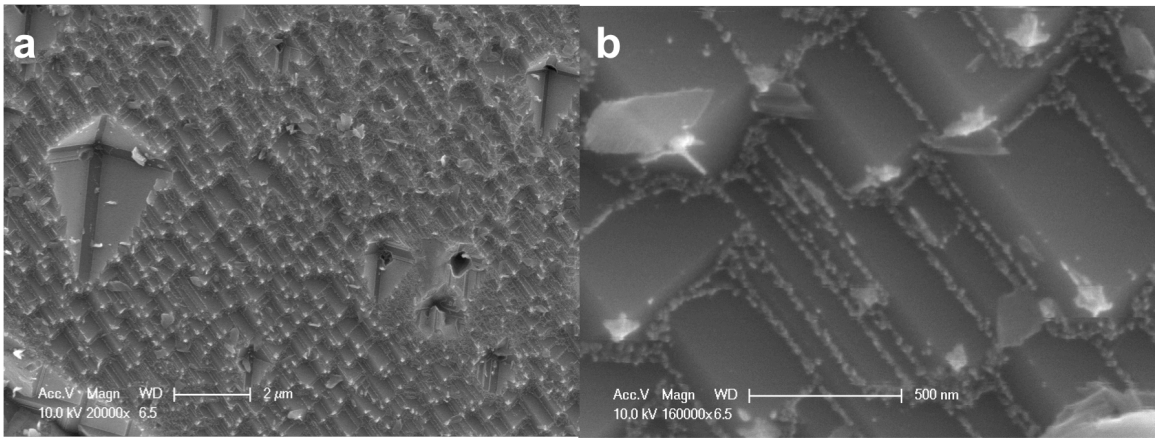

Figure 27. The growth of TiO_2 nanowires on templates at 50 minutes (a) low magnification and (b) at high magnification SEM micrographs.

3.3.2.2 Control of the nanowire diameter by surface chemistry

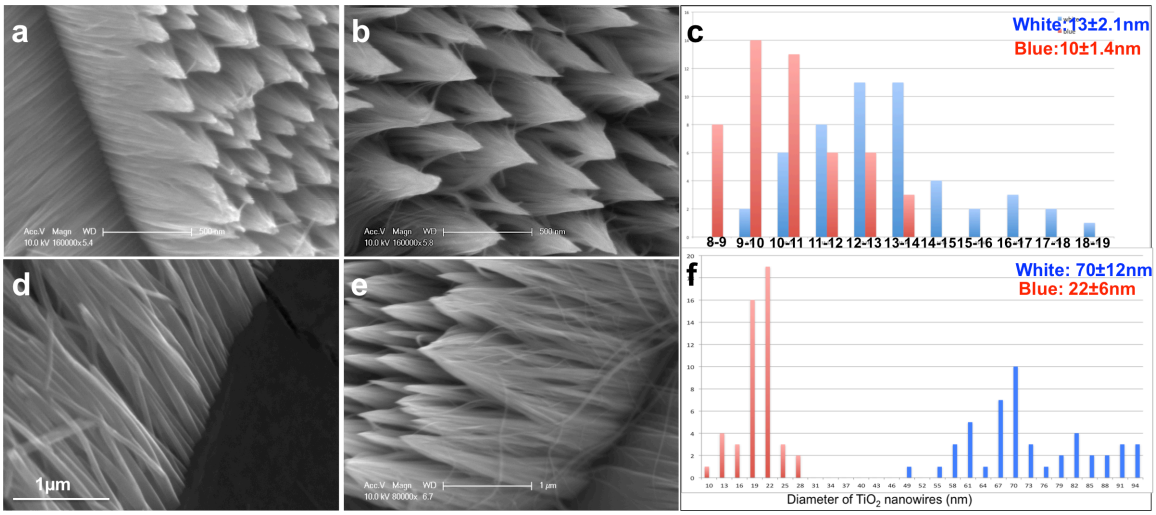

Figure 28. SEM micrographs and size distribution of the TiO_2 nanowires produced on white and blue templates for 1.5 hour and 6 hours. (a) white 1.5 hour, (b) blue 1.5 hour, (c) size distribution of white and blue for 1.5 hour, (d) white 6 hours, (e) blue 6 hours, (f) size distribution of white and blue for 6 hours.

The diameter and the density of the TiO_2 nanowires on the templates have been studied. By controlling the parameters when preparing the TiO_2 templates, two templates with different surface properties have been developed: white templates were treated in oxidative gases while blue templates were treated with reductive gases that may induce more oxygen vacancies [182]. SEM micrographs (Figure 28c, d) clearly demonstrate that the nanowires on both templates have similar morphologies. However, the diameters of the nanowires are different for the two templates. At 1.5 hours, the diameters of the nanowires on white templates are approximately 13±2.1 nm, while the nanowire diameters of the blue templates are 10±1.4 nm. After 6 hours reaction duration, the diameter of the nanowires on white and blue templates increased to 70±12 nm and 22±6

nm, respectively. Continuous crystalline growth in both vertical and lateral directions is common, albeit at different rates. The size increase of the nanowire diameter growing on the white templates is significantly different than on the blue templates. The difference of the nanowire diameter on white and blue templates is due to different surface chemistry properties, which is introduced by annealing the template under different gas environments.

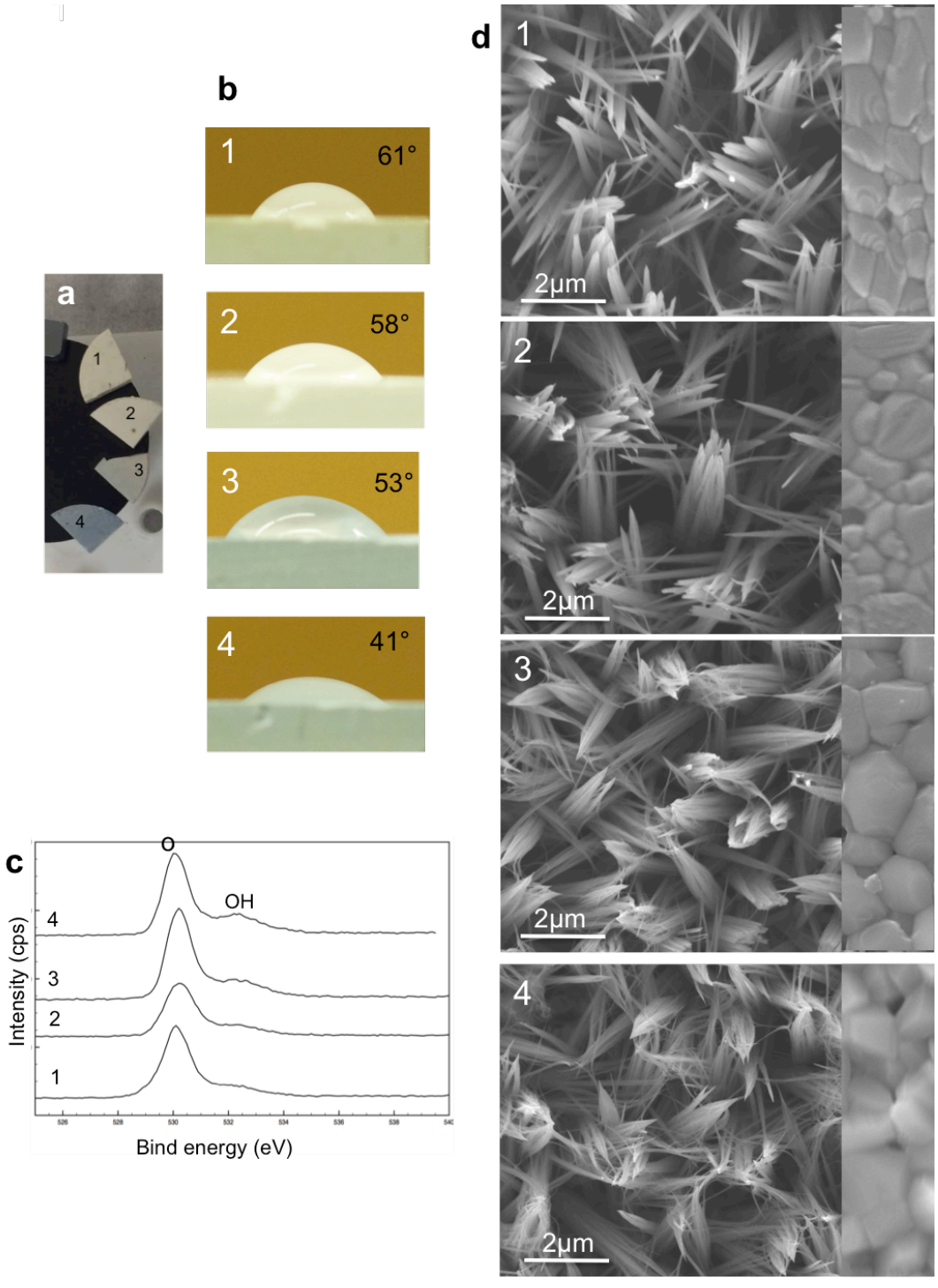

Figure 29. Characterization of the properties of 4 different wafers, and investigation of the nanowire growth on the templates. (a) photographic image, (b) contact angle analyses, (c) XPS, (d) TiO_2 nanowires growth on 4 different wafers (the insets in d are SEM micrographs of the templates before nanowire growth).

To further study the effects of the surface chemistry on the nanowire size, more thorough work has been conducted. Four templates (1-4) were annealed under different environments with controlled oxidative/reductive gases, from strongly oxidized [$p(O_2)$ = 75 kPa], oxidized[$p(O_2)$=10 Pa], reduced[$p(O_2)=10^{-5}$ Pa], to strongly reduced [$p(O_2) = 10^{-10}$ Pa]. As seen in Figure 29a, the color of the templates change from white to light blue and then to dark blue, which indicates the change in surface chemistry / defects. Wettability is an inherent characteristic of a solid surface. It effects the interactions between the template surface and the surrounding precursor solutions. To investigate the dependence of the wetting behavior on the resulting nanowire structure, the wettability is evaluated by placing a water droplet on the template surface. Figure 29b shows the contact angles of templates 1-4 are approximately 61°, 58°, 53°, 41°, respectively. The contact angles are usually affected by surface structure or surface energy [183]. In this work, structural surface features (i.e., kinks, edges, terraces) of the 4 templates are similar to each other, as seen the insets in Figure 29d. Thus, the surface energy will be dominant in affecting the nucleating properties of the templates. Surface energy can affect the nucleation processes of the nanowires. The continuous decrease in the contact angle from templates 1 to 4 indicates the increased availability of precursor in contact with the template surface, which will lead to a high nucleation density. Therefore, smaller diameter nanowires will be formed, which is confirmed in the SEM micrographs in Figure 29d.

The surface energy differences of these 4 templates are introduced by different annealing conditions. The reduced gas will lead to the formation of oxygen deficiencies

and Ti^{3+} near the surface (i.e., increase oxygen deficiency from templates 1 to 4). The stoichiometry near the surface would thus change from TiO_2 to $(TiO_{2-z})_nX_m$ (X can be any weakly absorbed species such as OH, H_2O, organic impurities). The species would occupy the vacant spot to coordinate with the Ti atoms at the surface to realize the sixth coordination [184]. Oxygen deficiency manifests itself in the formation of either oxygen vacancies or titanium interstitials [170], and it is investigated with X-ray photoelectron spectroscopy (XPS). Figure 29c shows the O 1s XPS spectra of these 4 samples, and it shows a trend of increasing peak intensity at around 532.1 eV, which is assigned to Ti-OH group formation, such as water molecules absorbed on the vacancies of TiO_2 [171, 185-188]. The single O 1*s* peak at 530.0 eV is a typical peak from oxygen in TiO_2. The Ti 2p XPS spectra of the 4 samples are almost identical, indicating the Ti atoms have similar bonding environments after sintering treatments. The lack of change of the Ti 2p band is due to healing of the Ti^{3+} defects by adsorption species (e.g., oxygen and water) [187, 189].

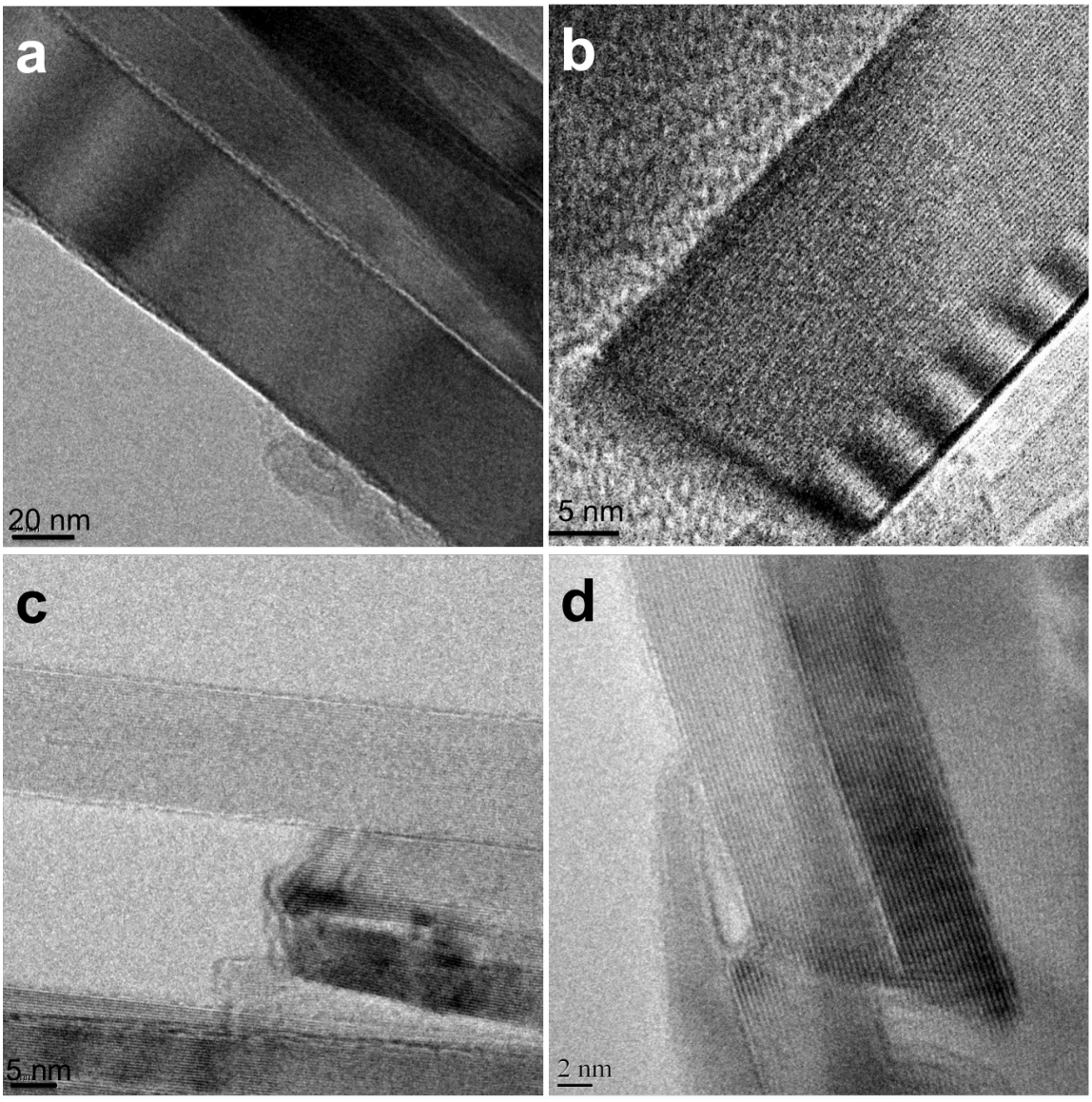

Figure 30. TEM micrographs of the nanowires growing on (a) template 1, (b) template 2, (c) template 3, (d) template 4, which were produced via an annealing process under different gas environments.

High resolution TEM was conducted on the nanowires growing on the 4 templates to further confirm the diameter of the nanowires. It can be observed that each nanowire is a single crystal with growing direction along the [001]. The diameters of the nanowires

were measured to be approximately 40 nm, 20 nm, 12 nm and 6 nm for samples 1 to 4, respectively. It is obvious that with an increase in surface oxygen deficiencies, TiO_2 nanowires with decreasing diameters are produced. Therefore, it can be concluded that the oxygen deficiencies produced during the annealing process will affect the surface energy, which can be used for controlling the size of the nanowires array growing on the templates. The density and size of the TiO_2 nanowires produced mainly depend on the nucleation rate on these four templates. According to the classical nucleation theory, the nucleation rate is indicated as the equation below.

$$J_s = A\ exp\frac{-B\gamma^3}{\Delta\mu^2}$$

Where A is a constant relative to the concentration of the precursor ions, and B is a constant depending on the molecular vibration and aggregation. γ is the specific surface energy, and μ is the supersaturation [190] [130, 191]. In our system, all four reactions have the same reaction conditions. Therefore, the specific surface energy becomes the central parameter for the nucleation kinetics. The surface energy, which can be translated into oxygen deficiency in our case, scales to the 3rd power, Therefore, the changing of the surface energy on these four templates can affect the nucleation rate, diameter and density of the nanowires significantly.

3.3.2.3 Control of the nanowire diameter by surface roughness

It has been discussed in a previous section that the roughness could control the growth rate of the crystal nanostructures, therefore affecting the density and the size of

the nanowires on the templates. To investigate the roughness effects on the nucleation and growth process, other potential factors, such as surface chemistry, have to be excluded. Therefore, the roughness study was conducted on single crystalline TiO_2 wafers, which have nearly uniform roughness and chemistry. Secondary ion mass spectrometry (SIMS) was applied to create a series of craters, and the roughness created on different crystallographic surfaces, such as (100), (001) and (111). Subsequent hydrothermal growth of titanium dioxide nanowires arrays on the craters was conducted to investigate the roughness effects on the nucleation process of TiO_2 nanowires.

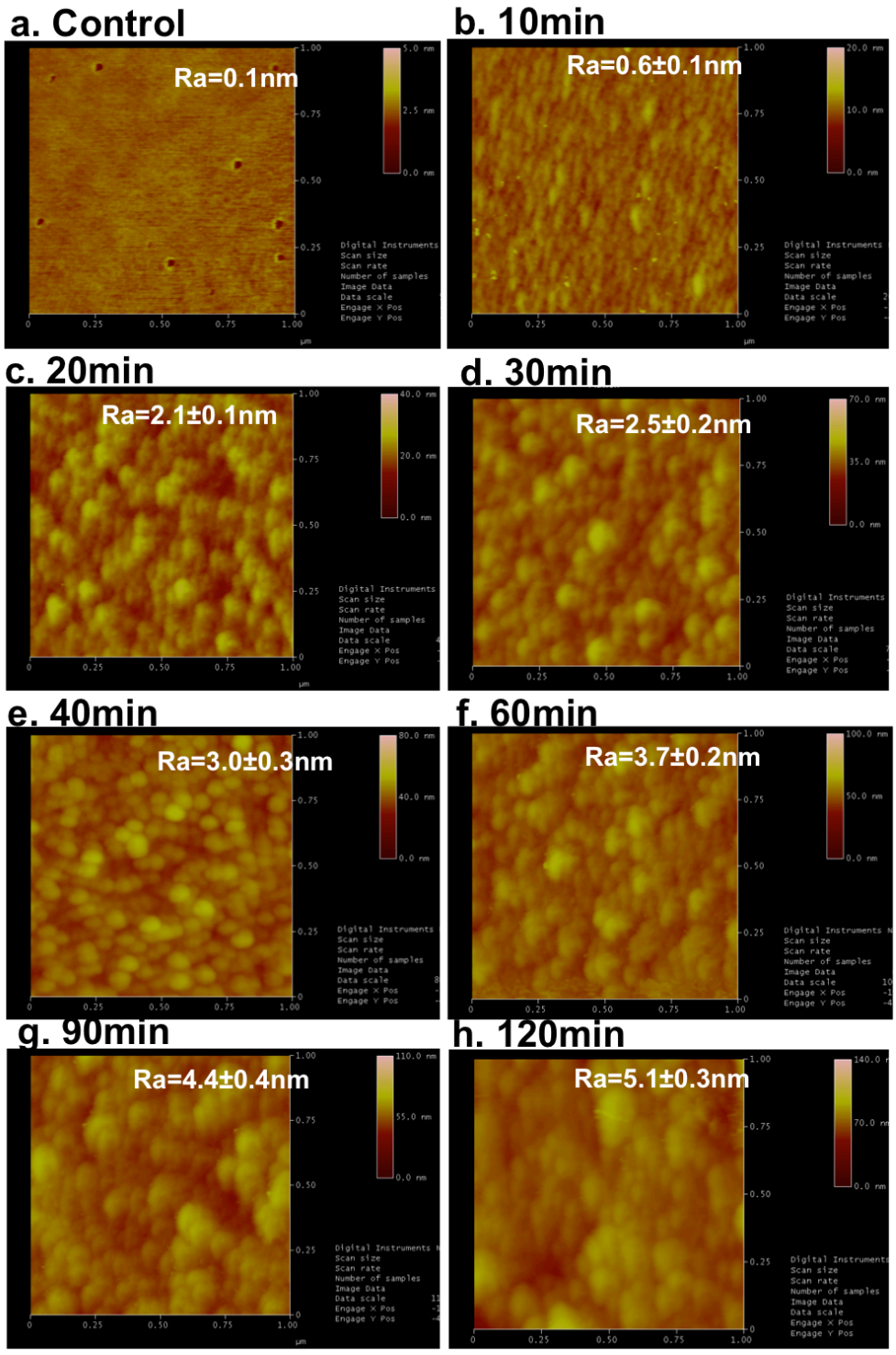

Figure 31. AFM images for SIMS induced craters on (100) TiO_2 single crystal templates with different roughness' for (a) 0 minutes, (b) 10 minutes, (c) 20 minutes, (d) 30 minutes, (e) 40 minutes, (f) 60 minutes, (g) 90 minutes, (h) 120 minutes.

To study the roughness created using SIMS on single crystalline wafers, AFM is used for evaluating the average roughness (R_a) analysis on each crater, as seen in Figure 31. The templates without SIMS treatment are very smooth, with a roughness of 0.1 nm. After SIMS treatment on the surface to create craters, it is obvious from the AFM analysis that the average roughness increases with increasing SIMS time. It increases from R_a=0.6 nm at 10 minutes SIMS treatment to R_a=2.5 at 30 minutes, and finally to R_a=5.2 nm at 120 minutes. SIMS treatments were also applied to (001) and (111) single crystalline TiO_2 templates as well as on silicon wafers to create craters with different roughness'. The roughness data vs. SIMS time for different templates is summarized in Figure 32. The roughness of the silicon wafer changed significantly at the early ages of the SIMS treatment, increasing from 0.1 nm to 2.0 nm within the first 20 minutes, but it reaches some equilibrium status without increasing roughness with further SIMS treatment. The (100) TiO_2 template is the most sensitive orientation to SIMS compared with the (001) and (111) single crystalline wafers.

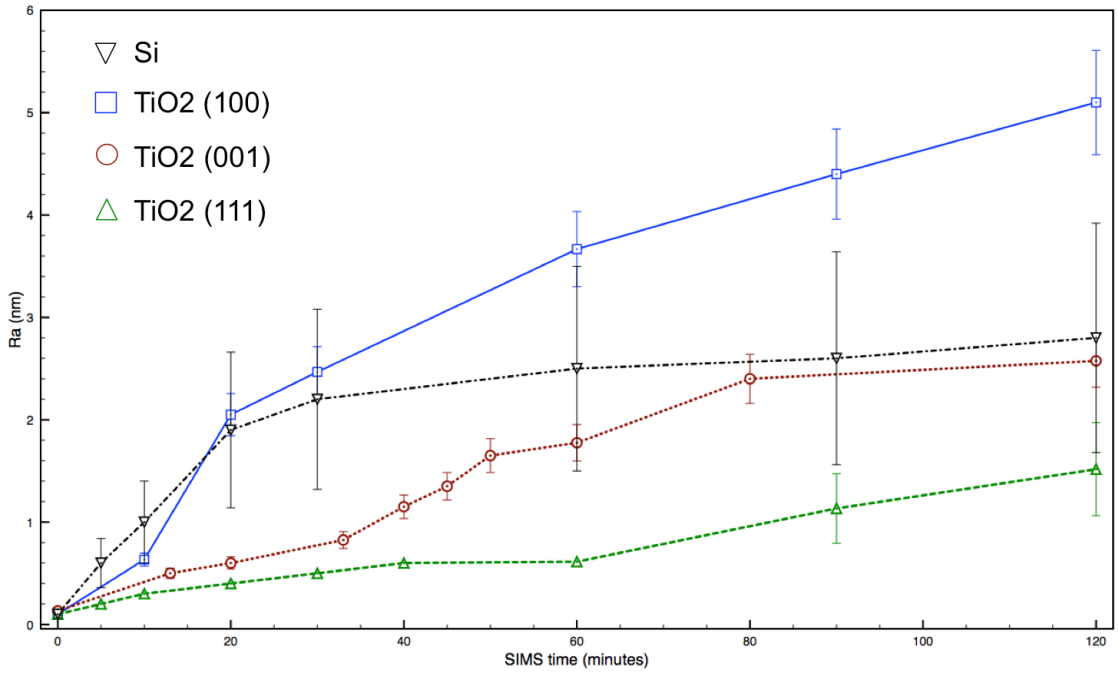

Figure 32. Roughness vs. SIMS treatment times for silicon (100) and TiO_2 single crystalline wafers in (100), (001) and (111) orientations.

It has been confirmed that SIMS can be used for controlling the roughness of the TiO_2 templates by applying for different time durations, and the effects of roughness on the nanowire growth would be conducted through hydrothermal reactions, using single crystalline (100) wafer as an example. Since single crystalline wafers are used for this study, there is no surface chemistry difference for different craters. Therefore the surface properties are solely dependent on the structure of the substrate surface, which is represented by the surface roughness. It has been discussed before that surface roughness is related to the number of kinks, steps and terraces. There are more kink sites and edges on a high roughness surface than on low roughness surfaces, and these sites are more favorable for the heterogeneous nucleation of the TiO_2 nanowires to occur due to low

energy barrier (low change in Gibbs free energy) [192], which explains the observations in Figure 33 that shows a high density of nuclei are obtained on templates with higher roughness. Figure 33 and Table 3 shows the comparison between representative samples produced at the craters with different surface roughness', and it presents a significant increase in nuclei number with roughness.

This phenomenon explained an approach for precisely controlling the density and diameter of nanowires by surface roughness using SIMS. SIMS is well known used for elements, composition characterization, this work opens a door for introducing SIMS to the application of nanostructure fabrication.

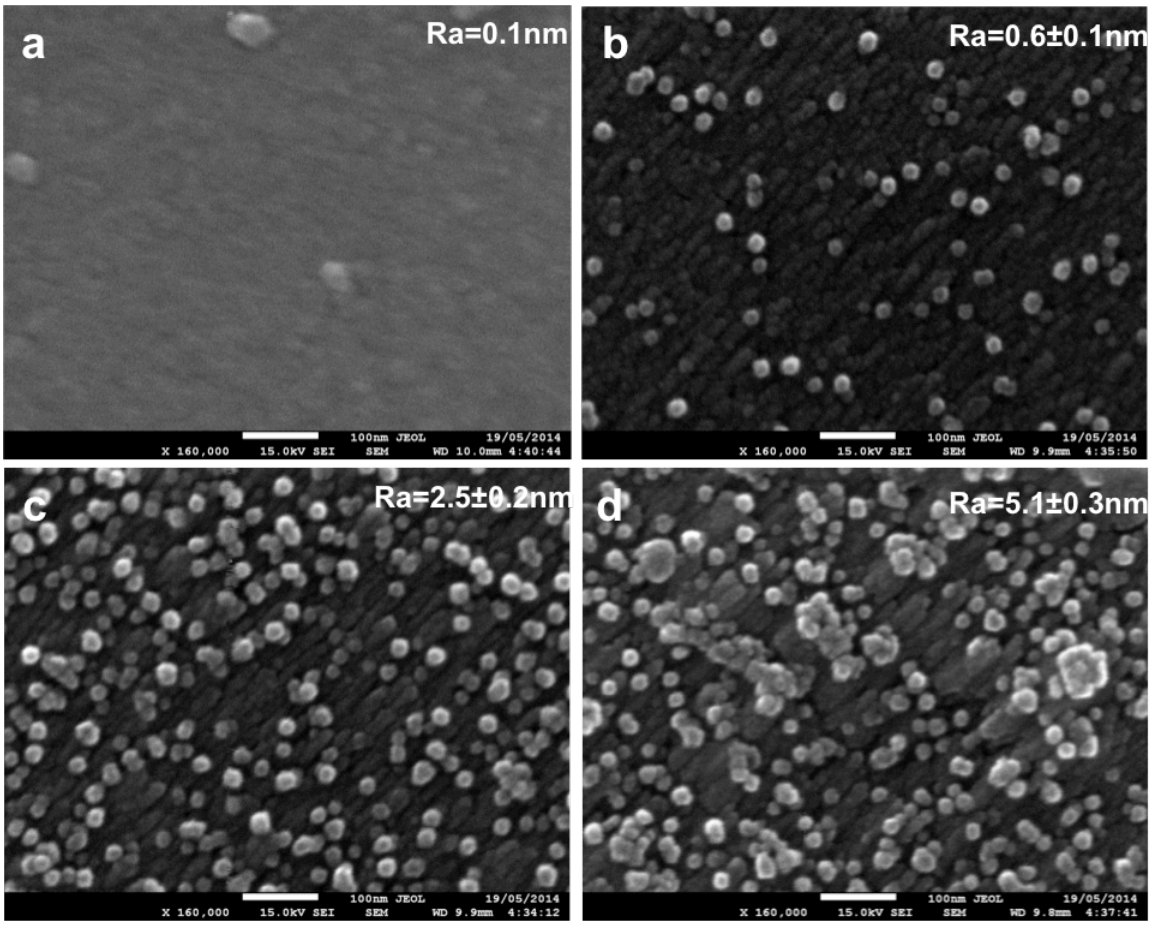

Figure 33. TiO_2 nucleation process on craters with different roughness created by SIMS. TiO_2 (100) single crystal wafer is used, [Ti]=0.25M, HCl=10mL, H_2O=1mL, T=180°C, reaction time = 40 minutes. Nuclei on TiO_2 with roughness of (a) R_a=0.1 nm, (b) R_a=0.6 nm, (c) R_a=2.5 nm, (d) R_a=5.1 nm.

Table 3. List of nuclei number and particle size of TiO_2 produced on craters (TiO_2 (100) single crystalline wafer) with different roughness.

Time	Average Roughness (nm)	Particle size (nm)	#/500*500 nm^2
0 (ctrl)	0.1	N.A.	1
10min	0.6±0.1	40	64
20min	2.1±0.1	27	146
30min	2.5±0.2	35	211
60min	3.7±0.2	39	223
90min	4.4±0.4	50	266
120min	5.1±0.3	62	234

3.3.2.4 Control of the nanowire tip sharpness though diffusion limited reactions

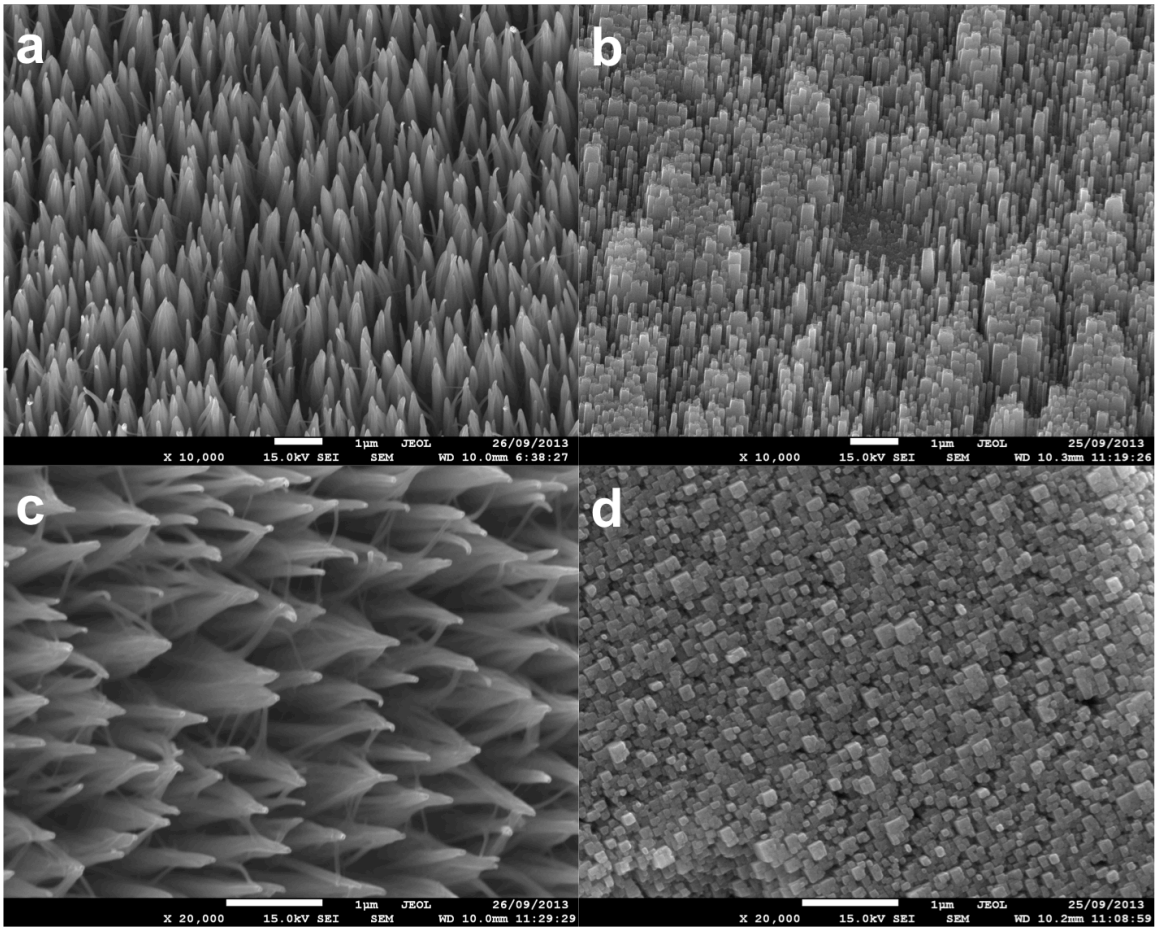

Figure 34. TiO_2 nanowires with sharp tips (a) produced with water as the solvent, with flat tips (b) produced with mineral oil as the solvent.

As illustrated earlier, the TiO_2 nanowires grow in an ion by ion fashion, and the growth process of the nanowire can be controlled via tuning the reaction conditions. When the precursor concentration is high, the nanowires prefer to grow along the [001] direction, which is the fastest growing direction of rutile phase TiO_2 [168, 169]. By controlling the diffusion rate of precursor ions, the sharpness of the tips can be modified, as seen in Figure 34. TiO_2 nanowires with sharp and flat tips can be produced. The

lengths of the wires are similar, with the tips presenting significantly different structures. The TiO_2 templates provide nucleation sites for the growth of the nanowires. At early stages, the precursor concentrations are high, leading to high nucleation rates and the formation of smaller diameter wires. In the solution with water as solvent, the precursor ions can diffuse freely in the solution. There is enough nutrient around the nanowires, but the precursor ions are difficult to penetrate between the densely packed nanowires. Therefore, the nanowires grow fastest along the highest surface energy planes (001), while the growth in lateral directions is limited, which leads to the formation of wires with sharp tips (Figure 34a). However, the use of a viscous solvent such as mineral oil, in which the diffusion of the precursor ions is limited, nanowires with flat tips and thicker diameters (Figure 3b) are formed. Since the diffusion of free precursor ions are hindered in the viscous solvent, there would be enough time for the ions to penetrate in between the wires, enabling growth of the side (110) planes of the nanowires, leading to flat tip and thicker diameter wires.

3.3.2 Photocatalytic Water Splitting Performance Testing

Figure 35 shows UV-Vis Diffusive reflectance and absorbance spectroscopy of white and blue templates. The calculated band gap of the white TiO_2 template is approximately 3.0 eV. Compared with the white template, the blue template possesses significant absorption in the visible and near infrared regions, which indicates the narrowing of the energy gap between conduction band and valence band [193]. It has been reported that oxygen vacancies in rutile TiO_2 can form a mid-gap state between the

original conduction and valence bands. The visible and near-infrared absorptions are assigned to the transitions from the TiO_2 valence band to oxygen vacancy level, or from the oxygen vacancy levels to the TiO_2 conduction band [171, 182, 193, 194].

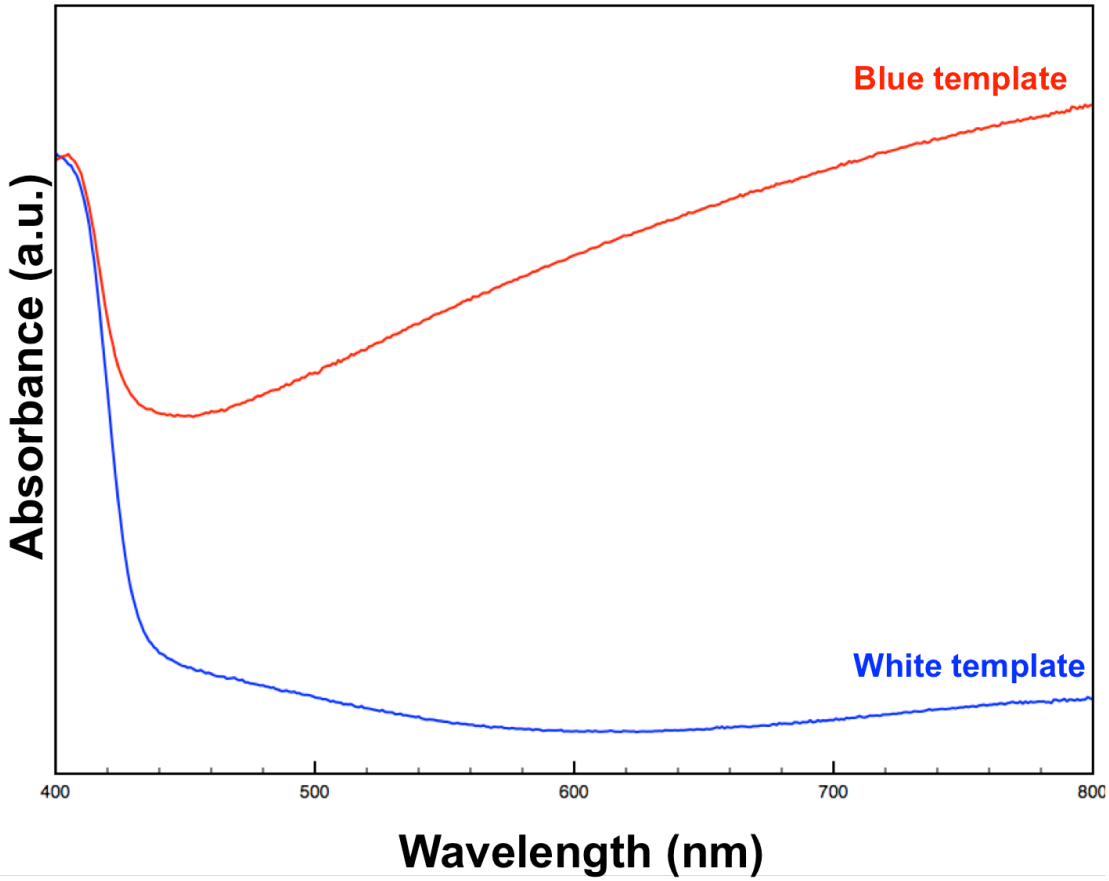

Figure 35. UV-Vis diffusive reflectance and absorbance spectra of the TiO_2 white template and the blue template.

The templates were fabricated into electrodes and a photoelectrochemical cell was assembled. When there is light shining on the photoelectrode, there are O_2 bubbles formed on the light-illuminated photo-anode (TiO_2 template). The production of H_2 gas was confirmed by the formation of bubbles evolving off the photocathode (Pt wires)

immediately after illumination. The number of the bubbles is affected by the illumination light intensity. With high intensity light, there are more bubbles forming on both electrodes.

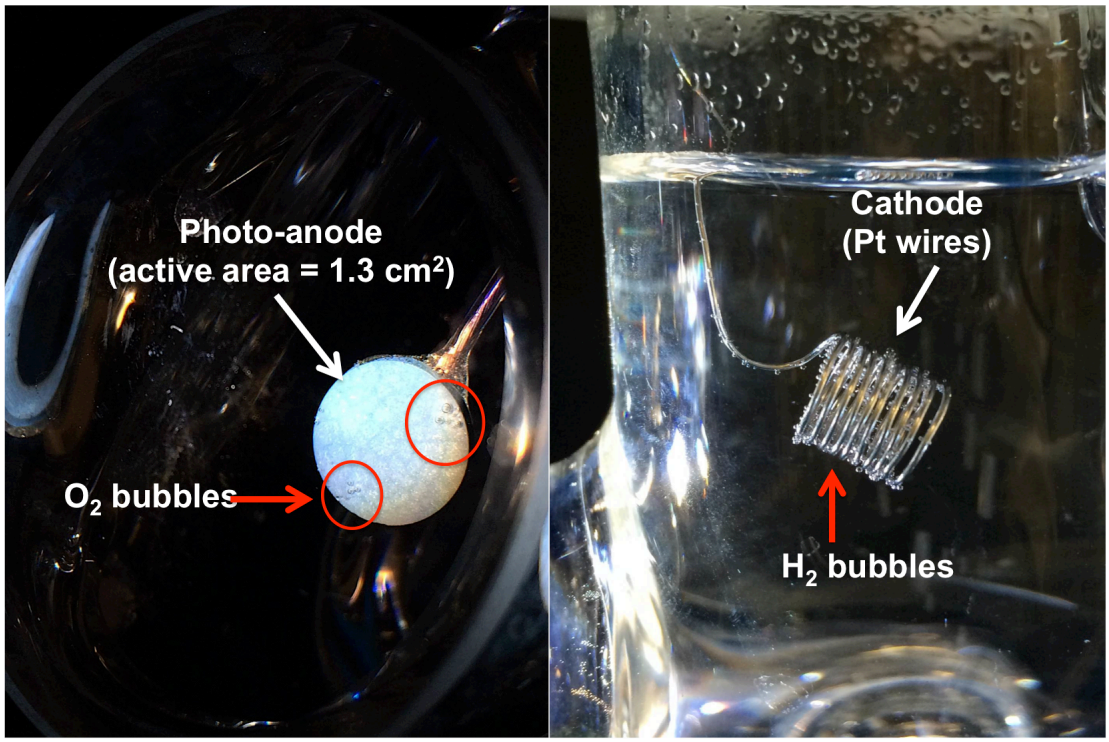

Figure 36. O_2 and H_2 bubbles evolving from the illuminated photoanode TiO_2 template and counter electrode surfaces with light illumination.

Cyclic voltammetry was conducted on both white and blue templates in the dark and in the light with an illumination intensity of 100mW/cm^2, as seen in Figure 37. It is observed that both white and blue templates have photo-responses with the light illumination. The photo-current density of the white template does not show a significant improvement with the illumination (Figure 37a), which might be due to the low

conductivity and high recombination of charge carriers in the bulk TiO_2 sample. Conversely, the blue template has a photo-current density more than 2 orders higher than the white template (Figure 37b). The reason for the remarkable performance is associated with the oxygen deficiencies, which greatly facilitates the charge separation [188, 195]. Since the white template does not show a promising performance, further studies will be focused on the blue template.

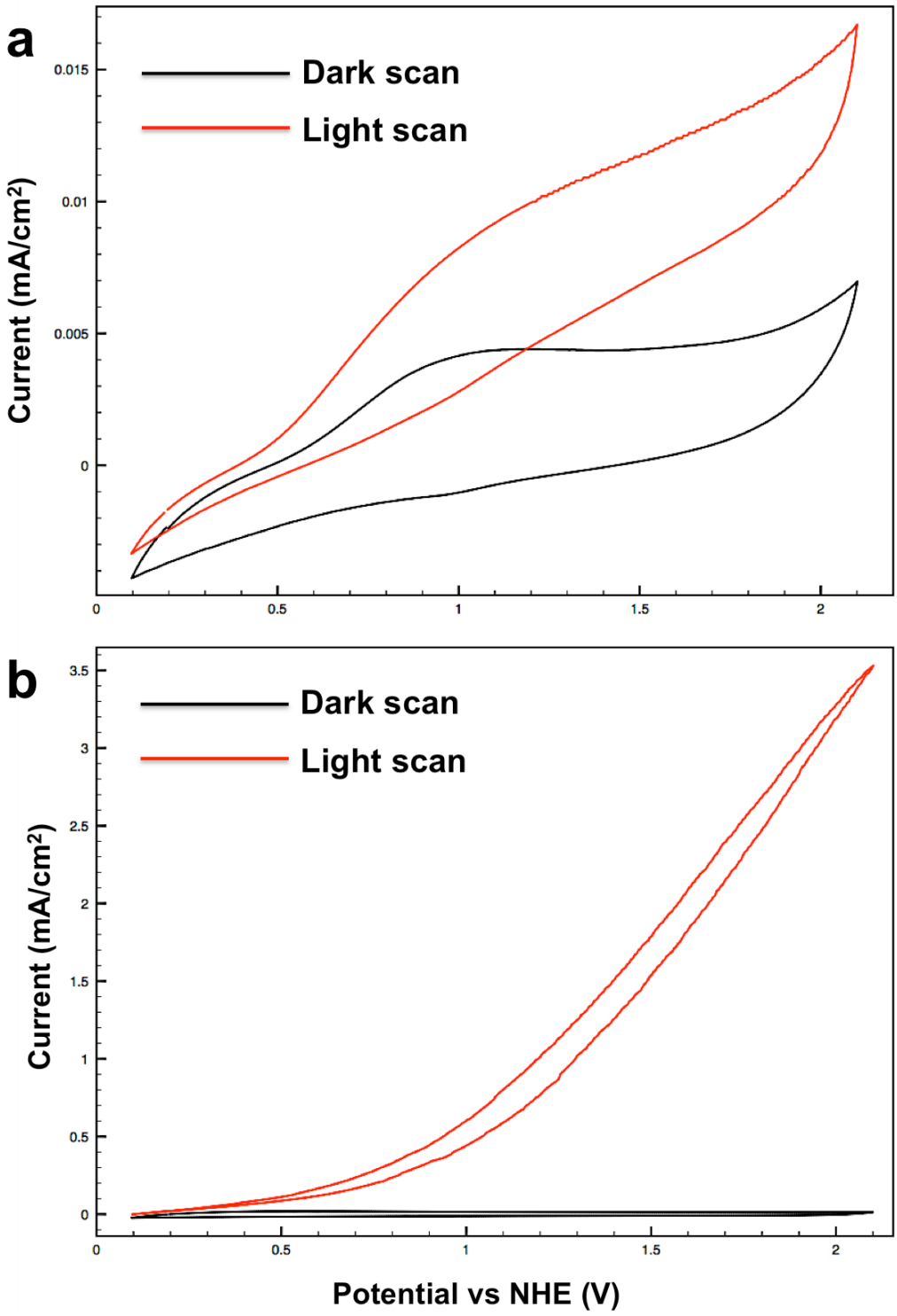

Figure 37. Cyclic voltammetry of (a) white template and (b) blue template. Illumination intensity I=100mW/cm^2 for light scan.

The effects of the nanowires on the photoelectrochemical performance are investigated by comparing blue templates with three samples with different lengths (200 nm, 1μm, 3μm) of the nanowires growing on the templates. At low light illumination intensity (10mW/cm^2), the bare template shows higher photocatalytic activity than the templates with nanowires, as seen in Figure 38a. With increasing light intensity, the templates with nanowires starts to show advantages over the bare template, as seen in Figure 38c. One the one hand, the nanowires growing on the templates have a diameter of ~15 nm, which is too thin to absorb light and produce extra photoelectrons. However, since the density of the nanowires is high on the templates, the drawback is that the nanowire array might reflect or block the light and reduce the illumination intensity that can reach the surface of the templates to produce electron-hole pairs, which can explain the reason for low activity of the nanowires samples under low illumination intensity. On the other hand, the nanowires are growing homo-epitaxially on the templates and behave like a single crystal. Thus, the holes produced through photo-excitation would be transferred along the nanowire in the (001) direction, which is the fastest charge transport orientation in rutile TiO_2 [168]. Therefore, when the illumination intensity is high enough, there would be a large quantity of electron-hole pairs produced in the templates, and the advantage of the nanowires would be performed for fast electron-hole separation to avoid recombination. In this work, it seems the short nanowires have the best performance for photocatalytic activity at high illumination intensity, and an optimum length of the

nanowire should exist for fast charge separation while avoiding blocking the light to the template surface.

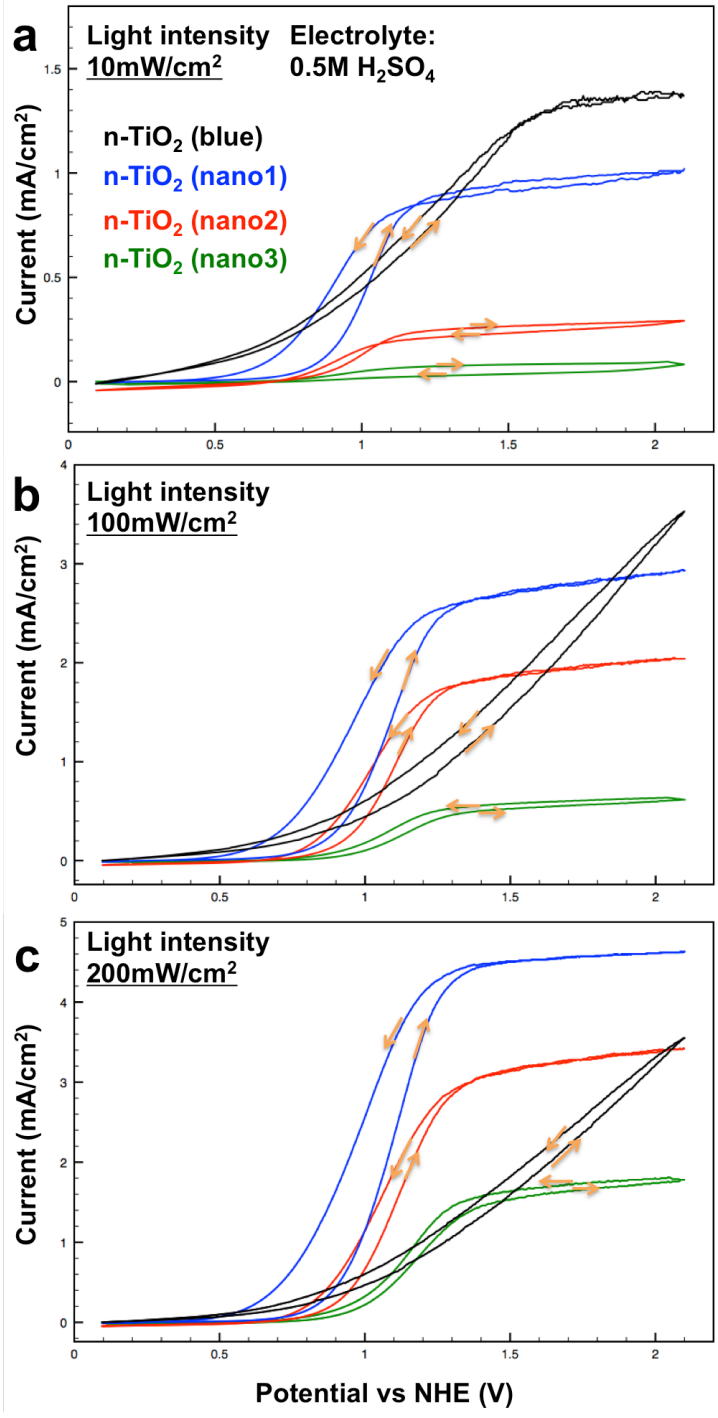

Figure 38. Characterization of photoelctrochemical activity of samples at different light illumination intensities. (black: N-TiO_2 blue) TiO_2 blue template, (blue: N-TiO_2 nano1) TiO_2 blue template with 200nm nanowires, (red: N-TiO_2 nano2) TiO_2 blue template with 1μm nanowires, (green: N-TiO_2 nano3) TiO_2 blue template with 3μm nanowires.

To further confirm the effects of the nanowires on the photocatalytic performance, TiO_2 nanowires at 1µm length with low density and regular density are compared. The 1µm length nanowire sample with regular density has a similar performance as the template, however, the nanowire performance is a combination of improved electron-hole separation and fewer electron-hole pairs produced by reduced light intensity. The low intensity nanowires still has the advantage for fast charge transfer. However, the low density arrays increased the exposed surface for absorbing light and produced more electron-hole pairs.

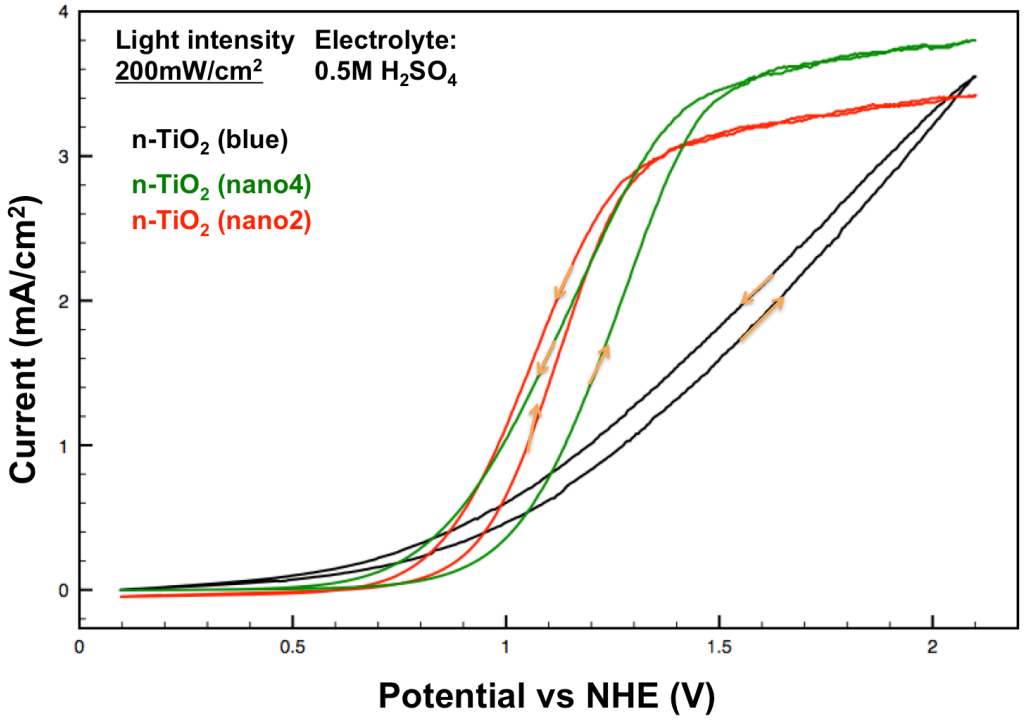

Figure 39. Characterization of photoelctrochemical activity of samples at different light illumination intensities. (black: N-TiO_2 blue) TiO_2 blue template, (blue: N-TiO_2 nano4) TiO_2 blue template with 1µm nanowires at low density, (green: N-TiO_2 nano2) TiO_2 blue template with 1µm nanowires at regular density.

Conclusions

In conclusion, TiO_2 nanowire-based thin films growing on novel templates were synthesized by hydrothermal reactions. The nanowires grew via a homo-epitaxial growth on TiO_2 templates. The growth orientations can be regulated with the templating system; the length of the nanowires can be precisely controlled by reaction time; the sharpness of the tips can be controlled via changing the diffusion rates of the precursor ions in the solution; and the density and diameter of the nanowires can be affected by controlling the oxygen deficiency and roughness of the templates. The photocatalytic activities of white and blue templates were compared, and it was demonstrated that the oxygen deficiency can greatly improve the performance. This is due to the modification in surface energy and band structure of the templates. The effects of the length of the nanowires on the photocatalytic activity were studied, and with lower light intensity, bare templates perform better than the templates with nanowires, while under high illumination intensity, the nanowires shows superior photocatalytic activity over bare templates. The performance of the high-density and low-density nanowire-based samples were compared. There should be an optimum length and density of the nanowires growing on the templates to achieve better performance. The TiO_2 nanowires synthesized on the templates in this work are very promising in applications including photocatalysis, solar hydrogen and photovoltaics.

Chapter 4.

Photocatalytic Zinc Oxide-Carbon Composite Materials

In Preparation

Wenting Hou, Chris Yang, Wei Tan, Jianxin Zhu, Pablo Cortez, Nichola Kinsinger and David Kisailus. Photocatalytic Zinc Oxide-Carbon Composite Materials.

ABSTRACT:

Based on inspiration from Nature, organic agents can be used to mimic organic-mineral interactions to yield ZnO-organic composite materials under mild solution conditions. The organics offer the potential to modify ZnO crystal nucleation and growth behavior, and provide a source of carbon. In this work, we have successfully synthesized ZnO-carbon composite materials via a hydrothermal method followed by thermal annealing. Crystal phase formation and evolution were examined by X-ray diffraction as well as transmission electron microscopy. Particle morphological behavior was investigated using scanning electron microscopy. Initially, a zinc-polyvinyl alcohol (Zn-PVA) composite structure was produced. PVA served as an organic matrix to guide the nucleation and crystal growth behavior, and limit the precursor diffusion, which yielded ZnO nanoparticles with uniform size distribution. During the annealing process, the semi-crystalline PVA decomposed to form graphitic and disordered carbon, while the hydrolyzed zinc species transformed from a layered basic zinc acetate to crystalline zinc oxide. The presence of this graphitic carbon will expedite electron transport, and therefore reduce electron-hole recombination within ZnO. The photocatalytic performance of ZnO-carbon nanostructures have shown promising results in exhibiting higher degradation rates than without carbon. Understanding the relationship between polymer and zinc species, and studying the annealing conditions on the growth of ZnO nanostructures will help to develop synthetic guidelines to enable efficient photocatalytic water treatment processes.

4.1. Introduction

With the development of industrial technologies, there are more newly evolved organic contaminants, such as pharmaceutical and endocrine disrupting compounds. The contaminants have been continuously emitted into our environment, especially in surface water systems. These have greatly affected human health and destroyed the ecological balance [196, 197]. Semiconducting materials such as TiO_2 and ZnO have attracted enormous attention as an excellent material for photocatalytic processes due to their high photosensitivity, non-toxic properties, etc [198-201]. The photocatalytic activity can be affected by photoelectrochemical properties, size, morphology and surface area of the semiconducting materials, which can be controlled by synthesis conditions, such as reaction time, temperature, pH and additive compounds [202-204].

In recent years, TiO_2 has been extensively studied and widely applied as a photocatalyst. However, ZnO is attracting more attention as an alternative to TiO_2 since ZnO has similar bandgap energy (3.2eV), but exceeds TiO_2 with lower cost and superior carrier mobility (ZnO: 200-1000 cm^2vs^{-1}, TiO_2=0.1~4 cm^2vs^{-1}) [27]. Many studies have reported on ZnO as a material for application in photocatalytic degradation of organic pollutants, and showed better performance for photocatalytic decomposition of some organic dye molecules than TiO_2 [199, 205, 206].

However, the photocatalytic efficiency achieved until now cannot meet practical applications. The bottleneck of the low efficiency is due to rapid electron-hole recombination. To improve the photo-generated electron-hole separation, a variety number of methods have been used to supply conjugated agents such as metals [207, 208] and

metal oxides [209, 210] to scavenge the electrons and reduce electron-hole recombination. Recently, carbon is widely used to capture and transport the photo-induced electrons through highly conductive carbon pathways. It has been reported that one-dimensional carbon nanofibers (CNF) [201], carbon nanotubes [211], graphene [212], Fullerene [213], and graphitic carbon [214] can effectively reduce the electron-hole recombination and improve photocatalytic performance. The combination of ZnO with carbon-based structures are promising for the superior electron transport properties, and have great potential for achieving high photocatalytic performance.

In this work, we have developed a novel synthesis method to produce uniformly distributed ZnO-carbon composite materials via a simple hydrothermal and annealing process. Based on inspiration from Nature, which utilizes organic to modify the nucleation and crystal growth processes of inorganic materials by organic-inorganic interactions [215, 216], we utilize PVA to mediate the synthesis of ZnO nanostructured materials. PVA can provide organic templating for producing a zinc-PVA composite material. After the annealing process, PVA decomposes to its carbon backbone in a graphitic carbon form, which greatly improved the photocatalytic performance.

4.2. Experimental Section

4.2.1 Material Synthesis

Zinc oxide-organic composites were synthesized under hydro-solvothermal conditions. Zinc acetate was used as the zinc precursor. A concentrated zinc acetate solution was prepared, and Poly vinyl alcohol (PVA MW ~ 40,000, 98-99%, Sigma

Aldrich) was subsequently added. The zinc acetate and PVA were combined to make solutions with a molar ratio of PVA : zinc acetate = 1:100, and the pH of the mixture solution was modified to 7.0 or 9.0 with ammonium hydroxide (30 wt% purchased from Acros Organics). The final concentrations of the zinc precursor solutions were 2.0 M. The modified solutions were immediately transferred into 23mL Teflon-lined hydrothermal reactors (Parr Instruments, Moline, IL) and heated to 150°C for 12 hours in convection ovens. The resulting ZnO-PVA products were in the form of rigid composites, which were cut into small pieces and then dehydrated by soaking in water for 24 hours, 50% water / 50% ethanol for 24 hours and followed by 100% ethanol for 24 hours. The dehydrated composites were then dried in a vacuum oven at room temperature. This dehydration and drying process maintains the structural integrity of the ZnO-PVA composites. The ZnO-PVA composite materials were then subsequently placed in an alumina boat and annealed in a tube furnace at varying temperatures (i.e., 200°C, 300°C, 400°C, 500°C, 600°C, and 800°C) for 1 hour at a rate of 10°C/minute, with air flowing at 60 cc / min to remove the organic within the composite and generate a ZnO nanocrystalline / carbon composite network.

ZnO without addition of polymer was synthesized using the same procedures as the ZnO-PVA composite materials. Briefly, concentrated zinc acetate or zinc nitrate precursors were prepared, and the pH of the solution was adjusted to 7 or 9 with an ammonium hydroxide solution. The resulting concentration of the zinc precursor was 2.0 M, and the solutions were transferred to hydrothermal reactors to conduct hydrothermal reactions at 150°C for 12 hours. The resulting powder was washed 3 times with DI water

and 2 times with ethanol to remove residual chemicals, and then the powder samples were dried in a vacuum oven and subsequently annealed in tube furnace at 500°C for 1 hour at a heating rate of 10°C/min. The samples were taken out of the tube furnace after cooling to ambient temperature for characterization and photocatalytic analysis.

4.2.2 Material Characterization

ZnO-PVA composites and resulting products were characterized using X-Ray Diffraction (XRD, PANalytical Empyrean) using Ni-filtered Cu Kα radiation at 45kV and 40mA within the 10-70° 2θ range. The crystalline size of the resulting products were calculated using the Scherer equation. The elemental composition of the materials were analyzed by Energy Dispersive Spectroscopy (EDS) and Raman microscopy. Raman spectroscopy measurements were carried out at room temperature in an ambient atmosphere using a 532 nm laser as the excitation source at 10 mW power.

The morphology and particle size of the products were observed with Scanning Electron Microscopy (SEM, FEI XL30) at 10kV accelerating voltage, and more morphology details of the products were determined using Transmission Electron Microscopy (TEM, FEI-PHILIPS CM300) at 300kV accelerating voltage for bright field imaging and electron diffraction analysis.

The thermal degradation processes of the ZnO-polymer composites were characterized using Thermal Gravimetric Analysis (TGA) and Differential Scanning Calorimetry (DSC). The composites materials were heated in air (flow rate ~20cm^3/min) at 10°C/min from 25°C to 1000°C.

The surface areas of samples were examined via Nitrogen Adsorption Surface Area Measurements (BET). The analyses for the surface areas were conducted at 77K using a Micrometritics ASAP 2020 (Norcross, GA). Before each measurement, ~ 100mg of sample was degassed at 90°C for 6 hours under vacuum. The adsorption isotherms of nitrogen at 77K were obtained using 40 relative pressure values ranging from 0.05 to 0.95.

The FTIR spectra were measured on a Nicolet 6700 FT-IR Spectrometer with an attenuated total reflectance (ATR) unit. Small quantities of samples were pressed onto the ATR window for the measurement.

4.2.3 Photocatalytic Performance

The photocatalytic activities of the products were investigated by measuring the degradation of Methylene Blue (MB) in the presence of ZnO-carbon or ZnO powder suspensions under UV illumination. The ZnO/ZnO-carbon suspension solutions were prepared by dispersing the sample powder in Milli-Q water, and the pH of the solutions were adjusted to 7.0 with dilute hydrochloric acid or ammonium hydroxide solutions. The resulting suspensions were sonicated for 5 minutes using a tip-horn ultrasonic processor (Hielscher UP100H, Ringwood, NJ). The suspensions were subsequently irradiated with a UV light (Phillips UV (A) 40 Watt bulb at 1 mW / cm^2) for 24 hours to remove any residual organics. To test the degradation reaction, a glass beaker filled with 100mL of 500 mg / L of ZnO suspension was prepared with the addition of Methylene Blue (MB 13μM) as targeting organic compound. A Phillips UV (A) 40 Watt bulb with the intensity of 1 mW / cm^2 was provided as light source. The concentrations of MB were measured at different reaction times, and the photocatalytic activity of ZnO was determined with UV-

Visible Spectroscopy (Bechman Coulter DU 800 Spectrophotometer) between 200 – 800 nm (λ_{max}=668nm).

4.3. Results and Discussion

4.3.1 Annealing Parameters Study

In this work, Polyvinyl alcohol (PVA) was used to assisting the nucleation and growth of ZnO nanostructures, and provides a carbon source via an annealing process. It is necessary to investigate an optimum annealing temperature for carbon formation, and at the same time to achieve ZnO nanostructures with appropriate size and morphology.

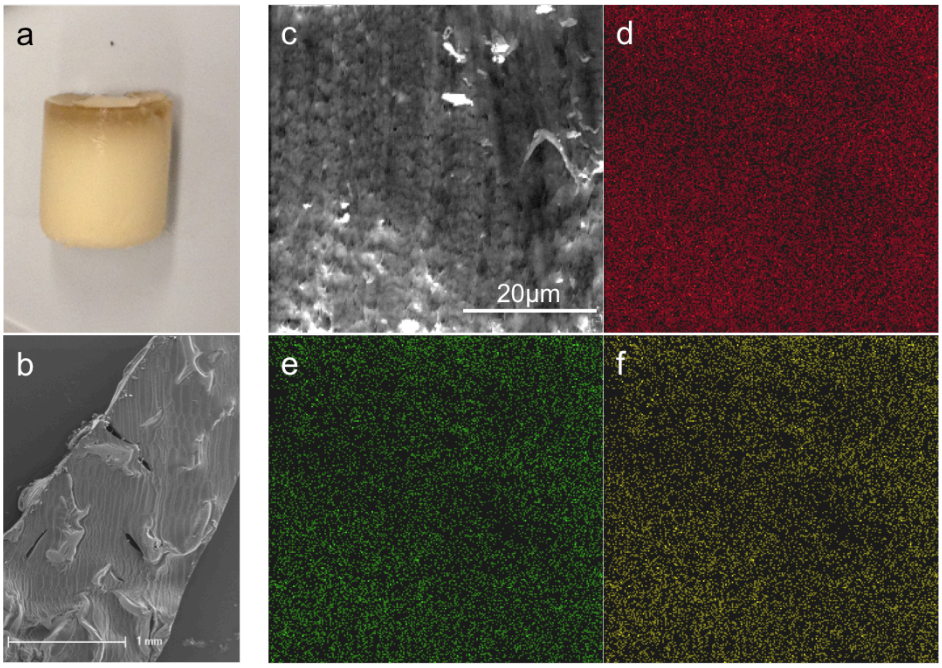

Figure 40. Illustration of Zn-PVA composite material (directly from reactor) formed from hydrothermal reaction at [Zn]=2M, pH=9, PVA:Zn=1:200, 150°C for 12 hours. (a) Photo image of Zn-PVA composite. (b) SEM micrograph of a section of Zn-PVA composite, (c) Zoom in SEM image and elemental maps of the corresponding area for (d) carbon, (e) Zinc, (f) Oxygen.

Zn-PVA composite materials were produced with a zinc precursor (zinc acetate) and PVA under an optimum pH using a hydrothermal method. The photographic image in Figure 40a displays a rigid and stable Zn-PVA composite material after a hydrothermal reaction. During the hydrothermal reaction, PVA chains act as an organic template with multiple OH-ligands which act as sites for hydrolyzed Zinc species that hydrogen bond to the polymer, effectively acting as a bridge to cross-link polymer chains. This linkage between the neighboring polymer chains leads to an increase in the viscosity of the solution [217]. Therefore, an elastic and rigid composite is formed. In figure 40b-f, SEM micrographs and EDS mapping of Zinc-PVA composite materials were conducted. Figure 40b indicates the SEM micrograph of a thin slice sectioned from the rigid composite material, and figure 40c is a higher magnification SEM of Figure 40b, revealing the uniformity of the whole sample, and no obvious heterogeneous structures have been observed inbetween the organic matrix. From the elemental mapping (Figure 40d-f) of an area in Zn-PVA composite material in Figure 40c, the carbon, zinc and oxygen species are relatively uniformly distributed.

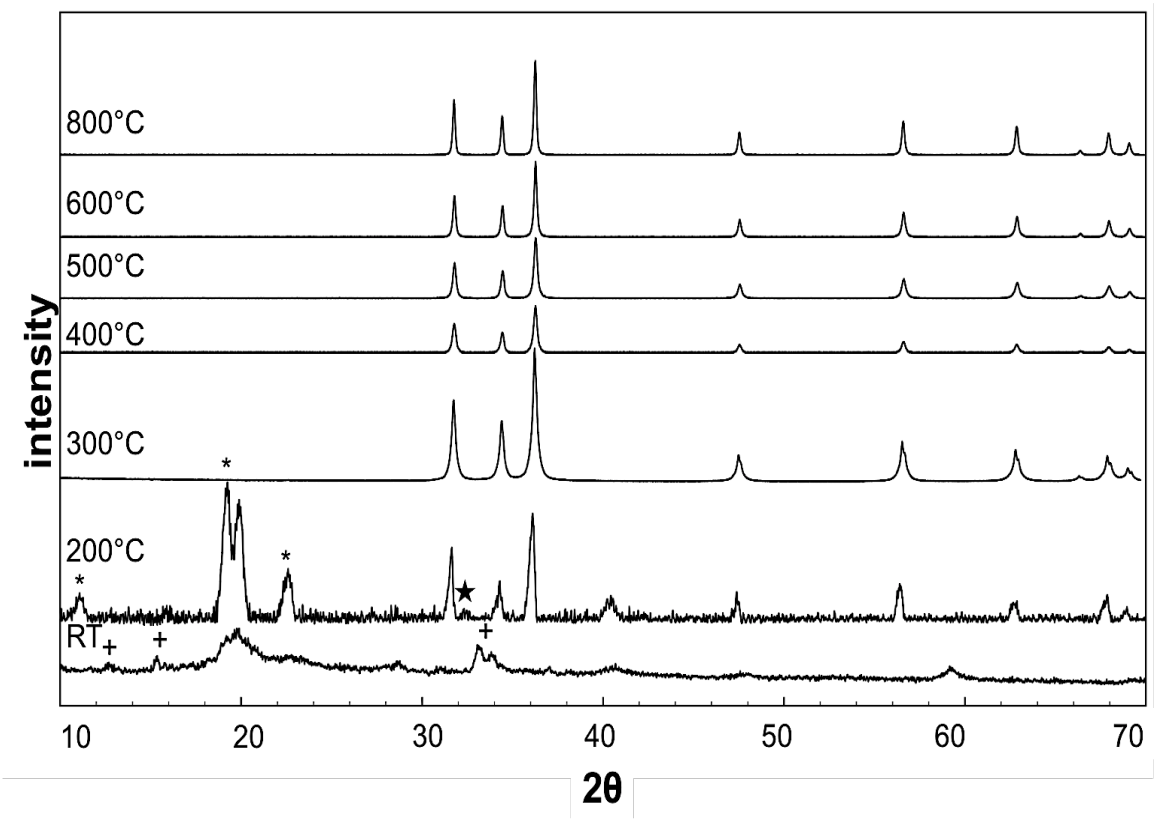

Figure 41. X-ray diffraction of ZnO nanocrystals produced from Zn-PVA composite ([Zn]=2M, PVA:Zn=1:200 at pH=9 150°C for 12hr) with increasing annealing temperature (200°C to 800°C) in air with 60cm^3/min flow rate. (* indicates crystalline PVA, + indicates layered basic zinc acetate, and ★ represents $Zn(OH)_2$)

The ZnO-carbon composite materials are produced by an annealing process. The annealing temperature plays an important role for controlling the formation of the ZnO-carbon nanoparticles. To investigate the evolution of ZnO-carbon nanostructures from polymer-assisted composite material, the sample was annealed in air at various temperatures. X-ray diffraction pattern in Figure 41 depicts the synthesis of ZnO-PVA composite materials at pH = 9 and 150°C for 12 hours (i.e., PVA:Zn=1:200, OH:Zn=4.5:1, using 2M Zinc acetate) and subsequently annealed in air for 1 hour at

different temperatures from 200°C to 800°C. The Zn-PVA composite material without annealing contains a combination of crystalline PVA and basic layered zinc acetate, and the peaks indicate the zinc species are very weak due to large amount of PVA. When the composite material is annealed in air at 200°C for 1 hour, a composition of crystalline PVA and ZnO are formed. Layered basic zinc acetate is decomposed resulting in the formation of a small amount of $Zn(OH)_2$. [218, 219] and an increase in the crystallinity of PVA. After the sample is annealed at 300°C to 800°C for 1 hour, only ZnO peaks are observed, and no PVA was detected. PVA is decomposed or consumed at higher annealing temperatures (> 300°C) [220]. With increasing annealing temperatures, the ZnO crystallite size increases from 10±1 nm at 200°C to 32±5 nm at 600°C.

Scanning electron microscopy (Figure 42) was used to confirm the particle size and morphology of ZnO nanoparticles at different annealing temperatures. With increasing temperature, the particle size continues to grow from ~10 nm at 200°C to 80±5 nm by 600°C and eventually to 180±30 nm by 800°C. The particle size distributions of all the samples are relatively uniform. Large aggregates or bulk structures have not been detected in the samples. This is likely due to the interaction of PVA, as a hydrophilic organic matrix, with Zn-species in controlling the nucleation and growth of ZnO nanoparticles. It is observed that the growth of the ZnO nanoparticles after the annealing are confined by aligned polymer chains that result in mat-like structures. This reveals the effects of PVA as a structure-directing organic agent for complexing Zinc species and guiding its formation process [221].

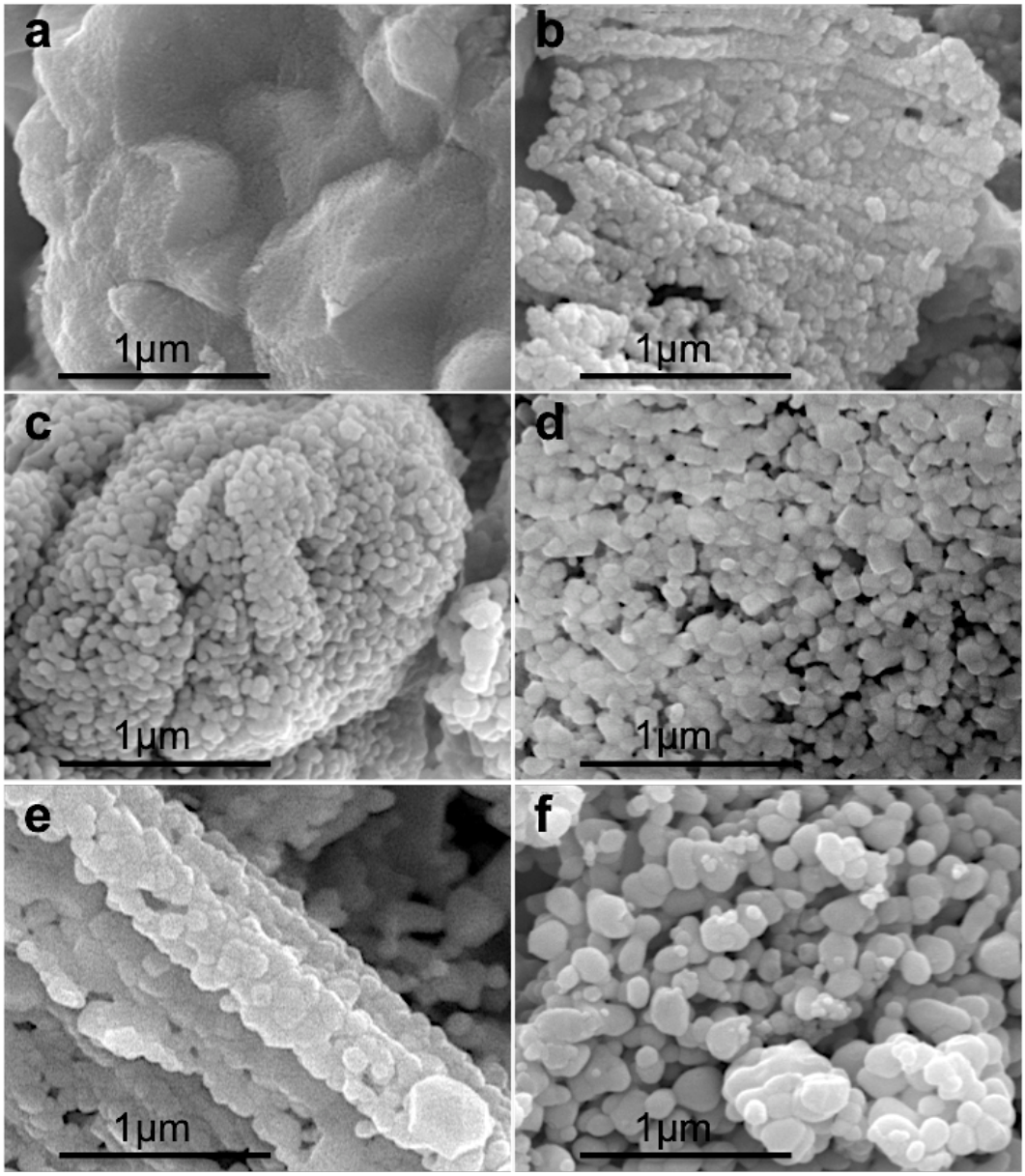

Figure 42. Scanning Electron Micrographs for ZnO nanoparticles after annealing for 1 hour in air at different temperatures (a) 200°C, (b) 300°C, (c) 400°C, (d) 500°C, (e) 600°C, (f) 800°C.

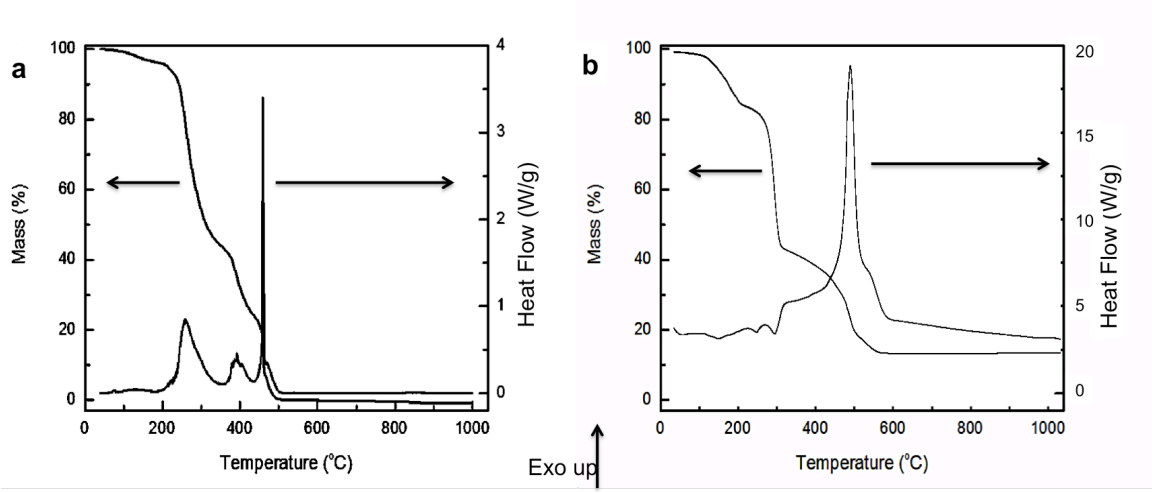

Figure 43. TGA/DSC for PVA and Zn-PVA composite materials heated in air flowing at 20 cc/min. (a) PVA; (b) Zn-PVA composite.

To further study the annealing process, Thermal Gravimetric Analysis (TGA) and Differential Scanning Calorimetry (DSC) in air were used to observe the decomposition of pure PVA and zinc-PVA composite materials from 25°C to 1000°C. It can be observed from Figure 43a that PVA alone undergoes significant weight loss by 400°C, with all the polymer removed by 500°C and only a small amount of carbon remaining (< 0.8 wt.%). Similar results have been observed [217]. TGA-DSC curves (figure 43b) of the Zn-PVA sample shift to a higher temperature, indicating the composite material is more thermally stable than pure PVA [222]. All of the organic in the composite sample annealed after 600°C will be completely decomposed, since there is no further weight loss after 600°C. The initial weight loss up to 120°C is due to the loss of bonded water to the layered basic zinc acetate and PVA in the composite materials. An endothermic peak between 120°C to 200°C, corresponding with a weight loss of 17%, is due to the decomposition of acetate groups in the layered basic zinc acetate structures[223] resulting in a phase transformation to

ZnO or $Zn(OH)_2$. DSC shows that endothermic peaks between 250°C to 320°C, are due to the structural decomposition of PVA [224]. It is believed that a chain-stripping elimination of water from the polymer forms polyene, which further decomposes to carbon. The weight loss and exothermic peak around 500°C is due to the carbonization from carbon to carbon dioxide. All the decomposition processes correspond to the XRD results discussed for the composite materials annealed at different temperatures in Figure 41.

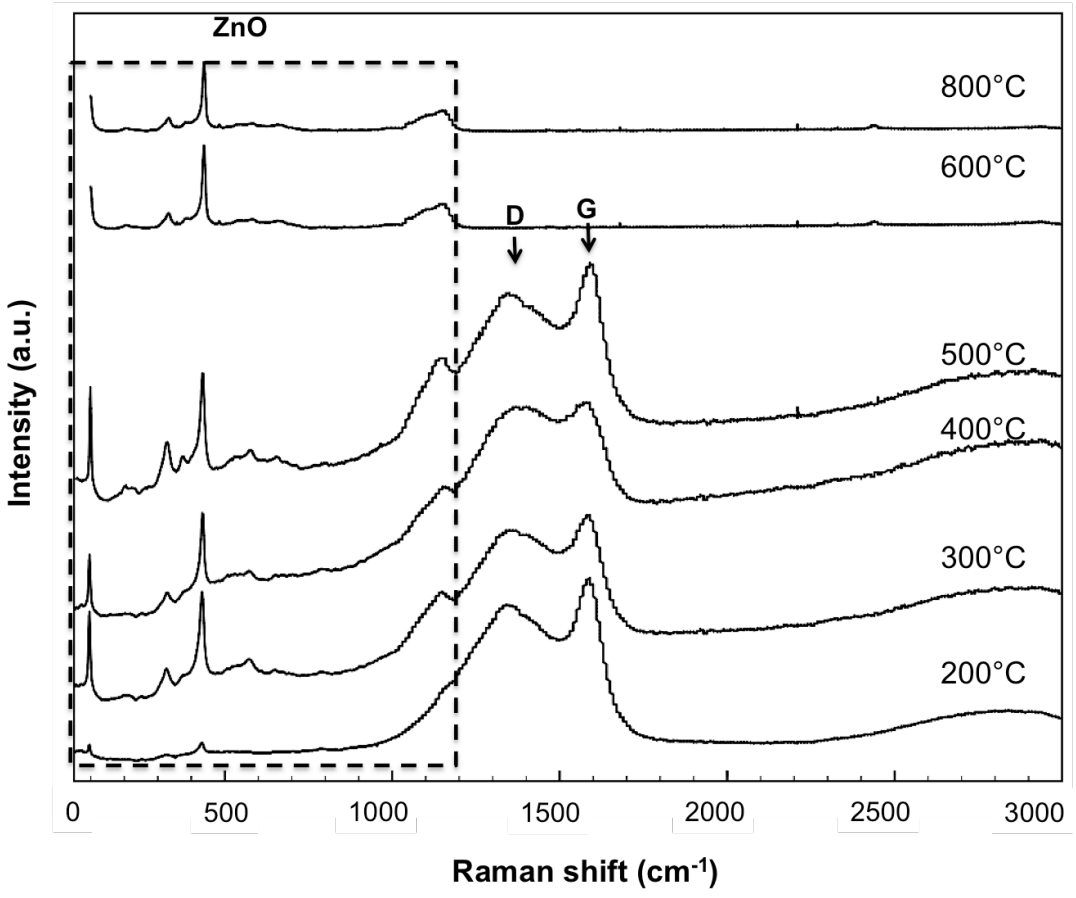

Figure 44. Raman spectroscopy of Zn-PVA composite materials annealed at different temperatures from 200°C to 800°C for 1 hour in air at 20 cc/min.

To analyze the resulting carbon in the samples annealed at different temperatures, Raman analysis (Figure 44) was conducted. Raman has been widely used for detecting and differentiating graphitic and disordered carbon. Graphitic carbon is well known to exhibit a better electron conductivity than disordered carbon [225]. Raman results reveal that there is no graphite or disordered carbon peaks observed in samples annealed at temperatures higher than 600°C. This confirms the complete decomposition of PVA after 600°C in the TGA/DSC analysis. The products annealed at 200°C to 500°C show intense peaks at 1355 cm^{-1} and 1584 cm^{-1}, attributed to disordered carbon (D) and graphitic (G) carbon, respectively. There is a broad peak at about 2700 cm^{-1}, which corresponds to the G' band (also called 2D band), originating from phonons with opposite momentum. From Figure 44, samples annealed from 200°C to 500°C all have a relatively higher intensity of graphitic peaks than disordered carbon, indicating a better electron conductivity. This is because graphitic carbon is known to have higher electronic conductivity than disordered carbon [225]. Among all of the samples, ZnO annealed at 500°C shows a higher intensity of graphite than disordered carbon. The decreased amount of disordered carbon is due to the decarburization process during high temperature annealing, and it can transform to carbon dioxide or graphitic carbon [226].

Table 4. Crystalline size, particle size and structural carbon data from annealed ZnO-PVA composite materials.

Annealing temperature	Crystalline size from XRD	Particle size from SEM	Intensity ratio of G/D from Raman
200°C	10 ± 1 nm	10 nm	1.08
300°C	15 ± 1 nm	30 ± 3 nm	1.01
400°C	21 ± 1 nm	40 ± 2 nm	1.00
500°C	28 ± 2 nm	60 ± 5 nm	1.10
600°C	32 ± 5 nm	80 ± 3 nm	N.A.
800°C	N.A.	180 ± 30 nm	N.A.

Based on our investigations from XRD, SEM, Raman and TGA, samples annealed under 200°C and 300°C still contain a large amount of amorphous PVA and impurities (zinc species). ZnO at 400°C has a relatively low intensity of graphitic carbon, and therefore the sample annealed at 500°C was selected as the annealing temperature for further analysis.

4.3.2 Investigation of PVA effects

ZnO materials were produced using a hydrothermal synthesis followed by an annealing process. The products synthesized with and without poly-vinyl alcohol (PVA) have been compared in order to investigate the effects of PVA (Figure 45). Figure 45a depicts X-ray diffraction patterns of ZnO produced in the absence of polymer at pH = 9 after a hydrothermal synthesis both before and after annealing. The resulting products

were identified as wurtzite ZnO without any impurity phase being detected. SEM micrographs (Figure 45b and d) demonstrate the morphological structure of the products before and after annealing process, respectively. After hydrothermal synthesis and before the annealing process, the products are composed of a majority of large rods and a small amount of star-shaped structures. The diameters of the rods are ~ 2-4 μm, and the lengths are ~ 4-8 μm. The surfaces of the rods are very rough, with some rods aggregated in the form of small rods or star shaped particles. After a 1 hour annealing process at 500°C, there is a slight increase in the particle size, while the concentration of the small particles decreased significantly. The surface of the products become smoother. This change may be due to the surface diffusion of ZnO, and similar results have been observed in an annealing study of $Li[Ni_{1/3}Co_{1/3}Mn_{1/3}]O_2$ at 600°C [172].

Figrue 45d shows X-ray diffraction patterns of ZnO produced with PVA at pH = 9 after hydrothermal synthesis before and after annealing. Unlike the products without PVA, the product before annealing is composed of semi-crystalline PVA, layered basic zinc acetate ($Zn(OH)_x(CH_3COO)_y \cdot zH_2O$, LBZA) and a small amount of ZnO. After the composite material is annealed at 500°C for 1 hour, the resulting product is transformed to pure wurtzite ZnO, with a crystalline size of ZnO was calculated to be 29±3 nm by the Sherrer equation and no PVA peaks were detected. This indicates the complete decomposition of PVA. Figure 45 e, f demonstrates the SEM micrographs of the ZnO-PVA composite materials before and after annealing. The product before annealing is a rigid ZnO-PVA composite material. A thin slice was sectioned for SEM, and it is

observed that the sample is homogeneous. After annealing, the sample is transformed to nanoparticles with the size about 30 nm.

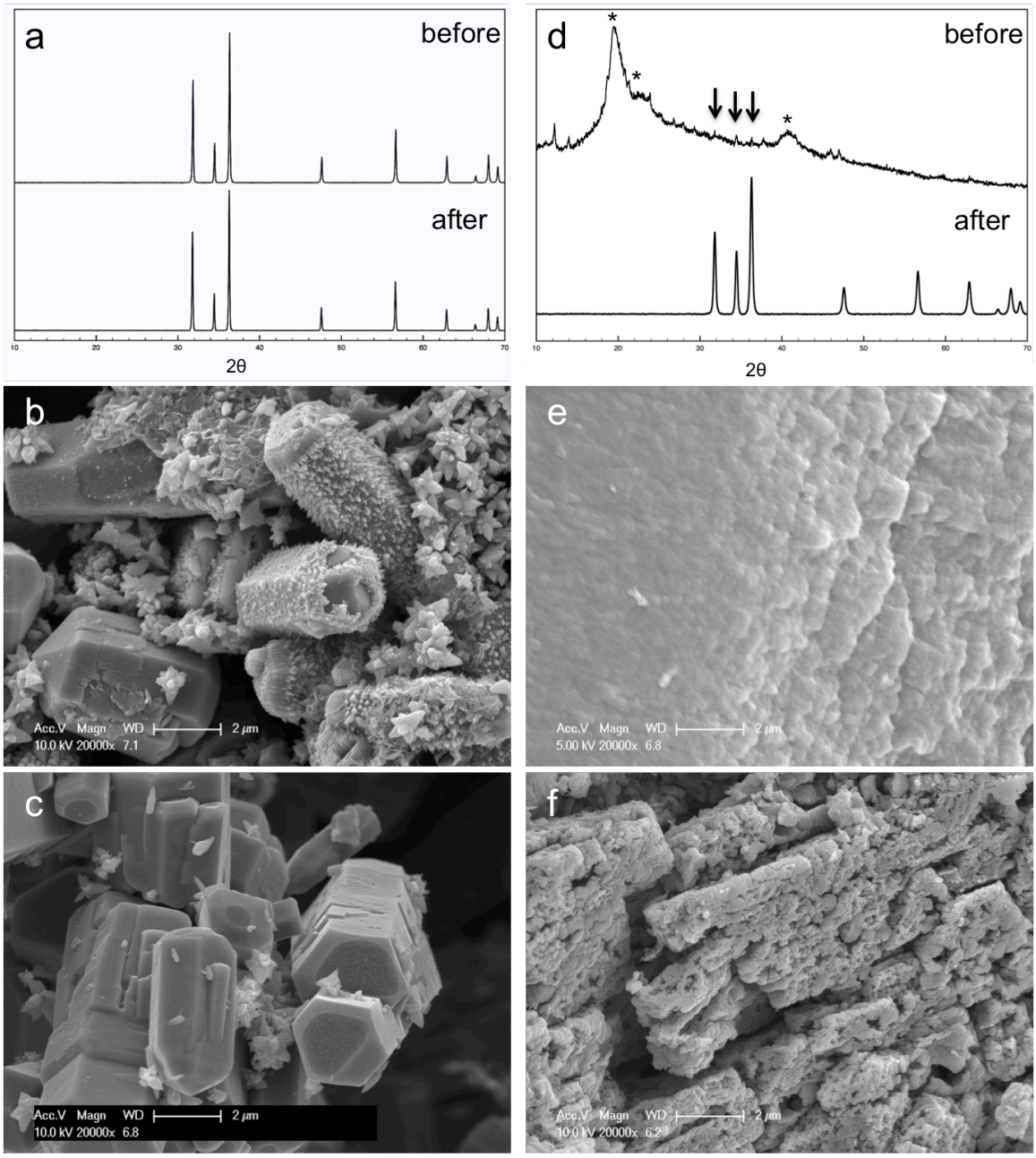

Figure 45. Comparison between ZnO products produced without PVA and with PVA, all samples were prepared with Zinc acetate as precursor, pH of solutions were adjusted to pH=9 with ammonium hydroxide, and the solutions were conducted hydrothermal reaction at 150°C for 12 hours. (a) XRD of ZnO without PVA before annealing process and after annealing process, SEM of ZnO without PVA (b) before annealing process and (c) after annealing process, (d) XRD of ZnO produced with PVA before annealing process and after annealing process, SEM of ZnO without PVA (e) before annealing process and (f) after annealing process.

Based on the comparison between the samples synthesized with PVA and without PVA, it is observed that the presence of PVA significantly reduces the crystallite and particle sizes of the resulting ZnO. We believe that PVA limits the diffusion of zinc precursor, reduces the dissolution of formed zinc species, and inhibits the aggregation of ZnO nanoparticles into large aggregates during the hydrothermal synthesis as the ZnO structure produced without PVA. Under high polymeric concentrations, the viscosity of the solution is too high for the zinc species to diffuse freely in the solution, which inhibits the crystal growth due to reduced crystal surface contact [217]. Also, PVA can crystallize to form an organic matrix with functional hydroxyl groups that mediate the nucleation and growth process of ZnO nanoparticles via electrostatic and covalent-coordination interactions [204]. Therefore, ZnO synthesized with PVA are uniform and have a small crystallite size. Conversely, the crystallinity of PVA is significantly enhanced by the presence of zinc acetate in the PVA/zinc acetate composite, revealing the interaction between PVA and zinc acetate molecules [227].

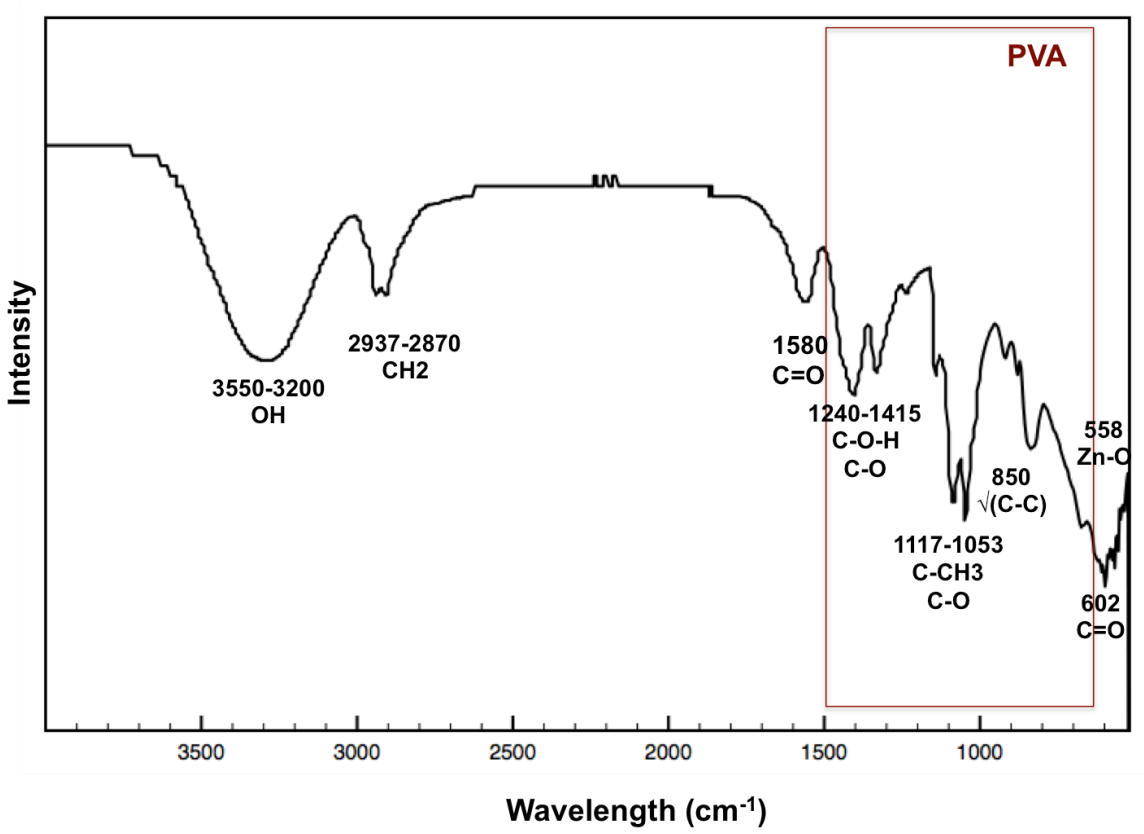

Figure 46. FTIR result for Zn-PVA composite materials after hydrothermal reaction ([Zn]=2M, pH=9, 150°C for 12hr).

Figure 46 depicts the IR result for the composite material. The peak around 558 cm^{-1} is due to Zn-O stretching, which may be indicated to ZnO, $Zn(OH)_4$ or LBZA in the polymer matrix, which is consistent with the XRD analysis. The O-H peak at 3200-3550 cm^{-1} corresponds to the –OH group of the functional hydroxyl group in PVA or –OH in hydrated surfaces of ZnO, and other peaks in the red box reveal the presence of PVA. The peaks at 1580 cm^{-1} and 602 cm^{-1} are due to the C=O stretching vibrations originating from the acetate groups, which confirms the complex of layered basic zinc acetate in the zinc-PVA composite material [227, 228].

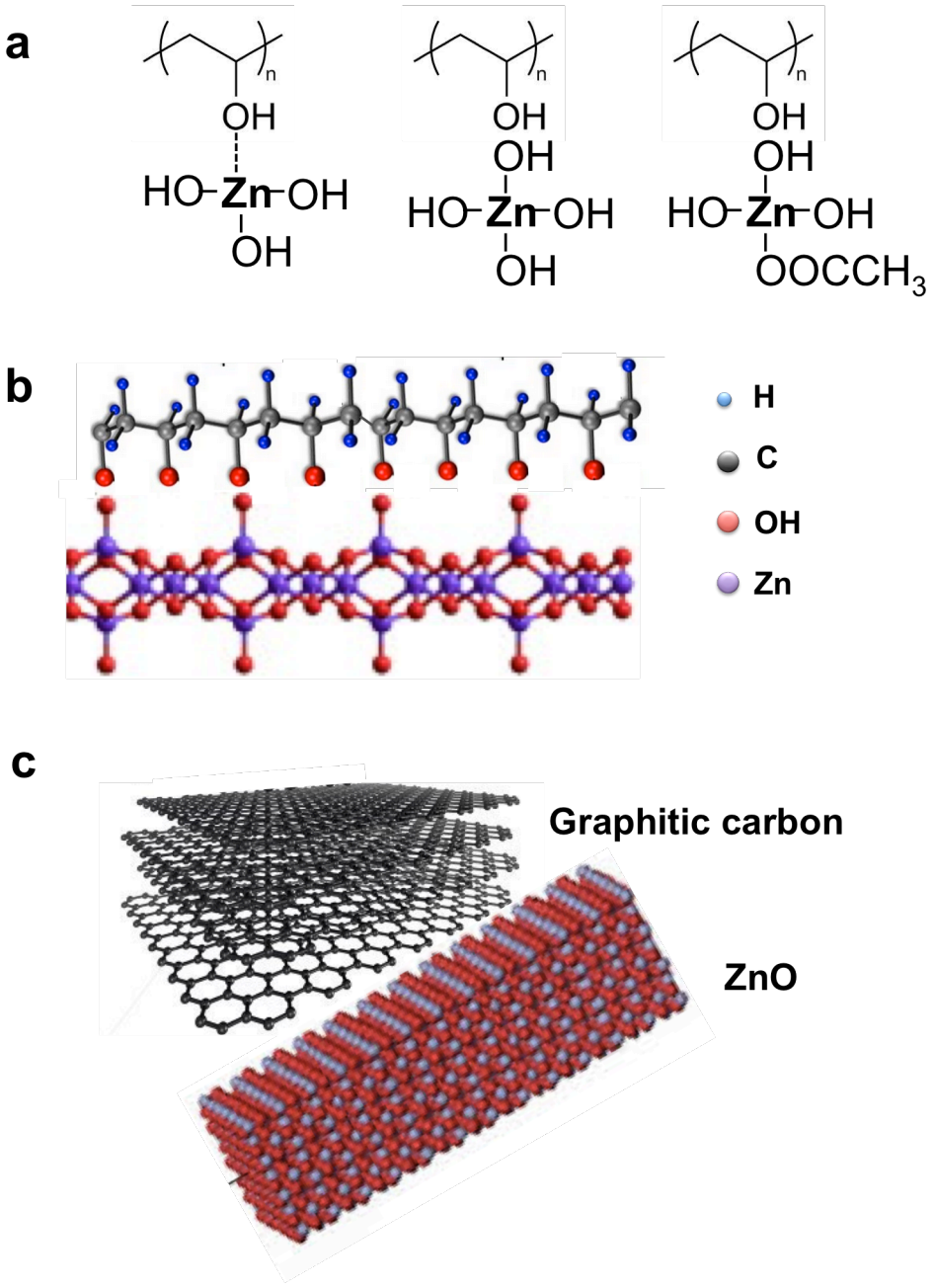

Figure 47. Schematics of the evolution of Zn-PVA composite materials. Potential PVA-Zinc species interactions (a) in solution, (b) after hydrothermal methods, (c) after annealing.

The interaction between zinc species in the solution and PVA is described in Figure 47. The zinc acetate ($Zn(CH_3COO)_2$) precursor cannot completely dissociate into Zn^{2+} since the acetate group (CH_3COO^-) can strongly chelate with Zn^{2+} ions [229]. After adding water, $Zn(CH_3COO)_2$ can be hydrolyzed, forming $Zn(OH)(CH_3COO)$, $Zn(OH)_2$ or $[Zn(OH)_4]^{2-}$ species as intermediates. The type of zinc complex depends on the pH of the solution. In this work, when the pH of the solution is adjusted to 9.0, the hydrolyzed zinc species $Zn(OH)_2$ or $[Zn(OH)_4]^{2-}$ will be dominant in the solution to interact with the hydroxyl groups on PVA and assemble by electrostatic and covalent-coordination interactions, as seen in Figure 47a. The concentrated solution is placed in autoclaves for hydrothermal reactions, and after the 150°C reaction for 12 hours, the solution transforms to a rigid and elastic composite structure, which has been confirmed to be layered basic zinc acetate and crystalline PVA. Figure 47b indicates the interaction between PVA and a complex layered structure $[Zn_x(OH)_y(H_2O)_2]^{2+}$ within the LBZA structure. There are a portion of zinc ions are octahedrally coordinated with six -OH groups, and another portion of zinc ions that are located above and below the empty octahedra and form tetrahedra composed of three OH groups and one water molecule. The resulting structural unit is a positively charged complex layer of $[Zn_x(OH)_y(H_2O)_2]^{2+}$ [218]. Figure 47c reveals the formation of ZnO-carbon composite structure after an annealing process. After the composite materials with polyvinyl alcohol were annealed at 500°C for 1 hour, it is found from previous Raman analysis confirmed that the sample consisted of ZnO nanocrystallites structure and graphite sheets. During annealing, some of the crystalline

polyvinyl alcohol decomposes into amorphous PVA and then to H_2O and CO_2, and the remaining crystalline PVA transformed to graphite layers [230]. LBZA would decompose into nano-crystalline ZnO [231]. Before annealing process, LBZA is covalent banded to crystalline PVA, with the decarburization at high annealing temperature, PVA will decompose to carbon and the ZnO nanoparticles bound to the carbon [230].

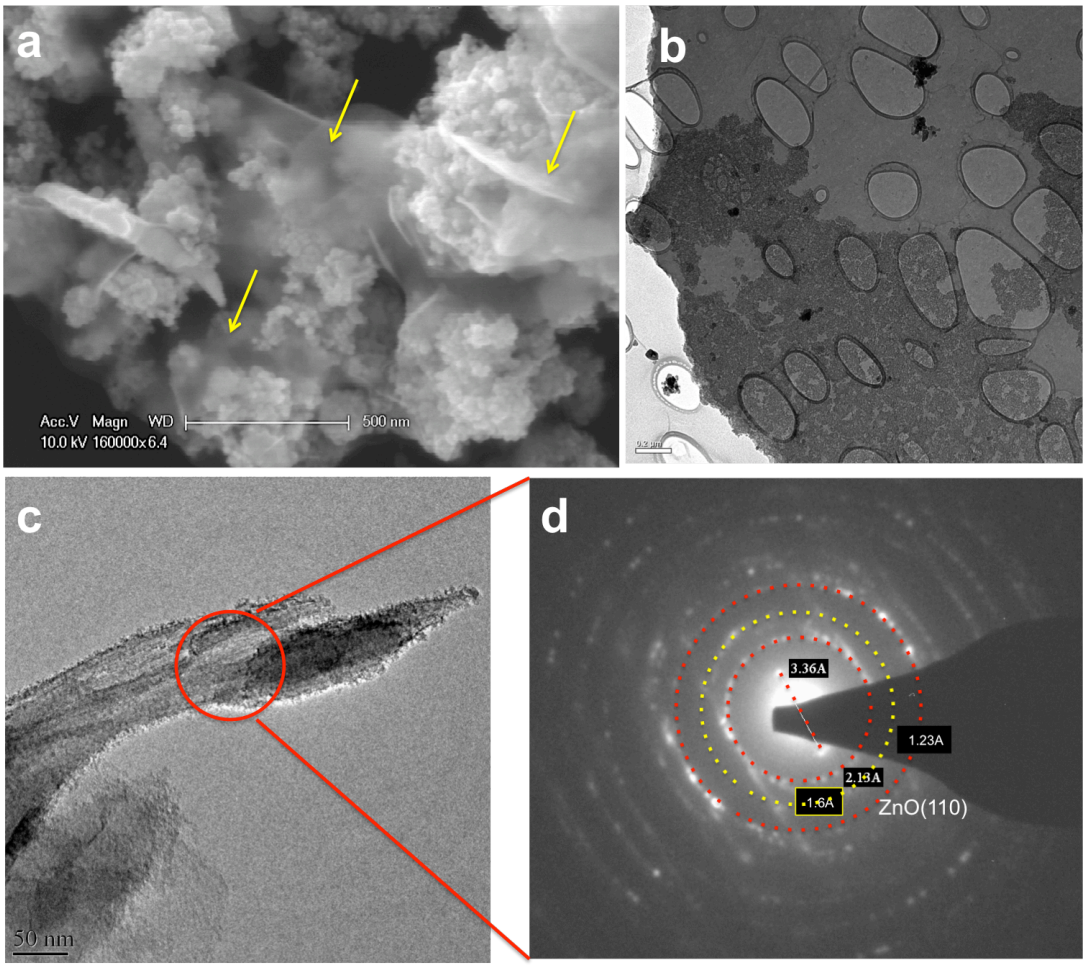

Figure 48. Characterization of a ZnO-carbon composite materials. (a) SEM micrograph of the ZnO-carbon composite material, (b) (c) TEM micrographs of the ZnO-carbon composite, (d) SAED from combination of carbon and ZnO nanoparticles (circled red area in (c))

In order to confirm the interaction between ZnO and graphitic carbon in the composite materials, high resolution SEM, TEM and SAED were conducted in the sample. In figure 48a, we observed that the small particles are wrapped inbetween the thin film structures (pointed with yellow arrows). It is believed that the thin film is composed of carbon. Further analysis was done using Bright field TEM analysis (Figure # (b) (c)). It is clear that the sample is composed of two parts, a layered structure in either flat (Figure 48b) or twisted (Figure 48c) conformations with nanoparticles adhering to the thin film surfaces. Selected area electron diffraction (SAED, Figure 48d) was done on the composite material (red circled area in Figure 48c) to reveal the presence of ZnO (yellow dotted circle) and graphitic carbon (red dotted circle), which confirms our speculation of the composition and phase of the thin film is crystalline graphitic carbon.

4.3.2 Photocatalytic Performance of ZnO-carbon Composite Materials

To study the effects of carbon in the photocatalytic degradation performance, Carbon-free ZnO nanoparticles and ZnO-carbon composite materials were compared. Carbon-free ZnO nanoparticles were synthesized using zinc nitrate, instead of zinc acetate as a zinc precursor to avoid the introduction of carbon element. Both samples are produced at pH = 7 in a hydrothermal reaction, followed by a 500°C annealing process in air for 1 hour.

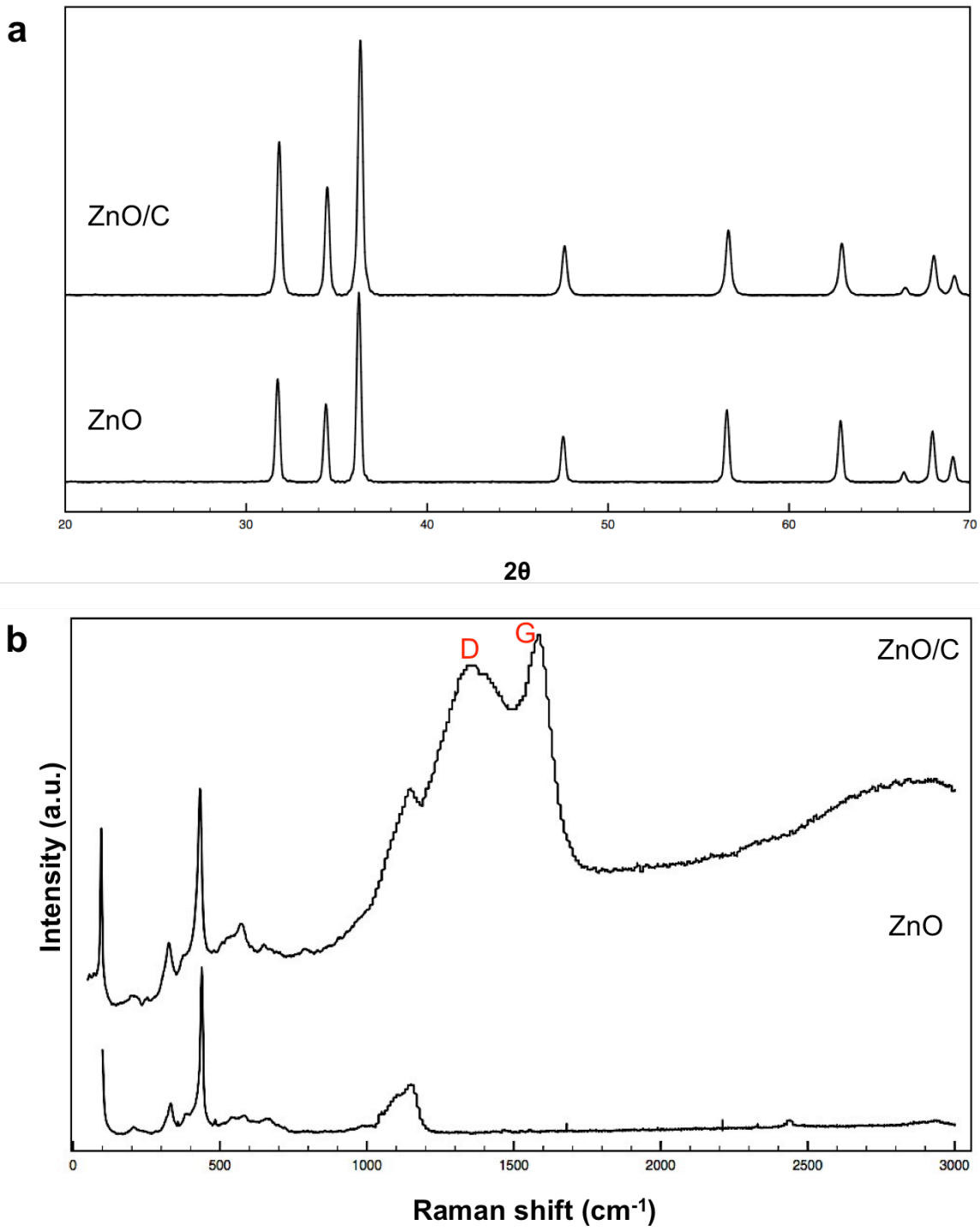

Figure 49. (a) XRD diffraction pattern for ZnO-carbon composite material and ZnO nanoparticles. (b) Raman spectroscopy of ZnO nanoparticle and ZnO-carbon composite material.

XRD in Figure 49a shows pure ZnO phase for both ZnO-carbon composite materials and the ZnO nanoparticles without any detectable impurities (such as zinc hydroxide or layered basic zinc acetate) and all of the peaks are indexed as wurtzite ZnO (JCPDS # 36-1451). The crystallite sizes of ZnO-carbon composite materials and ZnO nanoparticles were calculated to be 27.9±1.1 nm, 28.1±3.3 nm, respectively, using the full width at half maximum (FWHM) by the Scherrer equation.

From Figure 49b, the Raman peaks at 99 cm^{-1}, 439 cm^{-1}, 331 $cm^{-}1$, 1153 cm^{-1} indicate E_2^{low} Zn vibrations, E_2^{high} O vibrations, E_2^{high} - E_2^{low} O vibrations and second order or multiple phonon scattering of the Raman modes of the ZnO wurtzite structure, respectively. The representative peaks are observed from both pure ZnO and ZnO-carbon composite. There are two intense peaks differ ZnO-carbon composite material from ZnO nanoparticles at 1355 cm^{-1} and 1584 cm^{-1}, which correspond to the disordered (D) and Graphitic (G) bands of carbon respectively, indicating the presence of carbon in the sample. And in our result, it is clear that the graphitic peak at 1584 cm^{-1} has higher intensity than the disordered carbon peak at 1355 cm^{-1}. Both graphitic and disordered carbon are originated from the decomposition of PVA, that a part of matrix like structure of PVA transformed to layered graphitic carbon [230], while amorphous PVA forms disordered carbon after annealing in air, and part of the amorphous carbon can transform to graphitic carbon [226].

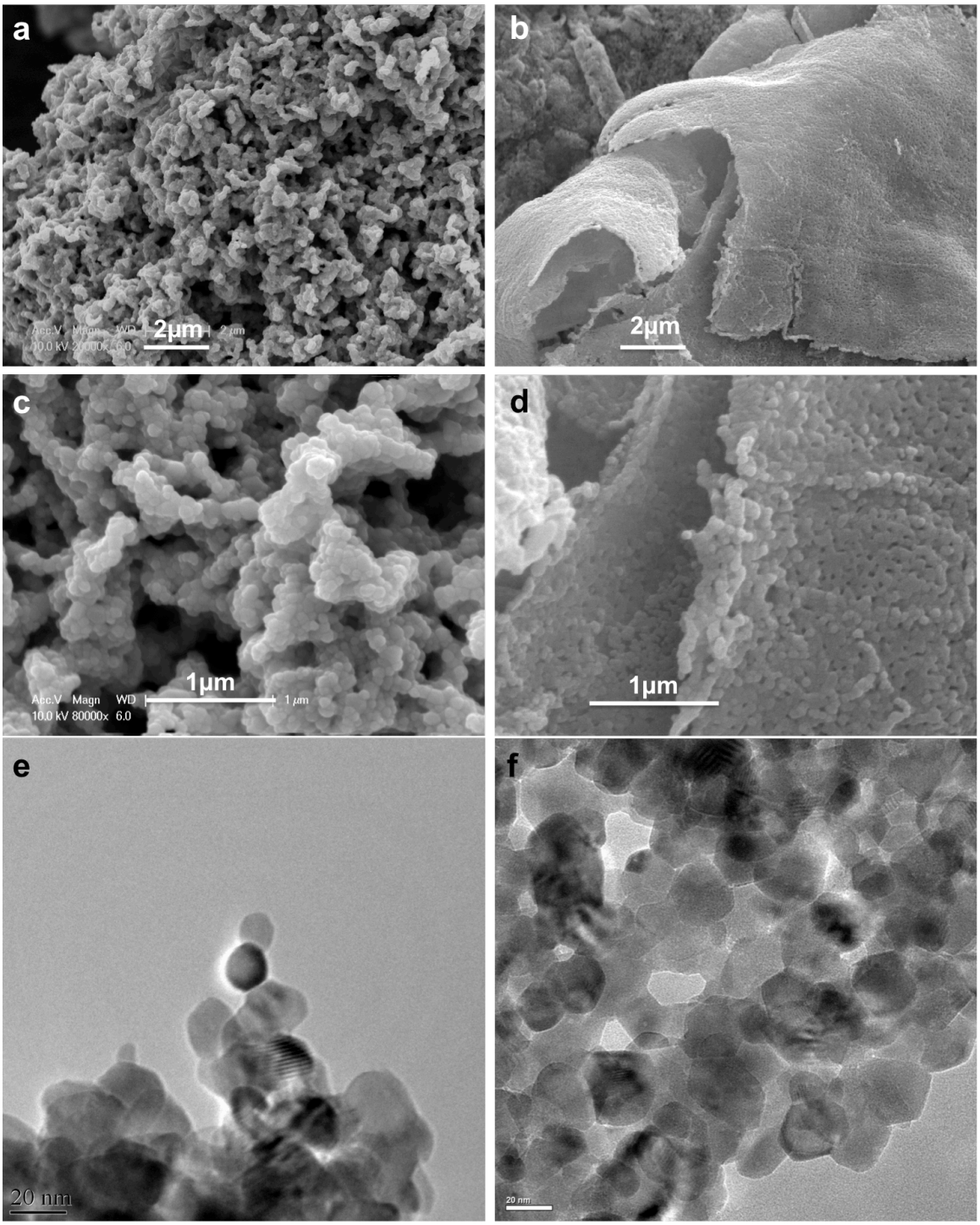

Figure 50. Characterization of morphology and particle/crystalline size for ZnO nanoparticles and ZnO-carbon composite material. SEM micrographs (a, c) and TEM micrograph (e) of ZnO nanoparticle without carbon, SEM micrographs (b, d) and TEM micrograph (f) of ZnO-carbon composite materials.

Figure 50 depicts the SEM and TEM micrographs for ZnO nanoparticles synthesized without a carbon-based precursor, and ZnO-carbon composite materials synthesized with PVA. From Figure 50 (b) and (d), the particle size of both pure ZnO and ZnO-carbon are both around 50 nm, and the morphological structure of the particles are also similar. From TEM micrographs (Figure #e, f), the crystalline size for ZnO nanoparticles and ZnO-carbon are measured to be 20±2 nm and 21±1 nm, respectively. BET was conducted on both samples and the surface area for pure ZnO and ZnO-carbon were 10.9 m^2/g and 10.2 m^2/g, respectively, which also confirm the comparability of the two samples.

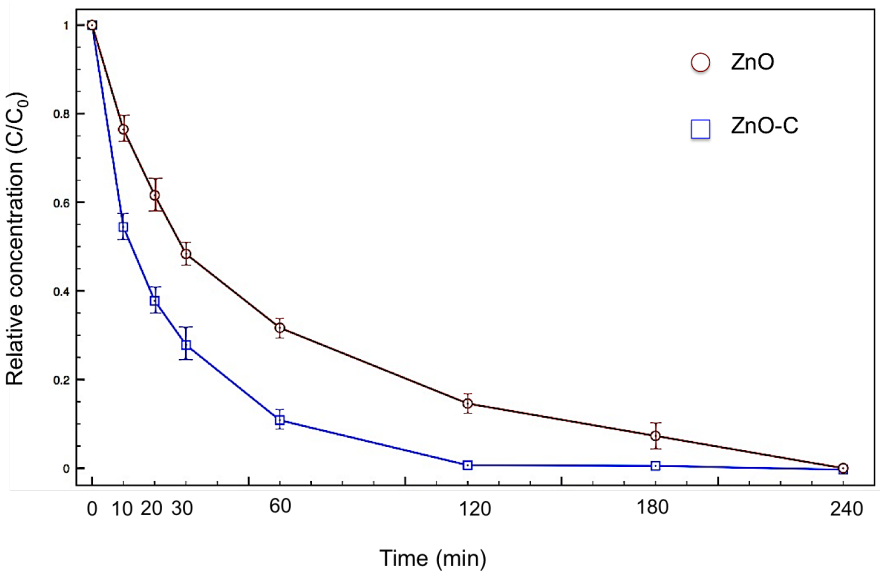

Figure 51. Photocatalytic degradation of MB versus time. Reactions were performed using ZnO nanoparticles and ZnO-carbon composite materials with similar size and morphology.

The photoactivities of pure ZnO nanoparticles and ZnO-carbon composite materials were evaluated by the degradation of Methylene Blue (MB) under UV irradiation to investigate the carbon effects on the photocatalytic performance. Figure 51 depicts time profiles of C/C_0 under UV irradiation, where C is the concentration of MB at the irradiation time t, and C_0 is the concentration in the absorption equilibrium of the photocatalyst before irradiation. There is an obvious increase in performance for the ZnO-carbon composite sample. The pure ZnO sample takes 4 hours to remove MB, while it only take 2 hours for the composite material to completely degrade MB. The samples have similar crystallite and particle sizes, morphologies and surface areas. The only difference between the two samples is the introduction of carbon into the composite material. Graphite is formed by the stacks of graphene sheets with an interplanar spacing of 0.335 nm, therefore, it has some superior properties similar to graphene, as shown in Figure 51c. The carrier mobility in graphitic carbon can be as high as 15,000 $cm^2V^{-1}s^{-1}$ [232], while in ZnO it is 200-1,000 $cm^2V^{-1}s^{-1}$ [233]. The increasing performance of the composite material is due to the high carrier mobility in graphitic carbon, when the electron and hole transport through ZnO to the surface, it will be quickly conducted to the attached graphitc carbon film [214]. Graphitic carbon helps to improve the charge separation and reduce the electron-hole recombination, therefore leading to a better performance than pure ZnO sample.

4.4. Conclusions

We developed a synthesis method for producing ZnO-carbon composite materials with superior photocatalytic performance. The ZnO-carbon composite is produced by PVA mediated hydrothermal synthesis, followed by an annealing process. The annealing process and the development of ZnO nanocrystals under different annealing temperatures were studied. The effects of PVA in the synthesis have been investigated. In the absence of PVA, large ZnO particles with non-uniform size distributions have been produced. While in the presence of PVA, nanosized, uniform ZnO structures have been fabricated. PVA, serves as an organic matrix for guiding the nucleation and growth process of ZnO nanoparticles; It also provides a source for graphitic carbon structures by annealing to improve charge separation and therefore increase the photocatalytic activity.

Chapter 5.

Conclusions

We have developed a one-pot solution-based method for branched ZnO rods under relatively mild conditions. The branched structures were modified by using EDA as a mineralizer under different zinc precursor and EDA concentrations. We observed that EDA plays an inhibitory role in nucleation, delaying complete hydrolysis and inducing secondary nucleation after initial formation of primary rods. This secondary nucleation lead to the formation of nanoparticles, which yielded branched structures growing from the prismatic faces of the primary rod. The branches formed via [10-11] /[0001] twins at the interface with the primary rod. By understanding of the growth mechanism, we can design nanostructures with high surface area for potential enhanced performance in dye-sensitized solar cells, photocatalysts and gas sensors.

We have synthesized TiO_2 nanowire-based thin films growing on novel templates by hydrothermal reactions. The nanowires are form via a homo-epitaxial growth on the templates, and the growth orientations can be regulated with the templating system; the length of the nanowires can be precisely controlled by reaction time; the sharpness of the tips can be controlled via changing the diffusion rates of the precursor ions in the solution; and the density and diameter of the nanowires can be affected by controlling the oxygen deficiencies (via oxygen concentration in the atmosphere) and roughness of the templates. The photocatalytic activities of white and blue templates were compared, and it was demonstrated that the oxygen deficiency can greatly improve the performance. The effects of the length of the nanowires on the photocatalytic activity were studied, and with lower light intensity, bare templates perform better than the templates with nanowires, while under high illumination intensity, the nanowires shows superior

photocatlytic activity over templates. The performance of the high-density and low-density nanowire films were compared. There should be an optimum length and density of the nanowires growing on the templates to achieve better performance. The TiO_2 nanowires synthesized on the templates are very promising in the applications including photocatalysis, solar hydrogen, photovoltaics.

We developed a synthesis method for producing ZnO-carbon composite materials with superior photocatalytic performance. The ZnO-carbon composite is produced by PVA mediated hydrothermal synthesis, followed by an annealing process. The annealing process and the development of ZnO nanocrystal under different annealing temperatures has been studied. The effects of PVA in the synthesis have been investigated. In the absence of PVA, large ZnO particles with non-uniform size distribution have been produced. While in the presence of PVA, nanosized, uniform ZnO structures have been fabricated. PVA serves as an organic matrix for guiding the nucleation and growth process of ZnO nanoparticles and also provides a source for graphitic carbon structures by annealing to improve charge separation and therefore increase the photocatalytic activity.

References

1. Pimentel, D.; Herz, M.; Glickstein, M.; Zimmerman, M.; Allen, R.; Becker, K.; Evans, J.; Hussain, B.; Sarsfeld, R.; Grosfeld, A., Renewable energy: current and potential issues. *BioScience* 2002, 52, 1111-1120.

2. Briefing, U. S., International Energy Outlook 2013. 2013.

3. Brown, M. T.; Cohen, M. J.; Sweeney, S., Predicting national sustainability: The convergence of energetic, economic and environmental realities. *Ecological Modelling* 2009, 220, 3424-3438.

4. Lewis, J. I.; Wiser, R. H., Fostering a renewable energy technology industry: An international comparison of wind industry policy support mechanisms. *Energy Policy* 2007, 35, 1844-1857.

5. Pelc, R.; Fujita, R. M., Renewable energy from the ocean. *Marine Policy* 2002, 26, 471-479.

6. Bridgwater, A. V., The Technical and Economic-Feasibility of Biomass Gasification for Power-Generation. *Fuel* 1995, 74, 631-653.

7. Gratzel, M., From space to earth: The story of solar electricity. *Nature* 2000, 403, 363-363.

8. Zhang, Q.; Dandeneau, C. S.; Zhou, X.; Cao, G., ZnO Nanostructures for Dye-Sensitized Solar Cells. *Adv Mater* 2009, 21, 4087-4108.

9. Zhang, Q.; Dandeneau, C. S.; Zhou, X.; Cao, G., ZnO Nanostructures for Dye Sensitized Solar Cells. *Adv Mater* 2009, 21, 4087-4108.

10. energy, U. S. d. o., 2012 renewable energy data book. *energy efficiency and renewable energy* 2012.

11. Zhang, J. Z., Metal oxide nanomaterials for solar hydrogen generation from photoelectrochemical water splitting. *Mrs Bull* 2011, 36, 48-55.

12. Alexander, B. D.; Kulesza, P. J.; Rutkowska, L.; Solarska, R.; Augustynski, J., Metal oxide photoanodes for solar hydrogen production. *J Mater Chem* 2008, 18, 2298-2303.

13. Cho, I. S.; Chen, Z. B.; Forman, A. J.; Kim, D. R.; Rao, P. M.; Jaramillo, T. F.; Zheng, X. L., Branched TiO2 Nanorods for Photoelectrochemical Hydrogen Production. *Nano Lett* 2011, 11, 4978-4984.

14. Ni, M.; Leung, M. K. H.; Leung, D. Y. C.; Sumathy, K., A review and recent developments in photocatalytic water-splitting using TiO2 for hydrogen production. *Renew Sust Energ Rev* 2007, 11, 401-425.

15. Dalrymple, O. K.; Yeh, D. H.; Trotz, M. A., Removing pharmaceuticals and endocrine-disrupting compounds from wastewater by photocatalysis. *J Chem Technol Biot* 2007, 82, 121-134.

16. Chong, M. N.; Jin, B.; Chow, C. W.; Saint, C., Recent developments in photocatalytic water treatment technology: a review. *Water research* 2010, 44, 2997-3027.

17. Hufschmidt, D.; Liu, L.; Selzer, V.; Bahnemann, D., Photocatalytic water treatment: fundamental knowledge required for its practical application. *Water Science & Technology* 2004, 49, 135-140.

18. Butti, K.; Perlin, J., *A golden thread: 2500 years of solar architecture and technology*. Cheshire books Palo Alto, CA, USA: 1980; Vol. 514.

19. Belessiotis, V.; Delyannis, E., The history of renewable energies for water desalination. *Desalination* 2000, 128, 147-159.

20. Mills, D., Advances in solar thermal electricity technology. *Sol Energy* 2004, 76, 19-31.

21. Tian, Y.; Zhao, C.-Y., A review of solar collectors and thermal energy storage in solar thermal applications. *Applied Energy* 2013, 104, 538-553.

22. Becquerel, A.-E., Recherches sur les effets de la radiation chimique de la lumière solaire, au moyen des courants électriques. *CR Acad. Sci* 1839, 9, 145-149.

23. Nelson, J., *The physics of solar cells*. World Scientific: 2003; Vol. 57.

24. Zhao, J.; Wang, A.; Green, M. A.; Ferrazza, F., 19.8% efficient ìhoneycombî textured multicrystalline and 24.4% monocrystalline silicon solar cells. *Appl Phys Lett* 1998, 73, 1991.

25. Hagfeldt, A.; Boschloo, G.; Sun, L. C.; Kloo, L.; Pettersson, H., Dye-Sensitized Solar Cells. *Chem Rev* 2010, 110, 6595-6663.

26. Oregan, B.; Gratzel, M., A Low-Cost, High-Efficiency Solar-Cell Based on Dye-Sensitized Colloidal Tio2 Films. *Nature* 1991, 353, 737-740.

27. Mor, G. K.; Shankar, K.; Paulose, M.; Varghese, O. K.; Grimes, C. A., Use of highly-ordered TiO2 nanotube arrays in dye-sensitized solar cells. *Nano Lett* 2006, 6, 215-218.

28. Grätzel, M., Solar energy conversion by dye-sensitized photovoltaic cells. *Inorg Chem* 2005, 44, 6841-6851.

29. Dominici, L.; Colonna, D.; D'Ercole, D.; Mincuzzi, G.; Riccitelli, R.; Michelotti, F.; Brown, T.; Reale, A.; Di Carlo, A., Dye Solar Cells: Basic and Photon Management Strategies. ISBN: 2011; pp 978-953.

30. Gratzel, M., Conversion of sunlight to electric power by nanocrystalline dye-sensitized solar cells. *Journal of Photochemistry and Photobiology A: Chemistry* 2004, 164, 3-14.

31. Gratzel, M., Photoelectrochemical cells. 2001.

32. O'Regan, B.; Gratzeli, M., A low-cost, high-efficiency solar cell based on dye-sensitized. *Nature* 1991, 353, 24.

33. Mathew, S.; Yella, A.; Gao, P.; Humphry-Baker, R.; Curchod, B. F.; Ashari-Astani, N.; Tavernelli, I.; Rothlisberger, U.; Nazeeruddin, M. K.; Grätzel, M., Dye-sensitized solar cells with 13% efficiency achieved through the molecular engineering of porphyrin sensitizers. *Nature chemistry* 2014.

34. Burschka, J.; Pellet, N.; Moon, S.-J.; Humphry-Baker, R.; Gao, P.; Nazeeruddin, M. K.; Grätzel, M., Sequential deposition as a route to high-performance perovskite-sensitized solar cells. *Nature* 2013, 499, 316-319.

35. Nissfolk, J.; Fredin, K.; Hagfeldt, A.; Boschloo, G., Recombination and transport processes in dye-sensitized solar cells investigated under working conditions. *The Journal of Physical Chemistry B* 2006, 110, 17715-17718.

36. Gr‰tzel, M., Solar energy conversion by dye-sensitized photovoltaic cells. *Inorg Chem* 2005, 44, 6841-6851.

37. Gratzel, M., Conversion of sunlight to electric power by nanocrystalline dye-sensitized solar cells. *Journal of Photochemistry and Photobiology A: Chemistry* 2004, 164, 3-14.

38. Wang, Z. L., Zinc oxide nanostructures: growth, properties and applications. *Journal of Physics: Condensed Matter* 2004, 16, R829.

39. Tornow, J.; Schwarzburg, K., Transient electrical response of dye-sensitized ZnO nanorod solar cells. *The Journal of Physical Chemistry C* 2007, 111, 8692-8698.

40. Leschkies, K. S.; Divakar, R.; Basu, J.; Enache-Pommer, E.; Boercker, J. E.; Carter, C. B.; Kortshagen, U. R.; Norris, D. J.; Aydil, E. S., Photosensitization of ZnO nanowires with CdSe quantum dots for photovoltaic devices. *Nano Lett* 2007, 7, 1793-1798.

41. Guo, M.; Diao, P.; Wang, X.; Cai, S., The effect of hydrothermal growth temperature on preparation and photoelectrochemical performance of ZnO nanorod array films. *J Solid State Chem* 2005, 178, 3210-3215.

42. Jiang, C.; Sun, X.; Lo, G.; Kwong, D.; Wang, J., Improved dye-sensitized solar cells with a ZnO-nanoflower photoanode. *Appl Phys Lett* 2007, 90, 263501.

43. Mandal, T.; Gregory, D., Hydrogen: a future energy vector for sustainable development. *Proceedings of the institution of mechanical engineers, part C: journal of mechanical engineering science* 2010, 224, 539-558.

44. Lauermann, G.; Häussinger, P.; Lohmüller, R.; Watson, A. M., Hydrogen, 1. Properties and Occurrence. *Ullmann's Encyclopedia of Industrial Chemistry*.

45. Ogden, J. M., Prospects for building a hydrogen energy infrastructure. *Annual Review of Energy and the Environment* 1999, 24, 227-279.

46. Fujishima, A.; Honda, K., Electrochemical photocatalysis of water at a semiconductor electrode. *Nature* 1972, 238, 37-38.

47. Ni, M.; Leung, M. K.; Leung, D. Y.; Sumathy, K., A review and recent developments in photocatalytic water-splitting using TiO2 for hydrogen production. *Renewable and Sustainable Energy Reviews* 2007, 11, 401-425.

48. Nakade, S.; Saito, Y.; Kubo, W.; Kitamura, T.; Wada, Y.; Yanagida, S., Influence of TiO2 nanoparticle size on electron diffusion and recombination in dye-sensitized TiO2 solar cells. *The Journal of Physical Chemistry B* 2003, 107, 8607-8611.

49. Anderson, N. A.; Lian, T., Ultrafast electron transfer at the molecule-semiconductor nanoparticle interface. *Annu. Rev. Phys. Chem.* 2005, 56, 491-519.

50. Diebold, U., The surface science of titanium dioxide. *Surf Sci Rep* 2003, 48, 53-229.

51. Ni, M.; Leung, M. K. H.; Leung, D. Y. C.; Sumathy, K., A review and recent developments in photocatalytic water-splitting using TiO2 for hydrogen production. *Renewable and Sustainable Energy Reviews* 2007, 11, 401-425.

52. Gr‰tzel, M., Photoelectrochemical cells. *Nature* 2001, 414, 338ñ344.

53. Sakthivel, S.; Shankar, M.; Palanichamy, M.; Arabindoo, B.; Bahnemann, D.; Murugesan, V., Enhancement of photocatalytic activity by metal deposition: characterisation and photonic efficiency of Pt, Au and Pd deposited on TiO< sub> 2</sub> catalyst. *Water Research* 2004, 38, 3001-3008.

54. Bamwenda, G. R.; Tsubota, S.; Nakamura, T.; Haruta, M., Photoassisted hydrogen production from a water-ethanol solution: a comparison of activities of Au TiO< sub> 2</sub> and Pt TiO< sub> 2</sub>. *Journal of Photochemistry and Photobiology A: Chemistry* 1995, 89, 177-189.

55. Wu, N.-L.; Lee, M.-S., Enhanced TiO< sub> 2</sub> photocatalysis by Cu in hydrogen production from aqueous methanol solution. *Int J Hydrogen Energ* 2004, 29, 1601-1605.

56. Liu, S.; Qu, Z.; Han, X.; Sun, C., A mechanism for enhanced photocatalytic activity of silver-loaded titanium dioxide. *Catal Today* 2004, 93, 877-884.

57. Li, Y.; Lu, G.; Li, S., Photocatalytic production of hydrogen in single component and mixture systems of electron donors and monitoring adsorption of donors by in situ infrared spectroscopy. *Chemosphere* 2003, 52, 843-850.

58. Koca, A.; Şahin, M., Photocatalytic hydrogen production by direct sun light from sulfide/sulfite solution. *Int J Hydrogen Energ* 2002, 27, 363-367.

59. Abe, R.; Sayama, K.; Sugihara, H., Development of new photocatalytic water splitting into H2 and O2 using two different semiconductor photocatalysts and a shuttle redox mediator IO3-/I. *The Journal of Physical Chemistry B* 2005, 109, 16052-16061.

60. Sayama, K.; Arakawa, H., Effect of Na< sub> 2</sub> CO< sub> 3</sub> addition on photocatalytic decomposition of liquid water over various semiconductor catalysis. *Journal of Photochemistry and Photobiology A: Chemistry* 1994, 77, 243-247.

61. Arab, S.; Li, D.; Kinsinger, N.; Zaera, F.; Kisailus, D., Solvothermal synthesis of a highly branched Ta-doped TiO2. *J Mater Res* 2011, 26, 2653-2659.

62. Colon, G.; Maicu, M.; Hidalgo, M. s.; Navio, J., Cu-doped TiO< sub> 2</sub> systems with improved photocatalytic activity. *Applied Catalysis B: Environmental* 2006, 67, 41-51.

63. Wang, C.-y.; Bahnemann, D. W.; Dohrmann, J. K., A novel preparation of iron-doped TiO2 nanoparticles with enhanced photocatalytic activity. *Chem Commun* 2000, 1539-1540.

64. Choi, W.; Termin, A.; Hoffmann, M. R., The role of metal ion dopants in quantum-sized TiO2: correlation between photoreactivity and charge carrier recombination dynamics. *The Journal of Physical Chemistry* 1994, 98, 13669-13679.

65. Choi, Y.; Umebayashi, T.; Yoshikawa, M., Fabrication and characterization of C-doped anatase TiO 2 photocatalysts. *J Mater Sci* 2004, 39, 1837-1839.

66. Di Valentin, C.; Pacchioni, G.; Selloni, A.; Livraghi, S.; Giamello, E., Characterization of paramagnetic species in N-doped TiO2 powders by EPR spectroscopy and DFT calculations. *The Journal of Physical Chemistry B* 2005, 109, 11414-11419.

67. Jimmy, C., Synthesis of hierarchical nanoporous F-doped TiO2 spheres with visible light photocatalytic activity. *Chem Commun* 2006, 1115-1117.

68. Zuo, F.; Wang, L.; Wu, T.; Zhang, Z.; Borchardt, D.; Feng, P., Self-doped Ti3+ enhanced photocatalyst for hydrogen production under visible light. *J Am Chem Soc* 2010.

69. Kang, M. G.; Han, H.-E.; Kim, K.-J., Enhanced photodecomposition of 4-chlorophenol in aqueous solution by deposition of CdS on TiO< sub> 2</sub>. *Journal of Photochemistry and Photobiology A: Chemistry* 1999, 125, 119-125.

70. Dhanalakshmi, K.; Latha, S.; Anandan, S.; Maruthamuthu, P., Dye sensitized hydrogen evolution from water. *Int J Hydrogen Energ* 2001, 26, 669-674.

71. Nowotny, J.; Bak, T.; Nowotny, M.; Sheppard, L., Titanium dioxide for solar-hydrogen I. Functional properties. *Int J Hydrogen Energ* 2007, 32, 2609-2629.

72. Malato, S.; Fernández-Ibáñez, P.; Maldonado, M.; Blanco, J.; Gernjak, W., Decontamination and disinfection of water by solar photocatalysis: recent overview and trends. *Catal Today* 2009, 147, 1-59.

73. Becher, P.; Orlich, M.; Kosmidou, A.; König, M.; Baroth, M.; Thiel, H.-J., Genetic diversity of pestiviruses: identification of novel groups and implications for classification. *Virology* 1999, 262, 64-71.

74. Zwiener, C.; Richardson, S. D.; De Marini, D. M.; Grummt, T.; Glauner, T.; Frimmel, F. H., Drowning in disinfection byproducts? Assessing swimming pool water. *Environ Sci Technol* 2007, 41, 363-372.

75. Prasse, C.; Ternes, T., Removal of Organic and Inorganic Pollutants and Pathogens from Wastewater and Drinking Water Using Nanoparticles–A Review. In *Nanoparticles in the Water Cycle*, Springer: 2010; pp 55-79.

76. Kolpin, D. W.; Thurman, E. M.; Lee, E. A.; Meyer, M. T.; Furlong, E. T.; Glassmeyer, S. T., Urban contributions of glyphosate and its degradate AMPA to streams in the United States. *Sci Total Environ* 2006, 354, 191-197.

77. Lissemore, L.; Hao, C.; Yang, P.; Sibley, P. K.; Mabury, S.; Solomon, K. R., An exposure assessment for selected pharmaceuticals within a watershed in Southern Ontario. *Chemosphere* 2006, 64, 717-729.

78. Robert, D.; Malato, S., Solar photocatalysis: a clean process for water detoxification. *Sci Total Environ* 2002, 291, 85-97.

79. Gaya, U. I.; Abdullah, A. H., Heterogeneous photocatalytic degradation of organic contaminants over titanium dioxide: a review of fundamentals, progress and problems. *Journal of Photochemistry and Photobiology C: Photochemistry Reviews* 2008, 9, 1-12.

80. Sunada, K.; Kikuchi, Y.; Hashimoto, K.; Fujishima, A., Bactericidal and detoxification effects of TiO2 thin film photocatalysts. *Environ Sci Technol* 1998, 32, 726-728.

81. Linsebigler, A. L.; Lu, G.; Yates Jr, J. T., Photocatalysis on TiO2 surfaces: principles, mechanisms, and selected results. *Chem Rev* 1995, 95, 735-758.

82. Sakthivel, S.; Neppolian, B.; Shankar, M.; Arabindoo, B.; Palanichamy, M.; Murugesan, V., Solar photocatalytic degradation of azo dye: comparison of photocatalytic efficiency of ZnO and TiO< sub> 2</sub>. *Sol Energ Mat Sol C* 2003, 77, 65-82.

83. Daneshvar, N.; Salari, D.; Khataee, A., Photocatalytic degradation of azo dye acid red 14 in water on ZnO as an alternative catalyst to TiO< sub> 2</sub>. *Journal of Photochemistry and Photobiology A: Chemistry* 2004, 162, 317-322.

84. Chakrabarti, S.; Dutta, B. K., Photocatalytic degradation of model textile dyes in wastewater using ZnO as semiconductor catalyst. *J Hazard Mater* 2004, 112, 269-278.

85. Ozgur, U.; Hofstetter, D.; Morkoc, H., ZnO Devices and Applications: A Review of Current Status and Future Prospects. *P Ieee* 2010, 98, 1255-1268.

86. Ozgur, U.; Alivov, Y. I.; Liu, C.; Teke, A.; Reshchikov, M. A.; Dogan, S.; Avrutin, V.; Cho, S. J.; Morkoc, H., A comprehensive review of ZnO materials and devices. *J Appl Phys* 2005, 98, -.

87. Klingshirn, C. F., Zinc Oxide-From Fundamental Properties Towards Novel Applications. *UCR Lib* 2007.

88. Hou, W.; Lancaster, L.; Li, D.; Bowlus, A.; Bozhilov, K.; Kisailus, D., Biologically inspired synthesis of highly branched zinc oxide nanowires. 2013.

89. Ohyama, M.; Kouzuka, H.; Yoko, T., Sol-gel preparation of ZnO films with extremely preferred orientation along (002) plane from zinc acetate solution. *Thin Solid Films* 1997, 306, 78-85.

90. Liu, X.; Wu, X.; Cao, H.; Chang, R., Growth mechanism and properties of ZnO nanorods synthesized by plasma-enhanced chemical vapor deposition. *J Appl Phys* 2004, 95, 3141-3147.

91. Vayssieres, L., Growth of arrayed nanorods and nanowires of ZnO from aqueous solutions. *Adv Mater* 2003, 15, 464-466.

92. Feng, X.; Feng, L.; Jin, M.; Zhai, J.; Jiang, L.; Zhu, D., Reversible super-hydrophobicity to super-hydrophilicity transition of aligned ZnO nanorod films. *J Am Chem Soc* 2004, 126, 62-63.

93. Yu, H.; Zhang, Z.; Han, M.; Hao, X.; Zhu, F., A general low-temperature route for large-scale fabrication of highly oriented ZnO nanorod/nanotube arrays. *J Am Chem Soc* 2005, 127, 2378-2379.

94. Bai, X.; Gao, P.; Wang, Z. L.; Wang, E., Dual-mode mechanical resonance of individual ZnO nanobelts. *Appl Phys Lett* 2003, 82, 4806.

95. Landmann, M.; Rauls, E.; Schmidt, W., The electronic structure and optical response of rutile, anatase and brookite TiO2. *Journal of Physics: Condensed Matter* 2012, 24, 195503.

96. Reyes-Coronado, D.; Rodriguez-Gattorno, G.; Espinosa-Pesqueira, M.; Cab, C.; De Coss, R.; Oskam, G., Phase-pure TiO2 nanoparticles: anatase, brookite and rutile. *Nanotechnology* 2008, 19, 145605.

97. Scanlon, D. O.; Dunnill, C. W.; Buckeridge, J.; Shevlin, S. A.; Logsdail, A. J.; Woodley, S. M.; Catlow, C. R. A.; Powell, M. J.; Palgrave, R. G.; Parkin, I. P., Band alignment of rutile and anatase TiO2. *Nature materials* 2013, 12, 798-801.

98. Grätzel, M.; Rotzinger, F. P., The influence of the crystal lattice structure on the conduction band energy of oxides of titanium (IV). *Chemical physics letters* 1985, 118, 474-477.

99. Bickley, R. I.; Gonzalez-Carreno, T.; Lees, J. S.; Palmisano, L.; Tilley, R. J. D., A structural investigation of titanium dioxide photocatalysts. *J Solid State Chem* 1991, 92, 178-190.

100. Ohno, T.; Tokieda, K.; Higashida, S.; Matsumura, M., Synergism between rutile and anatase TiO2 particles in photocatalytic oxidation of naphthalene. *Applied Catalysis A: General* 2003, 244, 383-391.

101. González-García, L.; González-Valls, I.; Lira-Cantu, M.; Barranco, A.; González-Elipe, A. R., Aligned TiO2 nanocolumnar layers prepared by PVD-GLAD for transparent dye sensitized solar cells. *Energ Environ Sci* 2011, 4, 3426-3435.

102. Yoshitake, H.; Sugihara, T.; Tatsumi, T., Preparation of wormhole-like mesoporous TiO2 with an extremely large surface area and stabilization of its surface by chemical vapor deposition. *Chem Mater* 2002, 14, 1023-1029.

103. Li, D.; Soberanis, F.; Fu, J.; Hou, W.; Wu, J.; Kisailus, D., Growth Mechanism of Highly Branched Titanium Dioxide Nanowires via Oriented Attachment. *Cryst Growth Des* 2013, 13, 422-428.

104. Kinsinger, N. M.; Wong, A.; Li, D.; Villalobos, F.; Kisailus, D., Nucleation and crystal growth of nanocrystalline anatase and rutile phase TiO2 from a water-soluble precursor. *Cryst Growth Des* 2010, 10, 5254-5261.

105. Antonelli, D. M.; Ying, J. Y., Synthesis of hexagonally packed mesoporous TiO2 by a modified sol–gel method. *Angewandte Chemie International Edition in English* 1995, 34, 2014-2017.

106. Siegel, R.; Ramasamy, S.; Hahn, H.; Zongquan, L.; Ting, L.; Gronsky, R., Synthesis, characterization, and properties of nanophase TiO2. *J Mater Res* 1988, 3, 1367-1372.

107. Bavykin, D. V.; Friedrich, J. M.; Walsh, F. C., Protonated titanates and TiO2 nanostructured materials: synthesis, properties, and applications. *Adv Mater* 2006, 18, 2807-2824.

108. Ding, K.; Miao, Z.; Liu, Z.; Zhang, Z.; Han, B.; An, G.; Miao, S.; Xie, Y., Facile synthesis of high quality TiO2 nanocrystals in ionic liquid via a microwave-assisted process. *J Am Chem Soc* 2007, 129, 6362-6363.

109. Chen, X.; Li, C.; Gr√§tzel, M. l.; Kostecki, R.; Mao, S. S., Nanomaterials for renewable energy production and storage. *Chem Soc Rev* 2012, 41, 7909-7937.

110. Green, M. A.; Emery, K.; Hishikawa, Y.; Warta, W.; Dunlop, E. D., Solar cell efficiency tables (version 39). *Progress in Photovoltaics: Research and Applications* 2012, 20, 12-20.

111. Han, L.; Islam, A.; Chen, H.; Malapaka, C.; Chiranjeevi, B.; Zhang, S.; Yang, X.; Yanagida, M., High-efficiency dye-sensitized solar cell with a novel co-adsorbent. *Energ Environ Sci* 2012, 5, 6057-6060.

112. Look, D.; Reynolds, D.; Sizelove, J.; Jones, R.; Litton, C.; Cantwell, G.; Harsch, W., Electrical properties of bulk ZnO. *Solid State Commun* 1998, 105, 399-401.

113. Zhang, Q. F.; Dandeneau, C. S.; Zhou, X. Y.; Cao, G. Z., ZnO Nanostructures for Dye-Sensitized Solar Cells. *Adv Mater* 2009, 21, 4087-4108.

114. Anta, J. A.; GuilleÃÅn, E.; Tena-Zaera, R., ZnO-Based Dye-Sensitized Solar Cells. *The Journal of Physical Chemistry C* 2012, 116, 11413-11425.

115. Jagadish, C.; Pearton, S. J., *Zinc oxide bulk, thin films and nanostructures: processing, properties, and applications*. Elsevier Science: 2006.

116. Elkhidir Suliman, A.; Tang, Y.; Xu, L., Preparation of ZnO nanoparticles and nanosheets and their application to dye-sensitized solar cells. *Sol Energ Mat Sol C* 2007, 91, 1658-1662.

117. Baxter, J. B.; Aydil, E. S., Nanowire-based dye-sensitized solar cells. *Appl Phys Lett* 2005, 86, 053114-053114-3.

118. Han, J.; Fan, F.; Xu, C.; Lin, S.; Wei, M.; Duan, X.; Wang, Z. L., ZnO nanotube-based dye-sensitized solar cell and its application in self-powered devices. *Nanotechnology* 2010, 21, 405203.

119. Kisailus, D.; Schwenzer, B.; Gomm, J.; Weaver, J. C.; Morse, D. E., Kinetically controlled catalytic formation of zinc oxide thin films at low temperature. *J Am Chem Soc* 2006, 128, 10276-10280.

120. Xu, F.; Sun, L., Solution-derived ZnO nanostructures for photoanodes of dye-sensitized solar cells. *Energ Environ Sci* 2011, 4, 818-841.

121. Xia, Y.; Yang, P.; Sun, Y.; Wu, Y.; Mayers, B.; Gates, B.; Yin, Y.; Kim, F.; Yan, H., One‚ÄêDimensional Nanostructures: Synthesis, Characterization, and Applications. *Adv Mater* 2003, 15, 353-389.

122. Law, M.; Greene, L. E.; Johnson, J. C.; Saykally, R.; Yang, P., Nanowire dye-sensitized solar cells. *Nature materials* 2005, 4, 455-459.

123. Jiang, C. Y.; Sun, X. W.; Lo, G. Q.; Kwong, D. L.; Wang, J. X., Improved dye-sensitized solar cells with a ZnO-nanoflower photoanode. *Appl Phys Lett* 2007, 90.

124. Kong, Y.; Yu, D.; Zhang, B.; Fang, W.; Feng, S., Ultraviolet-emitting ZnO nanowires synthesized by a physical vapor deposition approach. *Appl Phys Lett* 2001, 78, 407-409.

125. Wu, J. J.; Liu, S. C., Low-temperature growth of well-aligned ZnO nanorods by chemical vapor deposition. *Adv Mater* 2002, 14, 215.

126. Huang, M. H.; Wu, Y.; Feick, H.; Tran, N.; Weber, E.; Yang, P., Catalytic Growth of Zinc Oxide Nanowires by Vapor Transport. *ChemInform* 2001, 32, no-no.

127. Govender, K.; Boyle, D. S.; Kenway, P. B.; O'Brien, P., Understanding the factors that govern the deposition and morphology of thin films of ZnO from aqueous solution. *J Mater Chem* 2004, 14, 2575-2591.

128. Ku, C. H.; Wu, J. J., Chemical bath deposition of ZnO nanowire,nanoparticle composite electrodes for use in dye-sensitized solar cells. *Nanotechnology* 2007, 18, 505706.

129. Liu, B.; Zeng, H. C., Hydrothermal synthesis of ZnO nanorods in the diameter regime of 50 nm. *J Am Chem Soc* 2003, 125, 4430-4431.

130. De Yoreo, J. J.; Vekilov, P. G., Principles of crystal nucleation and growth. *Rev Mineral Geochem* 2003, 54, 57-93.

131. Lowenstam, H. A.; Weiner, S., *On biomineralization*. Oxford University Press, USA: 1989.

132. Yu, S. H.; C√∂lfen, H.; Hartmann, J.; Antonietti, M., Biomimetic Crystallization of Calcium Carbonate Spherules with Controlled Surface Structures and Sizes by Double,ÄêHydrophilic Block Copolymers. *Adv Funct Mater* 2002, 12, 541-545.

133. Aizenberg, J.; Black, A. J.; Whitesides, G. M., Oriented growth of calcite controlled by self-assembled monolayers of functionalized alkanethiols supported on gold and silver. *J Am Chem Soc* 1999, 121, 4500-4509.

134. Belcher, A. M.; Wu, X.; Christensen, R.; Hansma, P.; Stucky, G.; Morse, D., Control of crystal phase switching and orientation by soluble mollusc-shell proteins. 1996.

135. Gupta, A. K.; Gupta, M., Synthesis and surface engineering of iron oxide nanoparticles for biomedical applications. *Biomaterials* 2005, 26, 3995-4021.

136. Cha, J. N.; Stucky, G. D.; Morse, D. E.; Deming, T. J., Biomimetic synthesis of ordered silica structures mediated by block copolypeptides. *Nature* 2000, 403, 289-292.

137. Cao, G., *Nanostructures and Nanomaterials: Synthe*. Imperial College Pr: 2004.

138. Li, D.; Soberanis, F.; Fu, J.; Hou, W.; Wu, J.; Kisailus, D., Growth mechanism of highly branched titanium dioxide nanowires via oriented attachment. *Cryst Growth Des*.

139. Wang, B.; Shi, E.; Zhong, W., Twinning morphologies and mechanisms of ZnO crystallites under hydrothermal conditions. *Cryst Res Technol* 1998, 33, 937-941.

140. Zhang, Q.; Liu, S. J.; Yu, S. H., Recent advances in oriented attachment growth and synthesis of functional materials: concept, evidence, mechanism, and future. *J Mater Chem* 2009, 19, 191-207.

141. Sounart, T. L.; Liu, J.; Voigt, J. A.; Huo, M.; Spoerke, E. D.; McKenzie, B., Secondary nucleation and growth of ZnO. *J Am Chem Soc* 2007, 129, 15786-15793.

142. Kim, Y. Y.; Kong, B. H.; Cho, H. K., Vertically arrayed Ga-doped ZnO nanorods grown by magnetron sputtering: The effect of Ga contents and microstructural evaluation. *J Cryst Growth* 2011, 330, 17-21.

143. Zhao, F.; Zheng, J.-G.; Yang, X.; Li, X.; Wang, J.; Zhao, F.; Wong, K. S.; Liang, C.; Wu, M., Complex ZnO nanotree arrays with tunable top, stem and branch structures. *Nanoscale* 2010, 2, 1674-1683.

144. Zhao, F.; Li, X.; Zheng, J.-G.; Yang, X.; Zhao, F.; Wong, K. S.; Wang, J.; Lin, W.; Wu, M.; Su, Q., ZnO pine-nanotree arrays grown from facile metal chemical corrosion and oxidation. *Chem Mater* 2008, 20, 1197-1199.

145. Yu, Z.; Hahn, M. A.; Maccagnano-Zacher, S. E.; Calcines, J.; Krauss, T. D.; Alldredge, E. S.; Silcox, J., Small-angle rotation in individual colloidal CdSe quantum rods. *Acs Nano* 2008, 2, 1179-1188.

146. Gao, X.; Li, X.; Yu, W., Flowerlike ZnO nanostructures via hexamethylenetetramine-assisted thermolysis of zinc-ethylenediamine complex. *The Journal of Physical Chemistry B* 2005, 109, 1155-1161.

147. Liu, B.; Zeng, H. C., Room temperature solution synthesis of monodispersed single-crystalline ZnO nanorods and derived hierarchical nanostructures. *Langmuir* 2004, 20, 4196-4204.

148. Liu, Y.; Kang, Z.; Chen, Z.; Shafiq, I.; Zapien, J.; Bello, I.; Zhang, W.; Lee, S., Synthesis, characterization, and photocatalytic application of different ZnO nanostructures in array configurations. *Crystal Growth and Design* 2009, 9, 3222-3227.

149. Yamabi, S.; Imai, H., Growth conditions for wurtzite zinc oxide films in aqueous solutions. *J Mater Chem* 2002, 12, 3773-3778.

150. Lu, F.; Cai, W.; Zhang, Y., ZnO hierarchical micro/nanoarchitectures: solvothermal synthesis and structurally enhanced photocatalytic performance. *Adv Funct Mater* 2008, 18, 1047-1056.

151. Xiong, G.; Pal, U.; Serrano, J.; Ucer, K.; Williams, R., Photoluminesence and FTIR study of ZnO nanoparticles: the impurity and defect perspective. *physica status solidi (c)* 2006, 3, 3577-3581.

152. Tang, L. G.; Hon, D. N. S., Chelation of chitosan derivatives with zinc ions. III. Association complexes of Zn2+ onto O,N-carboxymethyl chitosan. *J Appl Polym Sci* 2001, 79, 1476-1485.

153. Ohta, T., Solar-hydrogen energy systems. *Solar-Hydrogen Energy Systems* 1979, 1.

154. Bolton, J. R., Solar photoproduction of hydrogen: A review. *Sol Energy* 1996, 57, 37-50.

155. Liao, C.-H.; Huang, C.-W.; Wu, J., Hydrogen Production from Semiconductor-based Photocatalysis via Water Splitting. *Catalysts* 2012, 2, 490-516.

156. Hong, S. J.; Lee, S.; Jang, J. S.; Lee, J. S., Heterojunction BiVO4/WO3 electrodes for enhanced photoactivity of water oxidation. *Energ Environ Sci* 2011, 4, 1781-1787.

157. Sivula, K.; Formal, F. L.; Grätzel, M., WO3− Fe2O3 Photoanodes for Water Splitting: A Host Scaffold, Guest Absorber Approach. *Chem Mater* 2009, 21, 2862-2867.

158. Somasundaram, S.; Chenthamarakshan, C. R. N.; de Tacconi, N. R.; Rajeshwar, K., Photocatalytic production of hydrogen from electrodeposited p-Cu2O film and sacrificial electron donors. *Int J Hydrogen Energ* 2007, 32, 4661-4669.

159. Wang, G. M.; Yang, X. Y.; Qian, F.; Zhang, J. Z.; Li, Y., Double-Sided CdS and CdSe Quantum Dot Co-Sensitized ZnO Nanowire Arrays for Photoelectrochemical Hydrogen Generation. *Nano Lett* 2010, 10, 1088-1092.

160. Feng, X. J.; Shankar, K.; Varghese, O. K.; Paulose, M.; Latempa, T. J.; Grimes, C. A., Vertically Aligned Single Crystal TiO2 Nanowire Arrays Grown Directly on

Transparent Conducting Oxide Coated Glass: Synthesis Details and Applications. *Nano Lett* 2008, 8, 3781-3786.

161. Yu, Y. X.; Xu, D. S., Single-crystalline TiO2 nanorods: Highly active and easily recycled photocatalysts. *Appl Catal B-Environ* 2007, 73, 166-171.

162. Bao, J. M.; Zimmler, M. A.; Capasso, F.; Wang, X. W.; Ren, Z. F., Broadband ZnO single-nanowire light-emitting diode. *Nano Lett* 2006, 6, 1719-1722.

163. Polleux, J.; Gurlo, A.; Barsan, N.; Weimar, U.; Antonietti, M.; Niederberger, M., Template-Free Synthesis and Assembly of Single-Crystalline Tungsten Oxide Nanowires and their Gas-Sensing Properties. *Angewandte Chemie* 2006, 118, 267-271.

164. Pradhan, S. K.; Reucroft, P. J.; Yang, F. Q.; Dozier, A., Growth of TiO2 nanorods by metalorganic chemical vapor deposition. *J Cryst Growth* 2003, 256, 83-88.

165. Wu, J. M.; Shih, H. C.; Wu, W. T., Formation and photoluminescence of single-crystalline rutile TiO2 nanowires synthesized by thermal evaporation. *Nanotechnology* 2006, 17, 105-109.

166. Zhu, G.; Pan, L. K.; Xu, T.; Sun, Z., One-Step Synthesis of CdS Sensitized TiO2 Photoanodes for Quantum Dot-Sensitized Solar Cells by Microwave Assisted Chemical Bath Deposition Method. *Acs Appl Mater Inter* 2011, 3, 1472-1478.

167. Miao, Z.; Xu, D. S.; Ouyang, J. H.; Guo, G. L.; Zhao, X. S.; Tang, Y. Q., Electrochemically induced sol-gel preparation of single-crystalline TiO2 nanowires. *Nano Lett* 2002, 2, 717-720.

168. Li, D. S.; Soberanis, F.; Fu, J.; Hou, W. T.; Wu, J. Z.; Kisailus, D., Growth Mechanism of Highly Branched Titanium Dioxide Nanowires via Oriented Attachment. *Cryst Growth Des* 2013, 13, 422-428.

169. Arab, S.; Li, D. S.; Kinsinger, N.; Zaera, F.; Kisailus, D., Solvothermal synthesis of a highly branched Ta-doped TiO2. *J Mater Res* 2011, 26, 2653-2659.

170. Nowotny, M. K.; Sheppard, L. R.; Bak, T.; Nowotny, J., Defect chemistry of titanium dioxide. application of defect engineering in processing of TiO2-based photocatalysts. *J Phys Chem C* 2008, 112, 5275-5300.

171. Chen, X.; Liu, L.; Peter, Y. Y.; Mao, S. S., Increasing solar absorption for photocatalysis with black hydrogenated titanium dioxide nanocrystals. *Science* 2011, 331, 746-750.

172. Zhu, J.; Vo, T.; Li, D.; Lu, R.; Kinsinger, N. M.; Xiong, L.; Yan, Y.; Kisailus, D., Crystal Growth of Li [Ni1/3Co1/3Mn1/3] O2 as a Cathode Material for High-Performance Lithium Ion Batteries. *Cryst Growth Des* 2012, 12, 1118-1123.

173. Hill, J. J.; Haller, K.; Gelfand, B.; Ziegler, K. J., Eliminating Capillary Coalescence of Nanowire Arrays with Applied Electric Fields. *Acs Appl Mater Inter* 2010, 2, 1992-1998.

174. Voorhees, P. W., The theory of Ostwald ripening. *Journal of Statistical Physics* 1985, 38, 231-252.

175. Penn, R. L.; Banfield, J. F., Morphology development and crystal growth in nanocrystalline aggregates under hydrothermal conditions: Insights from titania. *Geochimica et cosmochimica acta* 1999, 63, 1549-1557.

176. Oliver, P. M.; Watson, G. W.; Kelsey, E. T.; Parker, S. C., Atomistic simulation of the surface structure of the TiO2 polymorphs rutile and anatase. *J Mater Chem* 1997, 7, 563-568.

177. Mason, M. S.; Chen, C. M.; Atwater, H. A., Hot-wire chemical vapor deposition for epitaxial silicon growth on large-grained polycrystalline silicon templates. *Mater Res Soc Symp P* 2003, 762, 551-556.

178. Guo, T.; Chen, Y.; Liu, L.; Cheng, Y.; Zhang, X.; Ma, B.; Wei, M., Homoepitaxial growth and photoluminescence of self-assembled In-doped ZnS nanowire bundles. *Cryst Res Technol* 2012, 47, 449-454.

179. Grandusky, J. R., *Homoepitaxial growth of gallium nitride and aluminum nitride and its effects on device properties*. ProQuest: 2007.

180. Burton, W.; Cabrera, N., Crystal growth and surface structure. Part I. *Discussions of the Faraday Society* 1949, 5, 33-39.

181. Jeong, H.-C.; Williams, E. D., Steps on surfaces: experiment and theory. *Surf Sci Rep* 1999, 34, 171-294.

182. Naldoni, A.; Allieta, M.; Santangelo, S.; Marelli, M.; Fabbri, F.; Cappelli, S.; Bianchi, C. L.; Psaro, R.; Dal Santo, V., Effect of Nature and Location of Defects on Bandgap Narrowing in Black TiO2 Nanoparticles. *J Am Chem Soc* 2012, 134, 7600-7603.

183. Lee, J. H.; Hon, M. H.; Chung, Y. W.; Leu, I. C., Microcontact Printing of Organic Self-Assembled Monolayers for Patterned Growth of Well-Aligned ZnO Nanorod Arrays and their Field-Emission Properties. *J Am Ceram Soc* 2009, 92, 2192-2196.

184. Zubavichus, Y.; Slovokhotov, Y. L.; Nazeeruddin, M. K.; Zakeeruddin, S.; Grätzel, M.; Shklover, V., Structural characterization of solar cell prototypes based on nanocrystalline TiO2 anatase sensitized with Ru complexes. X-ray diffraction, XPS, and XAFS spectroscopy study. *Chem Mater* 2002, 14, 3556-3563.

185. Schulze, P. D.; Hardegree, E. L., X-ray photoelectron study of the reaction of oxygen, nitric oxide, nitrous oxide, and water-d2 with gadolinium. *The Journal of Physical Chemistry* 1989, 93, 5254-5256.

186. Tan, X.; Fan, Q.; Wang, X.; Grambow, B., Eu (III) sorption to TiO2 (anatase and rutile): batch, XPS, and EXAFS studies. *Environ Sci Technol* 2009, 43, 3115-3121.

187. Wang, R.; Sakai, N.; Fujishima, A.; Watanabe, T.; Hashimoto, K., Studies of surface wettability conversion on TiO2 single-crystal surfaces. *The Journal of Physical Chemistry B* 1999, 103, 2188-2194.

188. Wang, G.; Wang, H.; Ling, Y.; Tang, Y.; Yang, X.; Fitzmorris, R. C.; Wang, C.; Zhang, J. Z.; Li, Y., Hydrogen-treated TiO2 nanowire arrays for photoelectrochemical water splitting. *Nano Lett* 2011, 11, 3026-3033.

189. Shultz, A. N.; Jang, W.; Hetherington III, W. M.; Baer, D. R.; Wang, L.-Q.; Engelhard, M. H., Comparative second harmonic generation and X-ray photoelectron spectroscopy studies of the UV creation and O< sub> 2</sub> healing of Ti< sup> 3+</sup> defects on (110) rutile TiO< sub> 2</sub> surfaces. *Surf Sci* 1995, 339, 114-124.

190. Otálora, F.; García-Ruiz, J., Nucleation and growth of the Naica giant gypsum crystals. *Chem Soc Rev* 2014, 43, 2013-2026.

191. Adamson, A. W.; Gast, A. P., Physical chemistry of surfaces. 1967.

192. De Yoreo, J. J.; Vekilov, P. G., Principles of crystal nucleation and growth. *Reviews in mineralogy and geochemistry* 2003, 54, 57-93.

193. Hu, Y. H., A Highly Efficient Photocatalyst—Hydrogenated Black TiO2 for the Photocatalytic Splitting of Water. *Angewandte Chemie International Edition* 2012, 51, 12410-12412.

194. Cronemeyer, D., Infrared Absorption of Reduced Rutile Ti O 2 Single Crystals. *Physical Review* 1959, 113, 1222.

195. Pan, X.; Yang, M.-Q.; Fu, X.; Zhang, N.; Xu, Y.-J., Defective TiO 2 with oxygen vacancies: synthesis, properties and photocatalytic applications. *Nanoscale* 2013, 5, 3601-3614.

196. Colborn, T.; vom Saal, F. S.; Soto, A. M., Developmental effects of endocrine-disrupting chemicals in wildlife and humans. *Environmental health perspectives* 1993, 101, 378.

197. Benotti, M. J.; Trenholm, R. A.; Vanderford, B. J.; Holady, J. C.; Stanford, B. D.; Snyder, S. A., Pharmaceuticals and endocrine disrupting compounds in US drinking water. *Environ Sci Technol* 2008, 43, 597-603.

198. Catano, F. A.; Valencia, S. H.; Hincapie, E. A.; Restrepo, G. M.; Marin, J. M., A Comparative Study between Tio2 and Zno Photocatalysis: Photocatalytic Degradation of Cibacron Yellow Fn-2r Dye. *Lat Am Appl Res* 2012, 42, 33-38.

199. Daneshvar, N.; Salari, D.; Khataee, A. R., Photocatalytic degradation of azo dye acid red 14 in water on ZnO as an alternative catalyst to TiO2. *J Photoch Photobio A* 2004, 162, 317-322.

200. Fei, H. L.; Liu, Y. P.; Li, Y. P.; Sun, P. C.; Yuan, Z. Y.; Li, B. H.; Ding, D. T.; Chen, T. H., Selective synthesis of borated meso-macroporous and mesoporous spherical TiO2 with high photocatalytic activity. *Micropor Mesopor Mat* 2007, 102, 318-324.

201. Mu, J. B.; Shao, C. L.; Guo, Z. C.; Zhang, Z. Y.; Zhang, M. Y.; Zhang, P.; Chen, B.; Liu, Y. C., High Photocatalytic Activity of ZnO-Carbon Nanofiber Heteroarchitectures. *Acs Appl Mater Inter* 2011, 3, 590-596.

202. Sun, L. D.; Zhang, J.; Yin, J. L.; Su, H. L.; Liao, C. S.; Yan, C. H., Control of ZnO morphology via a simple solution route. *Chem Mater* 2002, 14, 4172-4177.

203. Wang, E. B.; Wang, C. L.; Shen, E. H.; Gao, L.; Kang, Z. K.; Tian, C. G.; Lan, Y.; Zhang, C., Controllable synthesis of ZnO nanocrystals via a surfactant-assisted alcohol thermal process at a low temperature. *Mater Lett* 2005, 59, 2867-2871.

204. He, Y.; Sang, W. B.; Wang, J.; Wu, R. F.; Min, J. H., Polymer-assisted complexing controlled orientation growth of ZnO nanorods. *J Nanopart Res* 2005, 7, 307-311.

205. Cristina Yeber, M.; Rodríguez, J.; Freer, J.; Durán, N.; D Mansilla, H., Photocatalytic degradation of cellulose bleaching effluent by supported TiO< sub> 2</sub> and ZnO. *Chemosphere* 2000, 41, 1193-1197.

206. Ye, C.; Bando, Y.; Shen, G.; Golberg, D., Thickness-dependent photocatalytic performance of ZnO nanoplatelets. *The Journal of Physical Chemistry B* 2006, 110, 15146-15151.

207. Zheng, Y.; Zheng, L.; Zhan, Y.; Lin, X.; Zheng, Q.; Wei, K., Ag/ZnO heterostructure nanocrystals: synthesis, characterization, and photocatalysis. *Inorg Chem* 2007, 46, 6980-6986.

208. Zhang, Y.; Xu, J.; Xu, P.; Zhu, Y.; Chen, X.; Yu, W., Decoration of ZnO nanowires with Pt nanoparticles and their improved gas sensing and photocatalytic performance. *Nanotechnology* 2010, 21, 285501.

209. Song, K. Y.; Park, M. K.; Kwon, Y. T.; Lee, H. W.; Chung, W. J.; Lee, W. I., Preparation of transparent particulate MoO3/TiO2 and WO3/TiO2 films and their photocatalytic properties. *Chem Mater* 2001, 13, 2349-2355.

210. Ostermann, R.; Li, D.; Yin, Y.; McCann, J. T.; Xia, Y., V2O5 nanorods on TiO2 nanofibers: A new class of hierarchical nanostructures enabled by electrospinning and calcination. *Nano Lett* 2006, 6, 1297-1302.

211. Zhang, Y.; Tang, Z.-R.; Fu, X.; Xu, Y.-J., Engineering the unique 2D mat of graphene to achieve graphene-TiO2 nanocomposite for photocatalytic selective transformation: what advantage does graphene have over its forebear carbon nanotube? *Acs Nano* 2011, 5, 7426-7435.

212. Williams, G.; Seger, B.; Kamat, P. V., TiO2-graphene nanocomposites. UV-assisted photocatalytic reduction of graphene oxide. *Acs Nano* 2008, 2, 1487-1491.

213. Fu, H.; Xu, T.; Zhu, S.; Zhu, Y., Photocorrosion inhibition and enhancement of photocatalytic activity for ZnO via hybridization with C60. *Environ Sci Technol* 2008, 42, 8064-8069.

214. Zhang, L. W.; Fu, H. B.; Zhu, Y. F., Efficient TiO2 Photocatalysts from Surface Hybridization of TiO2 Particles with Graphite-like Carbon. *Adv Funct Mater* 2008, 18, 2180-2189.

215. Sanchez, C.; Arribart, H.; Guille, M. M. G., Biomimetism and bioinspiration as tools for the design of innovative materials and systems. *Nature materials* 2005, 4, 277-288.

216. Mann, S., Biomimetic materials chemistry. *Biomimetic Materials Chemistry, by Stephen Mann (Editor), pp. 400. ISBN 0-471-18597-3. Wiley-VCH, November 1995.* 1995, 1.

217. Kinsinger, N.; Tantuccio, A.; Sun, M.; Yan, Y.; Kisailus, D., Photocatalytic Titanium Dioxide Composite. *J Nanosci Nanotechno* 2011, 11, 7015-7021.

218. Hosono, E.; Fujihara, S.; Kimura, T.; Imai, H., Growth of layered basic zinc acetate in methanolic solutions and its pyrolytic transformation into porous zinc oxide films. *J Colloid Interf Sci* 2004, 272, 391-398.

219. Choy, J.-H.; Kwon, Y.-M.; Han, K.-S.; Song, S.-W.; Chang, S. H., Intra-and inter-layer structures of layered hydroxy double salts, Ni1-xZn2x [OH) 2 (CH3CO2) 2x. nH2O. *Mater Lett* 1998, 34, 356-363.

220. Yang, J. M.; Su, W. Y.; Leu, T. L.; Yang, M. C., Evaluation of chitosan/PVA blended hydrogel membranes. *journal of Membrane Science* 2004, 236, 39-51.

221. Sang, W.; Fang, Y.; Fan, J.; He, Y.; Min, J.; Qian, Y., Novel synthesis method of ZnO nanorods by ion complex transformed PVA-assisted nucleation. *J Cryst Growth* 2007, 299, 272-276.

222. Peng, Z.; Kong, L. X., A thermal degradation mechanism of polyvinyl alcohol/silica nanocomposites. *Polym Degrad Stabil* 2007, 92, 1061-1071.

223. Wang, Y.; Li, Y.; Zhou, Z.; Zu, X.; Deng, Y., Evolution of the zinc compound nanostructures in zinc acetate single-source solution. *J Nanopart Res* 2011, 13, 5193-5202.

224. Lei, X.-f.; Ma, J.-x., Synthesis and electrochemical performance of aluminum based composites. *Journal of the Brazilian Chemical Society* 2010, 21, 209-213.

225. Ferrari, A. C., Raman spectroscopy of graphene and graphite: disorder, electron–phonon coupling, doping and nonadiabatic effects. *Solid State Commun* 2007, 143, 47-57.

226. Oku, T.; Hirano, T.; Suganuma, K.; Nakajima, S., Formation and structure of carbon nanocage structures produced by polymer pyrolysis and electron-beam irradiation. *J Mater Res* 1999, 14, 4266-4273.

227. Yang, X.; Shao, C.; Guan, H.; Li, X.; Gong, J., Preparation and characterization of ZnO nanofibers by using electrospun PVA/zinc acetate composite fiber as precursor. *Inorganic Chemistry Communications* 2004, 7, 176-178.

228. Roy, A. S.; Gupta, S.; Sindhu, S.; Parveen, A.; Ramamurthy, P. C., Dielectric properties of novel PVA/ZnO hybrid nanocomposite films. *Composites Part B: Engineering* 2013, 47, 314-319.

229. Lee, S.; Jeong, S.; Kim, D.; Hwang, S.; Jeon, M.; Moon, J., ZnO nanoparticles with controlled shapes and sizes prepared using a simple polyol synthesis. *Superlattice Microst* 2008, 43, 330-339.

230. Oku, T.; Hirano, T.; Kuno, M.; Kusunose, T.; Niihara, K.; Suganuma, K., Synthesis, atomic structures and properties of carbon and boron nitride fullerene materials. *Mat Sci Eng B-Solid* 2000, 74, 206-217.

231. Zhang, Y.; Zhu, F.; Zhang, J. X.; Xia, L. L., Converting layered zinc acetate nanobelts to one-dimensional structured ZnO nanoparticle aggregates and their photocatalytic activity. *Nanoscale Res Lett* 2008, 3, 201-204.

232. Wang, S.; Ang, P. K.; Wang, Z.; Tang, A. L. L.; Thong, J. T.; Loh, K. P., High mobility, printable, and solution-processed graphene electronics. *Nano Lett* 2009, 10, 92-98.

233. Fortunato, E. M.; Barquinha, P. M.; Pimentel, A. C.; Gonçalves, A. M.; Marques, A. J.; Martins, R. F.; Pereira, L. M., Wide-bandgap high-mobility ZnO thin-film transistors produced at room temperature. *Appl Phys Lett* 2004, 85, 2541-2543.